

LANCASTER UNIVERSITY

DOCTORAL THESIS

**Quasiparticle Beam Profile Measurements in
Superfluid Helium 3 - B**

Author:

Sean.L.Ahlstrom

Supervisor:

Viktor Tsepelin

*A thesis submitted in fulfilment of the requirements
for the degree of Doctor of Philosophy*

in the

Ultra Low Temperature Research Group
Lancaster University

November 2016

Declaration of Authorship

This research was performed as a collaborative effort between various members of the Lancaster Ultra Low Temperature research group. I hereby declare that the work contained in this thesis is the authors own work and has not been submitted for the award of a higher degree at any other university.

“Alea Iacta est! (The die is cast)”

Julius Caesar (As he led his army over the Rubicon)

Abstract

This thesis details experiments in the ballistic regime of superfluid $^3\text{He-B}$ at temperatures around $100\ \mu\text{K}$. In this thesis, the quasiparticle beam profile from a Black-Body radiator and a vibrating wire resonator is measured using a quasiparticle camera which consists of 25 tuning forks. The vibrating wire resonator is found to have a very thinly spread beam at velocities slightly higher than the pair-breaking critical velocity which spreads out at higher velocities. At $21\ \text{mm/s}$ the vibrating resonator is found to have a more focused beam than the Black-Body radiator where both beam profiles are found to be focused around the centre of the quasiparticle camera. A theoretical model is created in order to model the spread and intensity of the experimental beam profile from the Black-Body radiator.

In this thesis, the response of some of the probes to thermal damping is measured in the form of the geometrical constants γ and λ . The geometrical constant λ is related to the velocity dependence of the probe to thermal damping and is found for two wires of varying diameter, a tuning fork and its overtone mode in which all the values of λ were close to unity. The geometrical constant γ is related to the sensitivity of a probe to thermal damping. This is found for a Black-Body radiator and then used to derive the sensitivity for other wires in the cell in thermal equilibrium with it. Two resonant modes of a small tuning fork are used to do a Black-Body radiator calibration on the area around the tuning fork which is used to find the sensitivity of 25 tuning forks (pixels) in the quasiparticle camera.

Acknowledgements

This thesis marks a substantial part of my life. A part that I would never be able to get through if it weren't for the help of all of the members of the Lancaster Ultra Low Temperature Research Group. A lot of the measurements taken in this thesis were a combined effort between us.

First of all, I would like to thank my supervisor Viktor Tsepelin for being there to guide me during my thesis write up, my measurements and for teaching me a lot I know today about the subject. I would like to thank Richard Haley, George Pickett, Tony Guènault, Ian Bradley for the countless discussions I've had with them during the course of these four years. Thank you to Chris Lawson, Roch Schanen, Matt Sarsby, Dmitry Zmeev, Maros Skyba, Jakub Vonka, Marcel Schrodin, Mark Giltrow, and Marcel Clovecko for answers to various technical questions and always being there if I needed a helping hand.

Thank you to Andrew Woods and Malcolm Poole for being there with me taking measurements over these past few years. Thank you for your insight and knowledge, a lot of the times there was no one else in the lab but us three and being there going through the measurements with you two was motivation and inspiration. Thank you to Edward Guise for making the cell with Andrew Woods. If it wasn't for you two there wouldn't be any experiment for me to retrieve any data from.

Thank you to Alan Stokes and Martin Ward for being a source of joy for me in these hard times. Thank you to Steve Holt for various electrical help as well as Steve Holden for helping me procure the right equipment. Thank you to Shonah Ion for being there during power outages and making sure we had the power to run our experiment. Thank you to Neil Drummond and Ian Bailey for looking through my thesis and suggesting some corrections. Thank you to anyone I missed.

Thank you to Luke Southwell and Nathan Woolett for keeping me on track. Knowing that I am not alone in my writing means a lot to me. Thanks also go to Luke Dunn, Charlotte Berry, Si Ye Huang, James Brandon, Melissa Leigh Wilkinson, and Jim Huxter for supporting me during this arduous time.

Finally, thank you to my brother Mark, and my mother Vandra for all the continued support. Thank you to my aunt Diana for getting me interested in physics all those years ago.

Contents

Declaration of Authorship	i
Abstract	iii
Acknowledgements	iv
Contents	v
List of Figures	viii
List of Tables	xiii
1 Introduction	1
1.1 History of Helium	1
1.2 Description of Thesis	4
2 Theoretical Background	6
2.1 Properties of ^3He	6
2.1.1 Quasiparticle Generation	7
2.2 Phases of ^3He	9
2.2.1 The Ballistic Regime	10
2.3 Properties of $^3\text{He-B}$	11
2.4 Vibrating Wire Theory	11
2.5 1D Simplification of the Damping Force on a Paddle in an Ideal Gas	14
2.6 Force on a Paddle With Respect to Andreev Reflection	16
2.6.1 Calculating the Temperature Using the Thermal Force	18
2.7 The Fraction of Quasiparticles That are Transmitted Through the Potential Barrier Caused by a Moving Superfluid	20
2.8 Calculating the Quasiparticle Flux $\langle nv_g \rangle$	22
2.9 Finding the Geometrical Constant λ	23
2.10 Pair Breaking Critical Velocity	23
2.11 Black Body Radiator Description	25
2.11.1 Damping Predictions	27
2.12 Finding the Geometrical Constant γ	29
2.12.1 Finding γ for a BBR	30

2.12.2	Using γ From One Tuning Fork in Order to Determine γ for Another Fork in Thermal Equilibrium with the First	30
2.12.3	Finding γ for One Wire Using γ From Another Wire in Thermal Equilibrium With It	31
2.13	Chapter Summary	32
3	Experimental Setup	34
3.1	Outline of the Cell	34
3.1.1	BBR Description	36
3.1.2	The Quasiparticle Camera	37
3.1.3	Properties of the MEMS	39
3.2	Operating Principle of Vibrating Resonators	39
3.2.1	Vibrating Wires	40
3.2.2	Tuning Forks	41
3.2.2.1	Properties That can be Calculated From the Tuning Fork Response	41
3.2.2.2	Tuning Fork Harmonics	43
3.2.2.3	Tuning Fork Setup	45
3.3	Measurement Techniques	46
3.3.1	Tracking Width	46
3.3.2	Frequency Sweeps	47
3.3.3	Amplitude Sweeps	48
3.4	Chapter Summary	49
4	Characterising the probes in the cell	50
4.1	Thermal Damping of Various Oscillators	51
4.1.1	Force-Velocity Characteristics of the Probes	51
4.1.2	The Force Velocity Gradient	54
4.1.3	Finding λ From the Amplitude Sweeps	56
4.2	Sensitivity of Vibrating Objects to Quasiparticles	60
4.2.1	Finding γ for $\mu\mu\mu_2$	60
4.2.2	Using γ for $\mu\mu\mu_2$ to Find γ for Other Wires in the Cell	60
4.2.3	Finding γ for D2 Using its Overtone Mode	61
4.2.4	Using the Value of γ From the Pixel Calibration to Find γ for the Rest of the Forks	66
4.3	Chapter Summary	67
5	Beam Profile From the BBR and Source Wire	69
5.1	Calibration of the BBR	70
5.2	BBR Beam Profile Measurements	72
5.2.1	Calculating the Width Parameter of the Forks due to the BBR	72
5.2.2	The Fork Damping During a BBR Ramp	73
5.2.3	Theoretical Estimations of the Width Parameter	75
5.3	Source Wire Beam Profile Measurements	79
5.3.1	Calculating the Width Parameter of the Forks for the Source Wire Ramp	79
5.3.2	Finding the Beam Profile for the Source Wire	80

5.4	Comparing the Power Captured by the Quasiparticle Camera From the BBR to the Source Wire	82
5.5	Chapter Summary	85
6	Summary	86
A	Preliminary Measurements	88
A.1	Background Corrections	88
A.2	Intrinsics	90
A.3	Non-Linear Corrections	91
A.4	Effective Width	94
	Bibliography	98

List of Figures

1.1	Phase Diagram of ^4He [23].	3
2.1	An energy level diagram of fermions at a temperature close to absolute zero. Fermions are shown filling the energy levels up to an energy close to the Fermi energy with some fermions in excited states.	6
2.2	The creation of a particle-hole excitation in a Fermi gas taken from [29].	7
2.3	The energy difference between the quasiparticle energy and the minimum Fermi energy ε for a quasiparticle against its momentum taken from [29]. Δ is the energy difference between the excitation energy and the energy of the condensate.	8
2.4	A figure of the discovery of superfluid ^3He , note that (A,B B' and A' all show phase transitions in the liquid) [27].	9
2.5	Phase diagram of ^3He [23].	10
2.6	A resonance of one of the probes in the cell when it was in superfluid helium 3. f_0 is the resonant frequency where Δf_2 is the full width at half maximum where the red line shows the real component of velocity and the blue line is the imaginary component of velocity.	13
2.7	A two dimensional model paddle moving through a gas.	15
2.8	Andreev reflection between a normal state A) and a superconducting state B). Particles are filled in black while Holes are filled in white. Dotted lines indicate the spin of the particle where filled lines indicate the momentum.	16
2.9	Andreev reflection in the superfluid with the fluid at rest in the front of the paddle in part 1) and the back of the paddle in part 3) where the fluid part 2) is moving with a velocity v towards the front 1). Δ is the energy gap needed to create excitations when the fluid is stationary.	17
2.10	The dispersion curve of the bulk ^3He next to a wire moving at velocity v	24
2.11	Thermalization of quasiparticles in the BBR where A) is the BBR without the heater wire on, B) is the BBR with the heater wire driven by a low driving force, and C) is the BBR with the heater wire driven by a high driving force.	25
2.12	A diagram showing the angle between the quasiparticle beam and the tuning fork. Note: this is a 2D sketch of a 3D situation.	27
3.1	A diagram of the different components in the inner cell. All the $M\mu$ wires have a diameter of $1.5\ \mu\text{m}$, all $\mu\mu\mu$ wires have a diameter of $4.5\ \mu\text{m}$ and all μ wires have a diameter of $1.5\ \mu\text{m}$. All the wires shown in the diagram apart from ICTA and the MEMS are made from Niobium Titanate.	35
3.2	A 2D diagram of the box and its dimensions (Not to Scale). The height of the box is $5.5\ \text{mm}$ and is not shown in the diagram.	36

3.3	A picture of the quasiparticle camera before it was added to the cell. . . .	37
3.4	A typical array of tuning forks that would be placed in the quasiparticle camera.	38
3.5	The setup for one of the arrays in the quasiparticle camera where five signals go through an array of 5 forks reaching a set of 5 Lockin Amplifiers. Note that SA is the summing amplifier with active attenuation and the IV is a current to voltage converter created by Holt et al. [48].	38
3.6	Setup of a vibrating wire. The signal is created by a generator and then goes through a drive box to the wire which generates a faraday voltage. This signal is amplified by a low temperature transformer and then read by an SR830.	41
3.7	The frequency ratio between the fundamental and first overtone modes as measured for a number of forks of similar width but varying lengths [47].	45
3.8	The setup of a single tuning fork	45
3.9	Using the DAQ program to track the width of two thermometers in the cell.	47
3.10	A frequency sweep of the fork D2 shortly after the cell had been demagnetized	48
3.11	The Force-Velocity characteristics of A2 found using an amplitude sweep. This is at a temperature of 108 μK	48
4.1	Amplitude sweeps of $\mu\mu\mu_3$ at different temperatures to find the force-velocity characteristics of the probe where black circles correspond to the intrinsic damping of the probe. The temperature of each characteristic is shown next to it on the graph. The circles indicate the part of the ramp where $\mu\mu\mu_3$ was increased to a certain drive while the lines indicate when the probe was ramped back down to a minimal drive.	52
4.2	I-swps taken of $\mu\mu\mu_3$, $M\mu$, D2 and D2OV1 at different temperatures in order to find the force-velocity characteristics of the probes. The temperatures are indicated at the start of the I-swp.	53
4.3	Intrinsic I-swps taken of various probes in the cell, These show a lack of Andreev reflection as there aren't any excitations in the bulk that the wire could shield itself from.	53
4.4	The change of $\frac{dF}{dV}$ against thermal force in an amplitude sweep taken on $\mu\mu\mu_3$ at 142 μK	54
4.5	The change of corrected $DFDV$ against thermal force in 1 I-swp of $\mu\mu\mu_3$ at 142 μK	56
4.6	The plot of reduced force against reduced velocity for the amplitude sweep of $\mu\mu\mu_3$ at 142 μK in order to find λ . The theoretical curve is with λ at 0.6 ± 0.03 . The error in lambda was found by comparing various theoretical curves and seeing which range of curves fit the data well. . . .	57
4.7	The plot of reduced force against reduced velocity for all the amplitude sweeps of $\mu\mu\mu_3$ analysed in order to find λ with a theoretical fit of λ is 0.50 ± 0.10	58
4.8	The plot of reduced force against reduced velocity for all the amplitude sweeps analysed in order to find λ with a theoretical fit of λ of 0.1 ± 0.03 .	59
4.9	Calculations of λ for various probes in the cell.	59

4.10	The hole drilled within the copper block has a depth of 4 mm (E) and a radius of 0.45 mm (D) in which the tuning fork is placed. The tuning fork used for these measurements is called D2, and this fork has a prong length shown by (A) of 1.75 mm as well as a prong thickness of 0.09 mm (B). The fork also has a distance between prongs of 0.09 mm which gives a total thickness of 0.27 mm (C). These forks also have a width of 0.05 mm which is not shown in the diagram.	62
4.11	Effect of the drive of the overtone of D2 on the damping of its fundamental during the measurement.	63
4.12	Effect of the power of D2OV1 on the damping of D2. This is a similar measurement to the BBR calibration.	64
4.13	Polynomial fit of the previous data.	64
4.14	Effect of the power of D2OV1 on D2 at high drives. This is done as it seems like there was a change in gradient in figure 4.13.	65
4.15	Effect of the power of D2OV1 on D2 at low drives. This is done as it seems like there was a change in gradient in figure 4.13.	65
5.1	The velocity against the force of the heater wire μ_2	71
5.2	The width of the thermometer wire $\mu\mu\mu_2$ against the drive (A) and velocity (B) of the heater wire μ_2	71
5.3	The calibration of the BBR where μ_2 is the heater wire and $\mu\mu\mu_2$ is the thermometer wire. The straight line is a least squared fit. For details see text.	72
5.4	The change in the width parameter for A3 (Red circles), B3 (Green squares), C3 (Blue diamonds), D3 (Magenta downwards triangles), and E3 (Cyan upwards triangles) against power during a BBR ramp. Note that by fitting a straight line we show that the beam profile does not change with respect to power.	73
5.5	The beam profile from the BBR as shown on each individual array. In this figure A Array (Red circles), B Array (Green squares), C Array (Blue diamonds), D Array (Magenta downwards triangles), and E Array (Cyan upwards triangles) are shown. This graph shows that the central array (C Array) receives the most damping with the damping falling off for pixels further from the focus of the beam, which seems to be slightly left of the centre of the array.	74
5.6	The beam profile from the BBR as shown on each individual array. In this figure $x=-2.2$ mm is shown as red circles, $x=-1.1$ mm is shown as green squares, $x=0$ mm is shown as blue diamonds, $x=1.1$ mm is shown as magenta downwards triangles, and $x=2.2$ mm is shown as cyan upwards triangles. This graph shows that the focus of the damping is between the second and third pixels and that the beam is shifted slightly towards D array.	74
5.7	The beam profile from the BBR at approximately 700 picowatts. The color bar at the side shows what width parameters each color represents.	75
5.8	The experimental data with theoretical fits for each of the arrays. Note due to symmetry only the fits for A (Red), B (Green) and C (Blue) are shown. This means the fit for D is the same as the fit for B, and the fit for E is the same as the fit for A. These fits are largely inconsistent with the data, which means some of the parameters of the fit must be off.	76

5.9	The experimental data with theoretical fits for each x position on the camera. Note due to symmetry only the fits for x=-2.2 mm (Red), x=-1.1 mm (Green) and x=0 mm (Blue) are shown. The fit for x=1.1 mm is exactly the same as the fit for x=-1.1 mm and the fit for x=2.2 mm is the same as the one for x=-2.2 mm. These fits are largely inconsistent with the data, which means some of the parameters of the fit must be off.	76
5.10	A colour map of the theoretical beam profile that was used to fit figure 5.8 and figure 5.9.	77
5.11	The experimental data with theoretical fits for each of the array where A is the red line, B is green, C is blue, D is magenta, and E is cyan. In this figure there is extra damping calculated for the central pixels that is not shown on the experimental data. This could be because some of the quasiparticles from the BBR go straight through the pixel instead of interacting with the fork.	77
5.12	The experimental data with theoretical fits for each x position on the camera. Note due to symmetry only the fits for x=-2.2 mm (Red), x=-1.1 mm (Blue) and x=2.2 mm (Cyan) are shown. The fit for x=-1.1 mm is exactly the same as the fit for x=0 mm and the fit for x=-2.2 mm is the same as the one for x=1.1 mm. In this figure there is extra damping calculated for the central pixels that is not shown on the experimental data. This could be because some of the quasiparticles from the BBR go straight through the pixel instead of interacting with the fork.	78
5.13	A colour map of the theoretical beam profile that was used to fit figure 5.11 and figure 5.12.	78
5.14	The force-velocity plot for the source wire. This graph shows that pair breaking happens at a velocity of the order of 10^{-2} m/s.	79
5.15	The width parameter against power for various forks during a $\mu\mu\mu_3$ ramp with A3 (red circles), B3 (green squares), C3 (blue diamonds), D3 (magenta downwards triangles), and E3 (cyan upwards triangles) shown where the velocity of the source wire is higher than the pair breaking critical velocity.	80
5.16	The full beam profile for the source wire where the power of the wire is approximately 48 pW. Shown in this figure are A array (Red circles), B array (Green Squares), C array (Blue Diamonds), D array (Magenta downwards triangles) and E array (Cyan upwards triangles). The beam from the source wire seems to be focused on C Array which indicates the beam is focused towards the centre of the camera.	81
5.17	The full beam profile for the source wire where the power of the wire is approximately 48 pW. Shown in the figure are x=-2.2 mm (Red circles), x=-1.1 mm (Green squares), x=0 mm (Blue diamonds), x=1.1 mm (Magenta downwards triangles) and x=2.2 mm (Cyan upwards triangles). This graph shows that the beam is centred close to the second pixel.	81
5.18	The full beam profile for the source wire shown in a colour map where the power of the wire is approximately 48 pW.	82
5.19	A comparison of the percentage of power trapped by $\mu\mu\mu_3$ and the BBR with a theoretical prediction shown as a red line for various powers. At low powers it shows that a high percentage of the power from the source wire is focused on the central pixels, with the beam spreading out at high powers.	83

5.20	A comparison of the percentage of power trapped by the source wire at 48 pW and the BBR at 678 pW with the corrected theoretical prediction for the diagonal down the camera shown by a red line.	83
5.21	A comparison of the percentage of power trapped by the source wire at different powers for a diagonal along the camera. Note that A1 at low powers shows a negative power percentage. This may have been because of small oscillations in the cell temperature with a period of approximately 200 s.	84
A.1	A typical fork background.	89
A.2	A DAQ background done at zero field.	89
A.3	An intrinsic amplitude sweep of the fork A2 at a temperature of 108 μ K.	91
A.4	Change in the width of a probe due to non-linearity. The probe V_x was ramped from 0.1 mV to 3 mV.	93
A.5	Signal height the probe was driven to during the non-linear measurement.	93
A.6	The width of the probe after it was non-linearly corrected using equation A.8.	94
A.7	Plot of the fork width against the width of the $M\mu$	95
A.8	Plot of the fork effective width against the $M\mu$ width.	96
A.9	Plot of the effective width of a fork in B array against the width of the $M\mu$	96

List of Tables

3.1	The relation between β values for various harmonics [61].	45
4.1	Effective width of the wires compared to $\mu\mu\mu_2$ and the value of γ for all wires except μ_2 , ICTA and OCTA.	61
4.2	Values of γ for all of the forks in camera. This was calculated using the effective width between the fork and D2.	67

Dedicated in the memory of Professor Shaun Neil Fisher. He was a great physicist and a good man. He was the one who chose me to do this doctorate and was there for me every step of the way.

Chapter 1

Introduction

1.1 History of Helium

Helium is an inert, unreactive gas at room temperature and pressure. It is light and because of this there is only a minute amount of it in the atmosphere of this planet (5 ppm) [1]. However while there is only a small amount of helium on the Earth there is a large abundance of it in the solar system. Most of this abundance is found in the sun [2]. Because of this evidence of this atom only started to emerge in 1868 when a man named Pierre Janssen found a new wavelength of light being emitted by the sun during a solar eclipse [3]. This was attributed to sodium however was proven later by Edward Frankland and Joseph Lockyer that this was not the case, and that a new element created these spectral lines. They named this element helium due to its connections with the sun [4] [5].

Helium was finally isolated by Sir William Ramsey in 1895 [6]. This was found when Sir Ramsey was trying to find the spectrum of a noble gas in a mineral containing Uranium. For the extraction of this element and the discovery of various noble gases Ramsey received the Nobel prize in chemistry [7]. After this discovery the mass of the helium atom was found to be that of helium 4. It would take a while until the only other stable isotope of helium called helium 3 was found. This is because helium 4 accounts for roughly 99.999% of all Helium [6].

Helium 3 makes up the rest of the total amount of stable helium on this planet. This isotope of helium was first discovered by Oliphant et al. in 1933 [8]. In Oliphant's measurement ${}^3\text{He}$ was discovered by bombarding Lithium atoms with protons [6]



The tritium in this experiment eventually decays into helium 3 via this process



Apart from the reactions shown earlier helium can be found either trapped underground in small quantities with natural gas [9] or it can be produced from nuclear fusion. This means of producing Helium includes reacting two isotopes of hydrogen (deuterium and tritium) together. The process is shown in equation 1.3 [10]



Due to helium being inert and light it has a large range of uses. Helium is commonly used for party and weather balloons. This atom is also used to cool superconductors due to its low boiling point. Devices that are cooled using liquid helium range from Magnetic Resonance Imaging scanners to CERN'S Large Hadron Collider [11]. For these uses helium 4 is used due to its high abundance relative to helium 3, however helium 3 has a large range of uses due to its unique properties [12]. This isotope of helium is mainly used to create a neutron detectors in order to detect radioactive isotopes at airports, which is due to the atom's high neutron capture cross section [13]. As helium has so many uses both isotopes are being used up at an incredibly fast rate. A large quantity of both isotopes of helium are owned by the US [14] and is stockpiled in Amarillo Texas, but has recently been sold off by the US government meaning there is a shortage of helium 3 [15].

The properties of helium that we are interested in are the properties that are revealed when the element is cooled to low temperatures. Helium 4 was first liquified by Kamerlingh Onnes in 1908 [16] [17] at a temperature of around 4K using a method similar to

the Linde process [18] [19]. For his work on finding superconductivity and his work on liquid Helium he received a Nobel prize in 1913 [20]. A new phase of liquid helium 4 called helium II (superfluid helium) was discovered by Kapitza in 1937 at temperatures around 2 K. This disproved that helium II was a crystalline solid phase thus proving that the change in specific heat previously seen by Kamerlingh Onnes was due to the liquid becoming a new state of matter [21]. The work on discovering superfluid Helium was one of the reasons that Kapitza received the Nobel prize [22]. These measurements give the phase diagram of shown in figure 1.1.

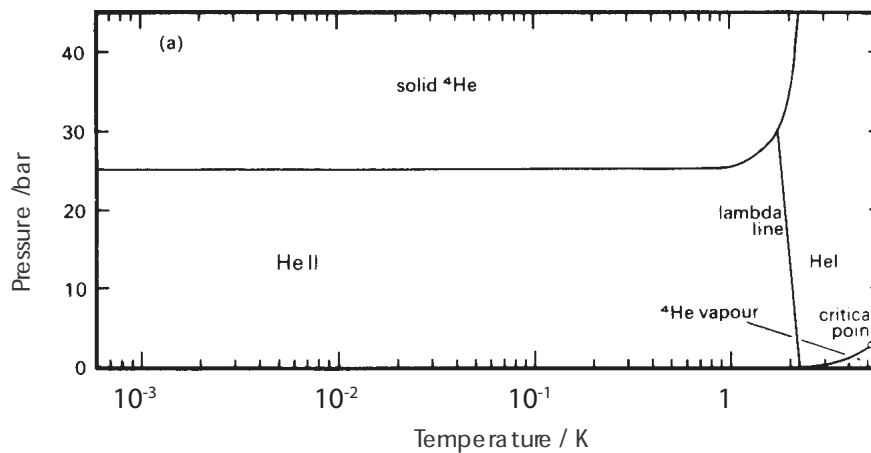


FIGURE 1.1: Phase Diagram of ${}^4\text{He}$ [23].

Helium 3 was first liquefied by Sydoriak, Grilly, and Hammel in 1949 [24] at a temperature of 3.33 K and a pressure of ~ 1 bar. A new state of ${}^3\text{He}$ was found by Lee, Osheroff, and Richardson in 1972. The liquid in this experiment was being cooled on the solid liquid line of figure 2.5 at a pressure of ~ 35 bar.

During this experiment pressure changes were seen in the sample. This was originally thought to be due to some change in the solid [25] although this was discounted and the change in pressure was eventually found to be due to a change to the liquid. The change in pressure in the liquid was found to be due to the liquid ${}^3\text{He}$ turning into a new state of matter. The discovery of this new state gave the trio the Nobel prize in physics [26]. The reference shown in [27] gives the review article of the measurements taken that gave them the Nobel prize. A diagram of the phases of ${}^3\text{He}$ is shown in section 2.2.

1.2 Description of Thesis

This thesis studies the quasiparticle beam profile of a wire and a Black-Body Radiator in $^3\text{He-B}$. In Chapter 2 the theoretical background behind these measurement starting with the properties and phases of ^3He and then moving onto the properties of $^3\text{He-B}$ are explained first. This chapter then moves onto Andreev reflection which is later used to find derivations for 2 geometrical constants, the sensitivity of a probe to thermal damping γ and λ which is related to the velocity dependence of the probe to thermal damping. After that a theoretical model for the beam profile will be derived in order to be compared to experimental data in further chapters and the resonant properties of vibrating wires will be discussed.

Chapter 3 explains the setup of all the instruments in this experiment. It starts off with explaining the setup of the cell and then goes on to explain the setup of the tuning forks and the wires as well as the properties of the first overtones of tuning forks compared to the their fundamental frequencies. This section then goes on to explain the specifics of how 5 arrays of 5 tuning forks make up the 25 pixel detector that was built in order to view this beam profile. It then goes on to talk about the black body radiator (BBR) and how it is used to create a quasiparticle beam. The experimental section also deals with the setup outside the cell. This includes the Stanford Research 830 and 844 lockins (SR830, SR844) as well as the Agilent generators, the summing amplifiers, and the current to voltage converters ((I-V) converters) used in the setup. We discuss how the readings from the SR830/844s are sent to the computer for analysis and explain in brief the differences between these Lockins. Finally the Labview programs used for these measurements will be explained as well as their respective pros and cons of each Labview program used. The three programs are frequency sweep (f-swp), amplitude sweep (I-swp) and the Data Acquisition (DAQ) program.

Chapter 4 gives the calculations of the geometrical constant γ for the Black Body Radiator (BBR) in the cell and a tuning fork. The Black Body Radiator was calibrated using measurements where the power of the BBR was increased while the damping on a detector wire inside the BBR was measured. The value of γ is first found for a wire in a black body radiator and then found for a tuning fork in the 25 pixel detector. In this same chapter the geometrical constant λ is calculated for various wires and forks. This is done using amplitude sweeps (I-swp) on the probe and by comparing the probe I-swp

at its lowest temperatures (Intrinsic sweep) to those at higher temperatures in order to find the thermal damping. From the velocity of the probe a value called the reduced velocity can be calculated. From the gradient of thermal force over reduced velocity the reduced force can be found. The value of λ can then be found by plotting the reduced force against reduced velocity and fitting the curve it creates. The value of λ is useful as it can be used to get rid of the non-linear damping of any probe it is calculated for. The value of λ represents how much the probe responds to the quasiparticle flux local to it. This value is dependent upon the geometry of the probe and it is seen that for a different probe geometry there is a different value of λ .

In Chapter 5 the power of the BBR was increased and the effects of this on the damping of the tuning forks in the 25 pixel detector were measured. The damping on the tuning forks is also measured when a wire close to the detector is driven to different velocities ($\mu\mu\mu_3$). The profile of the beam from the BBR and a wire ($\mu\mu\mu_3$) close to the 25 pixel detector will be discussed. These results will be shown for when the BBR is at different powers and when the wire is driven to different velocities. For the BBR the experimental data is compared against theoretical predictions. These theoretical predictions use the value of γ for a BBR calculated previously in Section 4.2.1.

The appendices deal with some of the preliminary measurements taken in order to find some of the key properties of the probe needed for further analysis. These include background measurements, intrinsic measurements, and non-linear corrections. The damping on the tuning forks is also turned into an effective damping for an easier comparison between the forks for further measurements. The background measurements were taken at a frequency that is far away from the resonance for the tuning forks. This was at ± 100 Hz for most of the resonances. The backgrounds were taken on resonance but at zero magnetic field strength for the wires. The intrinsics were estimated alongside λ using the non-linear correction data.

Chapter 2

Theoretical Background

2.1 Properties of ^3He

^3He is a fermion as it has a single unpaired neutron which gives it a total non-integer value of spin. All fermions must follow Fermi-Dirac statistics and the Pauli exclusion principle meaning that no two fermions can share exactly the same quantum numbers. As energy is directly linked to a quantum number only 2 fermions can share a quantum state one with spin up and one with spin down. At absolute zero fermions will fill all available energy levels up to the Fermi energy E_F . At non-zero temperature some of the fermions will become excited and will have energy higher than Fermi energy.

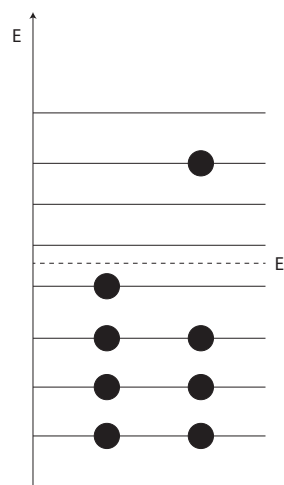


FIGURE 2.1: An energy level diagram of fermions at a temperature close to absolute zero. Fermions are shown filling the energy levels up to an energy close to the Fermi energy with some fermions in excited states.

When ^3He is cooled around 2 mK at pressures close to the solidification pressure some of the ^3He atoms create Cooper pairs in line with the theory created by Bardeen Cooper and Schrieffer (BCS theory) [28].

2.1.1 Quasiparticle Generation

The energy levels in a Fermi gas are filled up to the Fermi-energy at temperatures close to absolute zero. At energies close to the Fermi energy there will be particles that get excited with a small energy to an energy level that is above the Fermi surface which creates a quasihole-quasiparticle pair. This is shown in figure 2.2.

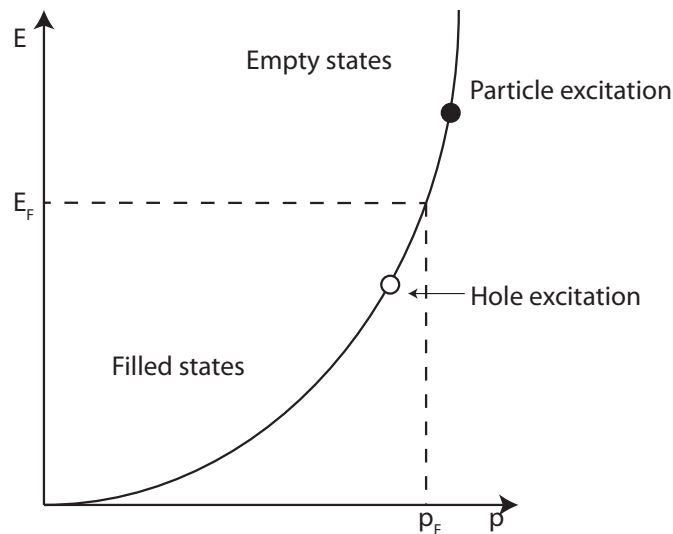


FIGURE 2.2: The creation of a particle-hole excitation in a Fermi gas taken from [29].

In a Fermi system with a condensate, a minimum energy of Δ is needed in order to move a particle from the condensate to an excited state. This means that any excitation in that Fermi system will have a minimum energy of Δ . Figure 2.3 shows the difference between the energy of the excitation and the Fermi energy against the momentum of the excitation.

The dotted line shown in figure 2.3 shows the Landau critical velocity. This is the minimum velocity that a probe can be driven to in order to create an excitation. In the model of the Landau critical velocity a projectile with mass m creates an excitation with energy E which causes the velocity of the projectile to change from v to v' . The value of this critical velocity can then be taken from the conservation of momentum and the conservation of energy shown by equations 2.2 and 2.1

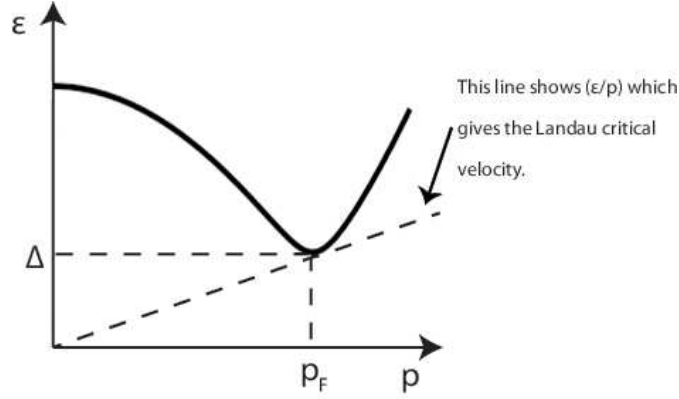


FIGURE 2.3: The energy difference between the quasiparticle energy and the minimum Fermi energy ε for a quasiparticle against its momentum taken from [29]. Δ is the energy difference between the excitation energy and the energy of the condensate.

$$mv' = mv - p, \quad (2.1)$$

$$\frac{mv'^2}{2} = \frac{mv^2}{2} - E. \quad (2.2)$$

In these equations p is the momentum of the excitation, v is the initial velocity of the probe and v' is the final velocity of the probe. These equations combine to form

$$\frac{mv^2}{2} = \frac{mv^2}{2} + \frac{p^2}{2m} - \mathbf{p} \cdot \mathbf{v} + E. \quad (2.3)$$

If the momentum of the excitation is assumed to be small then that gives us $-pv + E = 0$ which can be rearranged to give

$$v_L = \frac{\Delta}{p_F}, \quad (2.4)$$

where v_L is known as the Landau critical velocity which is shown on figure 2.3. At velocities close to this value quasiparticles will only have a minimal momentum change from the Fermi momentum. Higher velocities than the Landau critical velocity are needed to create higher energy excitations in the Fermi gas. The Landau critical velocity cannot be 0 as the minimum energy needed to create the excitation is Δ as shown in figure 2.3.

2.2 Phases of ^3He

While ^3He does create a condensate at very low temperatures it has various unique properties that need to be addressed further. The discovery of superfluidity by Lee, Oscheroff, and Richardson [27] found 2 phases of superfluid helium and the figure showing the features of this discovery is shown below in figure 2.4.

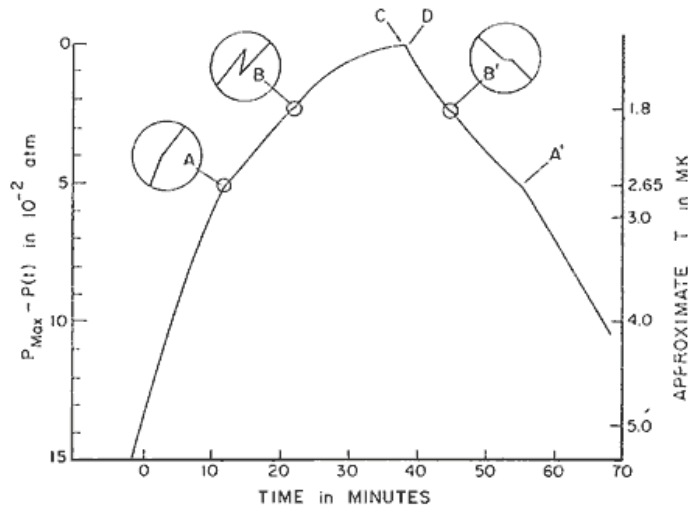


FIGURE 2.4: A figure of the discovery of superfluid ^3He , note that (A,B B' and A' all show phase transitions in the liquid) [27].

In this figure, ^3He was being cooled down at a pressure of around 35 bar where it was on the melting curve as both a liquid and a solid. This was using Pomeranchuk cooling. Pressure changes were observed in the liquid (initially thought to be in the solid) where the second order transitions in A and A' were eventually found to be due to the transition from the normal fluid to the A phase. This state is similar to the phase postulated by Anderson, Brinkman, and Morel (ABM) [30]. The first order phase transitions B and B' were also shown to be due to the transition from the A phase to the B phase. The B phase has similar properties to the Balian Werthamer phase that was predicted in [31]. This gives the phase diagram shown in figure 2.5.

The first thing to note is that the critical temperature T_c changes from 1 mK to 2 mK depending on the pressure. This has been examined by Greywall [32] and predicted by Anderson, Brinkman and Morel in 1961 [30].

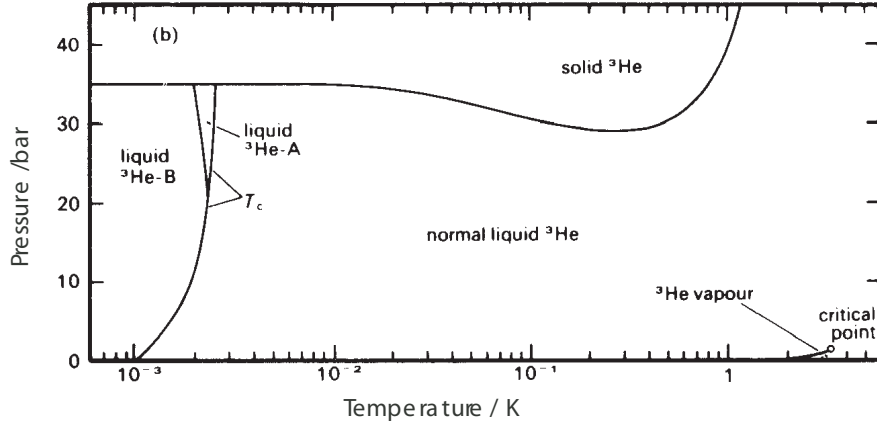


FIGURE 2.5: Phase diagram of ^3He [23].

At high pressures the liquid will first condense into the A phase and at lower pressures liquid ^3He will only condense into the B phase. Balian and Werthamer predicted this phase in 1963 [31]. The similarities between the Balian and Werthamer (BW) phase and the B phase, and the similarities between the A phase and the ABM phase were picked up by Leggett. For this discovery and for various other discoveries about the theory of the superfluid phases of ^3He Leggett was awarded the Nobel Prize in 2003 [33].

Under high magnetic fields the A Phase becomes more dominant. The measurements taken in this thesis are not under high magnetic field or under high pressure. Therefore the experiment is in the B phase and this phase is what will be discussed.

2.2.1 The Ballistic Regime

In ^3He there is a regime in which the mean free path of excitations is larger than the distance between the walls of the experimental cell. This is known as the ballistic regime. This regime is known to dominate at temperatures that are lower than $0.3T_c$ in cells of the size of the order of centimetres where T_c is the critical temperature of superfluid ^3He which is $929\ \mu\text{K}$ [34] as then the mean free path of the quasiparticles l is larger than the size of the cell and increases exponentially with decreasing temperature as $l \propto e^{\frac{\Delta}{k_B T}}$ [29]. As the measurements in this thesis are at around $100\ \mu\text{K}$ then this means that this experiment is in the ballistic regime.

2.3 Properties of $^3\text{He-B}$

The properties of a phase similar to $^3\text{He-B}$ were predicted by Balian and Werthamer [31] and then the similar properties between this theoretical phase and the B phase of ^3He were deduced by Leggett. The energy needed to break a Cooper pair and create Bogoliubov quasiparticles in this phase was found to be isotropic in k -space by Leggett with a value of [35]

$$\Delta_0 = 1.76k_B T_c. \quad (2.5)$$

Plugging this into equation 2.4 this gives

$$v_L = \frac{\Delta_0}{p_F}. \quad (2.6)$$

This gives a Landau critical velocity for $^3\text{He-B}$ of 27 mm/s. The pair breaking critical velocity that has been seen for wires in superfluid $\frac{1}{3}$ of the Landau velocity. This will be explained in Section 2.10.

2.4 Vibrating Wire Theory

All of the tuning forks and wires in the cell can be modelled as a mass on a spring as long as all of the damping on the probe is defined properly. A simple mass on a spring will have a restoring force of kx as well as a driving force $m\ddot{x}$. Hooke's law gives us the angular frequency of this mass in terms of the spring constant k and the effective mass m .

$$\omega = \sqrt{\frac{k}{m}}. \quad (2.7)$$

There are two extra forces that affect the probe in liquid ^3He that do not apply to a mass on a spring. These effects provide the damping to the resonator γ which is given by

$$\gamma = \gamma_2 + i\gamma_1. \quad (2.8)$$

In this equation γ_2 describes the dissipative force on the paddle and γ_1 is the non dissipative drag due to backflow over the resonator. This gives a total force on the probe F of

$$\frac{F}{m} = \ddot{x} + \gamma_2 \dot{x} + i\gamma_1 \dot{x} + \omega_0^2 x, \quad (2.9)$$

where ω_0 describes the natural resonant frequency of the wire with no external damping which can be seen when the wire's in a vacuum and m is the effective mass of the wire. The displacement of the wire is related to the angular frequency by the equation $x = x_0 e^{i\omega t}$. This equation is then used to find the displacement and acceleration of the wire as a function of velocity which is inserted into equation 2.9 and rearranged to give

$$\dot{x} = \frac{F}{m} \frac{\omega^2 \gamma_2 + i\omega(\omega_0^2 - \omega^2 - \omega\gamma_1)}{(\omega_0^2 - \omega^2 - \omega\gamma_1)^2 + \omega^2 \gamma_2^2}, \quad (2.10)$$

where equation 2.10 has both real (\mathbb{R}) and imaginary (\mathbb{J}) components with the real component given by equation 2.11 and the imaginary component given by equation 2.12.

$$\mathbb{R}(\dot{x}) = \frac{F}{m} \frac{\omega^2 \gamma_2}{(\omega_0^2 - \omega^2 - \omega\gamma_1)^2 + \omega^2 \gamma_2^2}, \quad (2.11)$$

$$\mathbb{J}(\dot{x}) = \frac{F}{m} \frac{i\omega(\omega_0^2 - \omega^2 - \omega\gamma_1)}{(\omega_0^2 - \omega^2 - \omega\gamma_1)^2 + \omega^2 \gamma_2^2}. \quad (2.12)$$

The real component is called the in phase component and the imaginary component is called the quadrature. This is seen experimentally in ^3He which is shown in figure 2.6.

In figure 2.6 the relation between frequency f and angular frequency ω is given by $f = \frac{\omega}{2\pi}$. The maximum in phase velocity of the resonance is given when

$$(\omega_0^2 - \omega_f^2 - \omega_f \gamma_1) = 0, \quad (2.13)$$

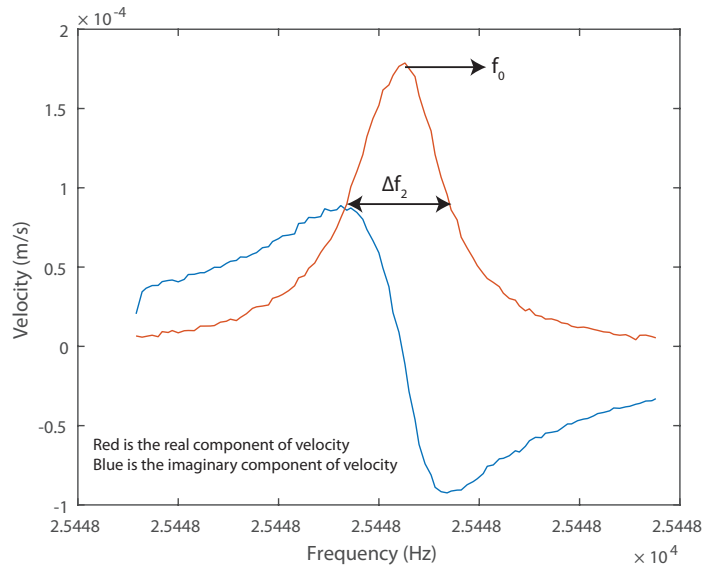


FIGURE 2.6: A resonance of one of the probes in the cell when it was in superfluid helium 3. f_0 is the resonant frequency where Δf_2 is the full width at half maximum where the red line shows the real component of velocity and the blue line is the imaginary component of velocity.

where ω_f is the resonant frequency in liquid ^3He which replaces ω in equation 2.11.

Given this condition the equation 2.11 reduces down to

$$\Re(\dot{x}) = \frac{F \omega^2 \gamma_2}{m \omega^2 \gamma_2^2} = \frac{F}{m \gamma_2}. \quad (2.14)$$

Using equation 2.13 the frequency shift of the probe due to backflow can be known.

Assuming that $\omega_f \gg \gamma_1$ then

$$\Delta f_1 = \frac{\gamma_1}{4\pi}. \quad (2.15)$$

In this equation $\Delta f_1 = \frac{\Delta\omega_1}{2\pi}$ and $\Delta\omega_1 = \omega_0 - \omega_f$. The variable Δf_1 defines the frequency shift between the resonance in vacuum and the resonance of the wire in liquid helium. From equations 2.11 we can find the full width at half maximum (FWHM) which is also defined as Δf_2 in figure 2.6. The value of the real component of velocity is at half its maximum when

$$(\omega_0^2 - \omega_{\frac{1}{2}}^2 - \omega_{\frac{1}{2}} \gamma_1^2)^2 = \omega_{\frac{1}{2}}^2 \gamma_2^2, \quad (2.16)$$

where if $\gamma_2 \ll \omega_{\frac{1}{2}}$ it simplifies to

$$\omega_{\pm\frac{1}{2}} = \frac{\gamma_1 \pm \gamma_2}{2}, \quad (2.17)$$

which gives a width Δf_2 of the resonance of $\frac{\omega_{+\frac{1}{2}} - \omega_{-\frac{1}{2}}}{2\pi}$ giving

$$\Delta f_2 = \frac{\gamma_2}{2\pi}. \quad (2.18)$$

The width of the resonance Δf_2 is taken as the difference between the two frequencies where the real component of the velocity was at half its height. By combining equation 2.18 and equation 2.14 we find that the maximum real velocity v_0 can be determined as a function of force F , mass m and the resonant width Δf_2 as

$$v_0 = \frac{F}{2\pi m \Delta f_2}. \quad (2.19)$$

This equation can be rearranged to give a value of height times width over drive (HWD). This is given by

$$\frac{\Delta f_2 v_0}{F} = \frac{1}{2\pi m} = \text{HWD} \sim \text{const.} \quad (2.20)$$

The HWD should stay constant and it is only dependent on the effective mass of the wire m . As the mass of the backflow over the resonator due to the non dissipative drag is far smaller than the mass of the resonator this means that the HWD is roughly constant. Because of this the HWD can be used to infer the width and therefore the temperature of the experiment as the velocity and force on the probe can be found experimentally.

2.5 1D Simplification of the Damping Force on a Paddle in an Ideal Gas

Figure 2.7 is a example of an ideal gas exchanging momentum with a paddle. This model works below $0.3T_c$ at cell sizes of the order of centimetres where the particles act according to the ballistic regime.

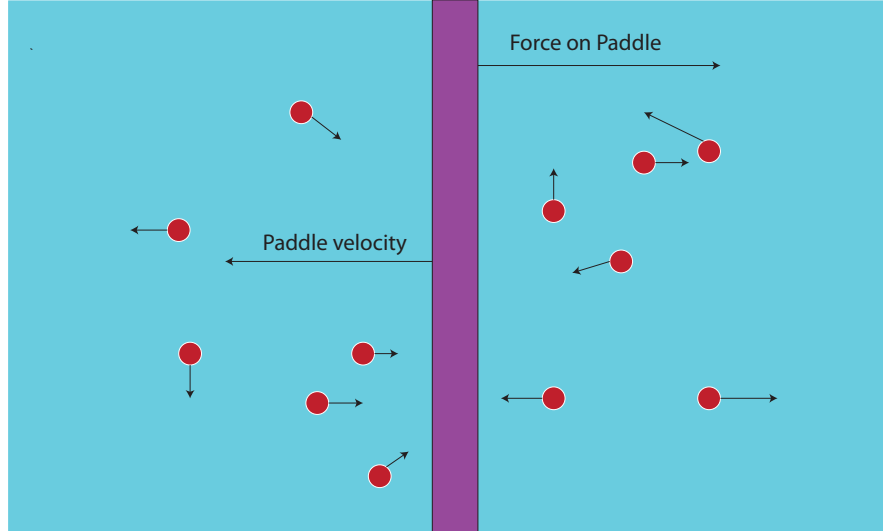


FIGURE 2.7: A two dimensional model paddle moving through a gas.

The paddle with area A is travelling with a velocity v and has a force F exerted by the particles around it. The particles are travelling with a group velocity of v_g and it is assumed that there are the same number $\frac{n}{2}$ of particles on both sides of the paddle. The force on the paddle can be expressed as

$$F = F_{Front} - F_{Back}. \quad (2.21)$$

The effective velocity of particles from the front hitting the paddle is $v_g + v$ and the momentum is p_F . This means that there is $2p_F$ of momentum exchange between the paddle and the particle. Using this the force of the particles is given as the number of particles hitting the paddle n times the relative velocity of the particles which is given as $\langle n(v_g + v) \rangle$ for particles hitting the front face of the paddle and $\langle n(v_g - v) \rangle$ for particles hitting the back of the paddle times the momentum of the particles p_F

$$F = A \langle n(v_g + v) \rangle p_F - A \langle n(v_g - v) \rangle p_F = 2Ap_F \langle nv \rangle. \quad (2.22)$$

This model is a good basis for understanding what happens to particles that hit a paddle. However this model estimates a larger force on the paddle than what is measured experimentally for quasiparticles in superfluid ^3He . This is because the model does not take into account a process called Andreev reflection which perfectly retro-reflects quasiparticles before they interact with the paddle.

2.6 Force on a Paddle With Respect to Andreev Reflection

Andreev reflection is the perfect retroreflection of a hole/particle into a particle/hole at an interface between a superconducting state and a normal state or a superfluid state and a normal state.

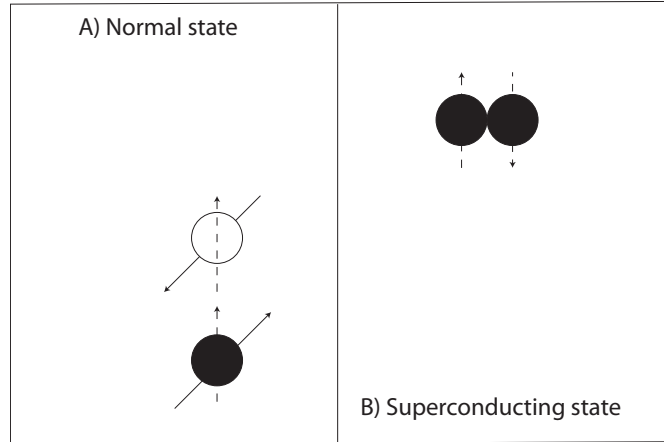


FIGURE 2.8: Andreev reflection between a normal state A) and a superconducting state B). Particles are filled in black while Holes are filled in white. Dotted lines indicate the spin of the particle where filled lines indicate the momentum.

In figure 2.8 a quasiparticle travelling with a momentum p hits a barrier between a normal and superconducting state. The particle retroreflects into a quasihole with momentum $+p$ and forms a Cooper pair in the superconducting state. This process was first found in superconductors [36], but can be applied to superfluids as well [37] whenever there is a change in the dispersion curve of ^3He .

Figure 2.9 is a one dimensional model that takes into account Andreev reflection in order to find the force on the paddle due to quasiparticle interaction. This model considers the dispersion curves of the superfluid around the paddle 2) and the front 1) and back 3) of the paddle with the paddle moving at a velocity v to the left .

This figure shows the dispersion curves for various quasiparticles and quasiholes around the paddle. This explains how both quasiparticles (A and C) and quasiholes(B and D) are affected by the local movement of superfluid ^3He shown in Part 2) of figure 2.9 .

Both quasiparticle A and quasihole D have enough energy to fill a state in the dispersion curve of the moving superfluid. The forces on the paddle from A and D are equation 2.23 and equation 2.24.

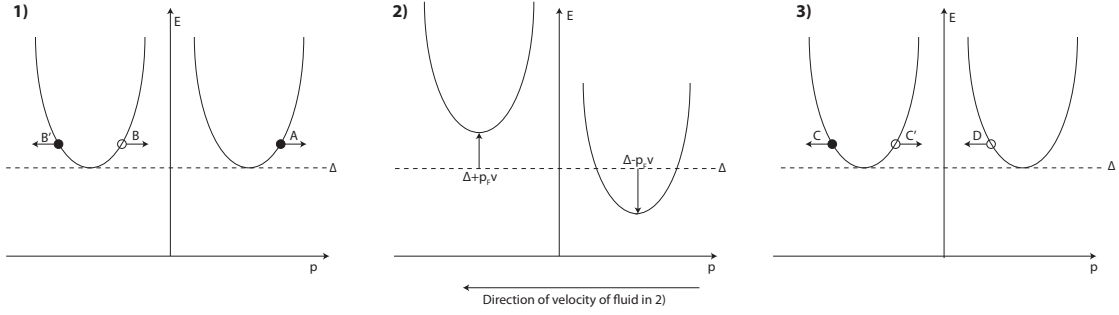


FIGURE 2.9: Andreev reflection in the superfluid with the fluid at rest in the front of the paddle in part 1) and the back of the paddle in part 3) where the fluid part 2) is moving with a velocity v towards the front 1). Δ is the energy gap needed to create excitations when the fluid is stationary.

$$F_A = Anp_F(v_g + v). \quad (2.23)$$

$$F_D = Anp_F(v_g - v). \quad (2.24)$$

As $v_g \gg v$ then we can remove v from the equation and then summate the forces.

$$F_A + F_D = 2Ap_F \langle nv_g \rangle. \quad (2.25)$$

For C and B only a fraction of the particles will be able to transmit through the barrier. The rest of the quasiparticles are Andreev reflected into their alternate counterparts shown by C' and B'.

$$F_B = -Anp_F(v_g - v)f_T. \quad (2.26)$$

$$F_C = -Anp_F(v_g - v)f_T. \quad (2.27)$$

$$F_B - F_C = -2Ap_F \langle nv_g \rangle f_T. \quad (2.28)$$

Summing the forces from all quasiparticles and quasiholes therefore gives

$$F = 2Ap_F \langle nv_g \rangle (1 - f_T). \quad (2.29)$$

In this equation A and p_F are known but the average excitation flux $\langle nv_g \rangle$ and the fraction transmitted f_T aren't known but can be derived. Because the density of quasiparticles in the superfluid is dependent on temperature then the force F in this equation can be defined as the thermal force F_T .

2.6.1 Calculating the Temperature Using the Thermal Force

Putting the fraction transmitted back into the previous definition of the thermal force equation 2.29 we get that the thermal force F_T is given by

$$F_T = 2Ap_F \langle nv_g \rangle \gamma(1 - f_T). \quad (2.30)$$

γ is a geometrical constant which explains how the area of the paddle interacts with the quasiparticle flux. Using the definition of the width of the resonance given by equation 2.19 and rearranging we find that

$$F_T = 2\pi m \Delta f_2 v, \quad (2.31)$$

where m is the effective mass of the resonator in equation 2.19. The definition of F_T given by equation 2.31 can be put into equation 2.30. This equation can then be rearranged to give

$$\Delta f_2 = \frac{Ap_F \gamma}{\pi m v} \langle nv_g \rangle (1 - f_T), \quad (2.32)$$

where f_T has been found in section 2.7 to be $e^{-\lambda p_F v / (k_B T)}$ (equation 2.49). Taking this at the low velocity limit the Taylor expansion can be used to find the first two terms of e^{-x} as $1 - x$. Substituting this in gives the equation below which can then be rearranged into equation 2.34.

$$\Delta f_2 = \frac{Ap_F \gamma}{\pi m v} \langle nv_g \rangle \lambda p_F v / k_B T. \quad (2.33)$$

$$\Delta f_2 = \frac{Ap_F^2 \gamma \lambda}{\pi m k_B T} \langle n v_g \rangle. \quad (2.34)$$

The quasiparticle flux $\langle n v_g \rangle$ is defined in equation 2.54. Inserting equation 2.54 into equation 2.34 gives

$$\Delta f_2 = B e^{-\Delta/k_B T}. \quad (2.35)$$

Where the constant B is given by

$$B = \frac{Ap_F^2 \gamma \lambda}{\pi m} v_F(\varepsilon) g(\varepsilon). \quad (2.36)$$

In equation 2.36 the value of the Fermi velocity is given in [6]. This gives a value of B for the resonator of $6.67 \times 10^5 \text{ s}^{-1}$ using values of γ and λ calculated later in this thesis. The value of this constant that was used in the temperature calculations was calculated previously as $5.07 \times 10^5 \text{ s}^{-1}$. The logarithms of both sides of equation 2.35 can then be taken to find the temperature as

$$\log\left(\frac{\Delta f_2}{B}\right) = -\Delta/k_B T. \quad (2.37)$$

As Δ is $1.76 k_B T_c$ this equation can then be reduced down to

$$\log\left(\frac{\Delta f_2}{B}\right) = -\Delta_0/k_B T, \quad (2.38)$$

where T_c is the critical temperature of ^3He which is 929 μK . Rearranging this equation we find that

$$T = \frac{\Delta_0}{\log\left(\frac{\Delta f_2}{B}\right)}. \quad (2.39)$$

The temperature can be used to find γ which is a geometrical constant of the order of unity which defines the sensitivity of the probe to quasiparticle damping.

2.7 The Fraction of Quasiparticles That are Transmitted Through the Potential Barrier Caused by a Moving Superfluid

The average flux of excitations that transfer momentum $\langle nv_g \rangle_T$ is defined as

$$\langle nv_g \rangle_T = \int_{\Delta + p_F v}^{\infty} g(\varepsilon) f(\varepsilon) v_g(\varepsilon) d\varepsilon. \quad (2.40)$$

where $g(\varepsilon)$ is the Density of States (DOS) of the fermions, $f(\varepsilon)$ is the Fermi distribution which is a function that defines the probability of a fermions occupying a specific energy level. This integral starts from the energy $\Delta + p_F v$ as that is the minimum energy the quasiparticle has to have in order to overcome the barrier created by the moving superfluid. $v_g(\varepsilon)$ is the group velocity of the excitations which is defined as

$$v_g(\varepsilon) = \frac{d\varepsilon}{dp} \quad (2.41)$$

where the total number of energy states in the system is the same as the total number of momentum states. This gives

$$g(\varepsilon) d\varepsilon = g(p) dp. \quad (2.42)$$

The average excitation flux can then be obtained. Because the density of energy states times the group velocity is the density of momentum states or $v_g(\varepsilon) \cdot g(\varepsilon) = g(p)$ this means that the group velocity and the density of energy states can be taken out of the integral as they together don't depend on energy as

$$\langle nv_g \rangle = g(p_F) \int_{\Delta + p_F v}^{\infty} f(\varepsilon) d\varepsilon. \quad (2.43)$$

From this the fraction transmitted can be found. This is by finding the flux of excitations above the energy of the potential barrier and dividing it by the total flux

$$f_T = \frac{\langle nv_g \rangle_T}{\langle nv_g \rangle}. \quad (2.44)$$

Which is converted to

$$f_T = \frac{g(p_F) \int_{\Delta+p_F v}^{\infty} f(\varepsilon) d\varepsilon}{g(p_F) \int_{\Delta}^{\infty} f(\varepsilon) d\varepsilon}. \quad (2.45)$$

The only part of this equation that is not cancelled out are the integrals of the Fermi distribution of energies. The Fermi distribution is given by

$$f(\varepsilon) = \frac{1}{e^{\varepsilon/k_B T} + 1}. \quad (2.46)$$

When the temperature approaches zero the term $e^{\varepsilon/k_B T}$ becomes much larger than 1. Because of this the Fermi distribution of energies can then be approximated to the Boltzmann distribution as

$$f(\varepsilon) \sim e^{-\varepsilon/k_B T}. \quad (2.47)$$

Plugging equation 2.47 into equation 2.45 the fraction transmitted can be found as

$$f_T = e^{-(\Delta+p_F v)/(k_B T)} - e^{-\Delta/(k_B T)}. \quad (2.48)$$

Which reduces down to

$$f_T = e^{-\lambda p_F v/(k_B T)}. \quad (2.49)$$

Where λ is a geometrical constant that is introduced in order to explain non-linear damping exhibited when the paddle is at a high velocity. This geometrical factor is of the order of unity.

2.8 Calculating the Quasiparticle Flux $\langle nv_g \rangle$

Using the definition of $\langle nv_g \rangle$ given by equation 2.43 and using the Fermi distribution of energies f_ε given by equation 2.47 we find that

$$\langle nv_g \rangle = g(p_F) \int_{\Delta}^{\infty} e^{-\varepsilon/k_B T} d\varepsilon. \quad (2.50)$$

Integrating f_ε we find that

$$\langle nv_g \rangle = g(p_F) k_B T \left[e^{-\varepsilon/k_B T} \right]_{\Delta}^{\infty}. \quad (2.51)$$

This then gives

$$\langle nv_g \rangle = g(p_F) k_B T e^{-\Delta/k_B T}, \quad (2.52)$$

where the Fermi velocity is 59 m/s at 0 bar given by [6], and the DOS of fermions $g(\varepsilon_F)$ in ^3He can be calculated from $g(\varepsilon_F) = \frac{m^* k_F}{\pi \hbar}$ [38]. In this equation m^* is the effective mass which is 2.8 times the mass of ^3He at 0 bar [6] and k_F is the wavevector of the quasiparticle flux which is related to the Fermi momentum p_F and the Planck constant \hbar by $k_F = \frac{p_F}{\hbar}$. Substituting this in gives

$$g(\varepsilon) = \frac{2.8 m p_F}{\pi \hbar^2}. \quad (2.53)$$

Where p_F is 8.28×10^{-25} kgm/s at 0 bar as given by [6] which gives a value of $g(\varepsilon)$ at 0 bar of $3.15 \times 10^{51} \text{ J}^{-1} \text{ m}^{-3}$. This gives a final expression for the quasiparticle flux $\langle nv_g \rangle$ of

$$\langle nv_g \rangle = v_F(\varepsilon) \frac{2.8 m p_F}{\pi \hbar^2} k_B T \cdot e^{-\Delta/k_B T} \quad (2.54)$$

The value of Δ in this calculation is given by $k_B(T + 1.76T_C)$ where T_C is the critical temperature of ^3He which is 929 μK . Using this information an estimate of the quasiparticle flux at 110 μK of $3.6519 \times 10^{19} \text{ m}^{-2} \text{ s}^{-1}$ can be obtained.

2.9 Finding the Geometrical Constant λ

λ is a geometrical constant that can be calculated from the thermal force. Therefore the thermal force must first be found. The thermal force can be deduced by subtracting all the other forces in the cell from the total force on the probe which takes the form of

$$F_T = F - F_I - F_{ex}. \quad (2.55)$$

where the forces acting on a probe are the thermal force F_T which is due to quasiparticles interacting with the probe, the intrinsic force F_I which is damping due to mechanical processes in the probe, and the non-linear damping force that is created by driving the probe to high velocities F_{ex} . Once we have found the thermal force then we can use equation 2.30 in order to find λ .

$$F_T = C(1 - e^{-\lambda v_*}). \quad (2.56)$$

Where v_* is the reduced velocity given by $v_* = \frac{p_F v}{k_B T}$. When the thermal force is divided by its derivative we get

$$\frac{F_T}{\frac{dF_T}{dv_*}} = \frac{1 - e^{-\lambda v_*}}{\lambda}. \quad (2.57)$$

This is called the reduced force. By plotting the reduced force against the reduced velocity we can therefore find the value of λ using this equation.

2.10 Pair Breaking Critical Velocity

In Lambert's paper [39], the velocity of the superfluid on the surface of the wire is related to the velocity of the wire by $v_\theta = -v(1 + \frac{a^2}{r^2}) \sin(\theta)$ where v_θ is the radial component of the superfluid velocity, v is the velocity of the wire, r is the radius of the wire, a is the distance between the superfluid and the middle of the wire and θ is the angle between the direction of travel of the superfluid and the surface of the wire. This gives a maximum radial velocity of $2v$ at $\theta = \pm \frac{\pi}{2}$ and $r = a$ which gives $2p_F v$ as the highest energy of the quasiparticle local to the wire as at rough surfaces the energy gap Δ is zero due to the existence of trapped quasiparticles on the wires surface.

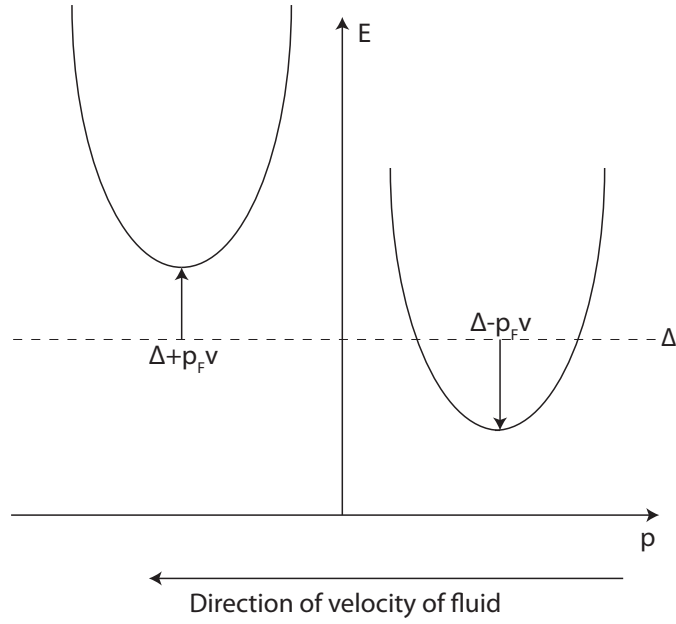


FIGURE 2.10: The dispersion curve of the bulk ${}^3\text{He}$ next to a wire moving at velocity v .

The quasiparticle energy of the superfluid next to the wire needs to be greater than the minimum energy of the quasiparticles in the bulk superfluid in order for the quasiparticle to escape into it; where the minimum energy of the bulk superfluid dispersion curve is $\Delta - p_F v$ as shown in figure 2.10. Putting this into an equation gives

$$\Delta - p_F v = 2p_F v. \quad (2.58)$$

This tidies up to

$$v = \frac{v_L}{3}, \quad (2.59)$$

where v is the pair breaking critical velocity, v_L is the Landau critical velocity, Δ is the energy gap and p_F is the Fermi momentum. This equation estimates a pair breaking critical velocity of a wire of 9 mm/s which is seen experimentally in Carney's paper [40]

2.11 Black Body Radiator Description

The Black Body Radiator is an object which absorbs all incoming radiation and emits a beam of radiation itself. In this experiment the main form of radiation that the BBR absorbs and emits are quasiparticles. In order to measure the quasiparticle flux inside the BBR there is a thermometer wire and in order to create a quasiparticle beam the BBR has a heater wire. The BBR is normally warmer than the rest of the cell as its only thermal connection to the rest of the cell is through the small hole in its wall.

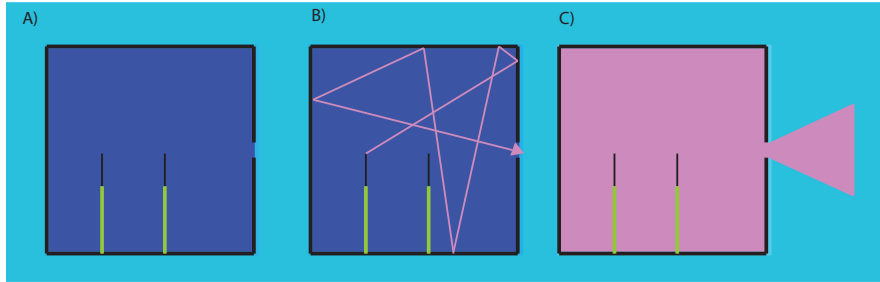


FIGURE 2.11: Thermalization of quasiparticles in the BBR where A) is the BBR without the heater wire on, B) is the BBR with the heater wire driven by a low driving force, and C) is the BBR with the heater wire driven by a high driving force.

The main use of the BBR in this experiment is to create a quasiparticle beam. In order to find the power emitted by the quasiparticle beam the power from the heater wire had to be calibrated against a parameter called the width parameter (WP) which is used to calibrate the BBR. The width parameter is defined as

$$WP = \Delta f_2 T k_B (T + \Delta_0 / k_B), \quad (2.60)$$

in which there should be a linear relationship between the width parameter and power of a BBR. By finding the coefficients of this fit the power of the BBR can be determined. This calibration is very useful as the power given out by the box can be dependent on the magnetic field strength. Thus for any measurements that need the quasiparticle beam the power can then be found from the temperature of the box instead of looking at the field dependent faraday voltage. This will be explained in the preliminary measurements section.

This calibration can be used to find the geometrical constant γ which defines the sensitivity of a probe to quasiparticles. In order to find this relation we must first look back

at Eq. (2.30) which defines the thermal force and correlate it to the definition of thermal force shown below

$$F_T = 2\pi m \Delta f_2 v, \quad (2.61)$$

where m is the mass of the probe, Δf_2 is the width of the resonance of the probe shown in section 2.4 and v is the velocity of the probe. When these two equations are correlated a relationship between the width of the resonance and the quasiparticle flux $\langle nv_g \rangle$ is found

$$\Delta f_2 = \frac{\gamma d p_F^2}{\pi m_l k_B T} \langle nv_g \rangle. \quad (2.62)$$

In this equation m_l is defined as the mass per unit length of the wire and d is the diameter of the wire. The only unknown parameter in this equation is the quasiparticle density $\langle nv_g \rangle$. The quasiparticle density is related to the flux of quasiparticles \dot{N} going out of the BBR hole in the following way

$$\dot{N} = \frac{A_H \langle nv_g \rangle}{4\pi} \int_0^{\pi/2} \cos(\theta) \sin(\theta) d\theta \int_0^{2\pi} d\phi. \quad (2.63)$$

Where A_H is the area of the hole of the BBR, θ is the angle from the apex of the cap generated from the BBR and ϕ is the angle which defines where on the x-y plane normal to the direction of the quasiparticle beam. This reduces down to equation 2.64. The fraction is $\frac{2}{4}$ instead of $\frac{1}{4}$ in order to take into account the quasiholes leaving the BBR

$$\dot{N} = \frac{2}{4} A_H \langle nv_g \rangle \quad (2.64)$$

The flux of quasiparticles \dot{N} is related to the power by $\dot{N} = \frac{\dot{Q}}{\langle E \rangle}$ where $\langle E \rangle$ is the mean quasiparticle energy in the BBR which is defined as $\langle E \rangle = \Delta + k_B T$ in which Δ is the energy gap in ^3He and $k_B T$ is the thermal energy of the quasiparticles. Using these equations $\langle nv_g \rangle$ can be defined as

$$\langle nv_g \rangle = \frac{2\dot{Q} \langle E \rangle}{A_H}. \quad (2.65)$$

Plugging this into equation 2.62 and rearranging we find that the BBR calibration gives

$$\frac{\Delta f_2 \langle E \rangle T}{\dot{Q}} = \frac{2dp_F^2 \gamma}{\pi k_B m_l A_H}, \quad (2.66)$$

where $\Delta f_2 \langle E \rangle T$ is the width parameter which is given by equation 2.60. This is useful as γ can be determined from this calibration. Also by using this calibration the power of the BBR can be calculated when the width parameter of the BBR is known. This is useful for when the magnetic field has changed between one BBR measurement and the next.

2.11.1 Damping Predictions

By using the definition of the quasiparticle density and some geometrical arguments the damping on the forks due to the BBR can be predicted. These measurements can then be compared against the experimental data. The quasiparticle density $\langle nv_g \rangle^F$ that reaches the fork is related to the quasiparticle flux $d\dot{N}$ by $\langle nv_g \rangle^F = \frac{d\dot{N}(\theta)}{dA}$ where dA is the area element the quasiparticles are going through and $d\dot{N}(\theta)$ is defined as the number of quasiparticles going through the area element every second.

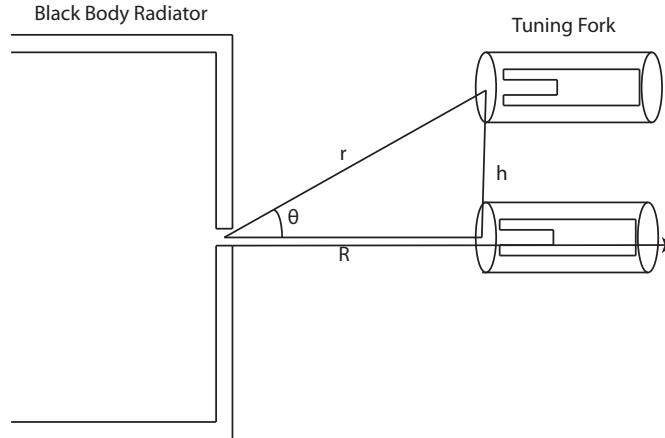


FIGURE 2.12: A diagram showing the angle between the quasiparticle beam and the tuning fork. Note: this is a 2D sketch of a 3D situation.

In order to find the size of the area element dA and the rate of quasiparticles going through that element $d\dot{N}$ a model containing the probe and BBR needed to be created. This model is shown in figure 2.12 and in this model the beam creates a cap with radius r and an area element dA where $dA = 2\pi r \sin(\theta) r d\theta$ where the 2π defines the sum

of all the ϕ components. Also in this equation the radius of the sphere r is given as $r = R/\cos(\theta)$ where R is the closest distance from the BBR to the camera and h is the distance from the closest point of the camera to the tuning fork that is being estimated. Using this information we can derive that

$$\langle nv_g \rangle^F = \frac{d\dot{N}(\theta) \cos(\theta)^2}{2\pi R \sin(\theta) R d\theta}, \quad (2.67)$$

where the value of $d\dot{N}(\theta)$ is the rate of quasiparticles coming out of the BBR given by $d\dot{N}(\theta) = A_H \langle nv_g \rangle \cos(\theta) \sin(\theta) d\theta$ with A_H being the area of the BBR hole. Using this equation we can see that $\langle nv_g \rangle^F$ turns into

$$\langle nv_g \rangle^F = \frac{A_H \cos^4(\theta)}{2\pi R^2} \langle nv_g \rangle^{BBR}, \quad (2.68)$$

where the BBR superscript means for the black body radiator. This can be converted into a power using equation 2.65 which gives

$$Q^F = \frac{A_P \cos^4(\theta)}{2\pi R^2} Q^{BBR}. \quad (2.69)$$

The extra $\cos(\theta)$ term comes in because the quasiparticle flux comes into the tuning fork at an angle θ . Plugging equation 2.68 back into equation 2.62 and converting for a fork we can now see how the damping on a fork is affected by the quasiparticle flux coming from the BBR ($\langle nv_g \rangle^{BBR}$)

$$\Delta f_2^F = \frac{\gamma W^F p_F^2}{\pi m_l k_B T^F} \frac{A_H \cos^2(\theta)}{2\pi R^2} \langle nv_g \rangle^{BBR}. \quad (2.70)$$

Using equation 2.62 for the wire in the BBR and then rearranging gives

$$\langle nv_g \rangle^{BBR} = \frac{\pi m_l^W k_B T^W}{\gamma^W p_F^2 d} \Delta f_2^W. \quad (2.71)$$

Plugging the quasiparticle density equation 2.71 into the equation for damping (equation 2.70) and then rearranging we find that

$$\Delta f_2^F T^F = \frac{\gamma^F m_l^W W^F}{\gamma^W m_l^F d^W} \frac{A_H \cos^2(\theta)}{2\pi R^2} \Delta f_2^W T^W. \quad (2.72)$$

The resonant width and temperature of the wire is related to the power of the BBR in the following way

$$\Delta f_2^W T^W = \frac{c\dot{Q}}{\langle E \rangle}, \quad (2.73)$$

where c is a constant derived by plotting the width parameter of the BBR against power. Plugging equation 2.73 into equation 2.72 we find that

$$\Delta f_2^F T^F \langle E \rangle = \frac{\gamma^F m_l^W W^F}{\gamma^W m_l^F d^W} \frac{A_H \cos^4(\theta)}{2\pi R^2} cQ. \quad (2.74)$$

Changing the mass of the wire and fork into densities then gives us

$$\Delta f_2^F T^F \langle E \rangle = \frac{\gamma^F \rho^W d^W}{\gamma^W \rho^F t^F} \frac{A_H \cos^4(\theta)}{2R^2} cQ, \quad (2.75)$$

where $\Delta f_2^F T^F \langle E \rangle$ is the predicted width parameter of the fork when the BBR is at a certain power. This predicted width parameter can then be used as a comparison to the experimental width parameter.

2.12 Finding the Geometrical Constant γ

The geometrical constant γ is related to the sensitivity of a probe to quasiparticle damping. In order to find γ the power and width parameter of a probe need to be known. This is possible for a black body radiator as it contains a heater and thermometer, however for objects that cannot measure the width parameter and power they need to be calibrated from objects where γ is known.

2.12.1 Finding γ for a BBR

Once the BBR calibration is found then γ is relatively easy to calculate from equation 2.66. In this equation the mass per unit length m_l for a wire is given by $m_l = \rho^w \pi d^2/4$ and m_l for a fork is given by $m_l = \rho^F W t_F/4$ where d is the diameter of the wire, ρ_w is the wire density, ρ^F is the fork density, W is the width of the fork tine, and t_F is the thickness of the fork tine. Putting this new information into equation 2.66 gives

$$\gamma = \frac{\Delta f_2 \langle E \rangle T}{\dot{Q}} \frac{\pi^2 k_B \rho^w d}{8 p_F^2} A_H, \quad (2.76)$$

for a wire and

$$\gamma = \frac{\Delta f_2 \langle E \rangle T}{\dot{Q}} \frac{\pi k_B \rho^F t^F}{8 p_F^2} A_H, \quad (2.77)$$

for a tuning fork. Finding γ is useful as it shows how sensitive the thermometer wire in the BBR is to quasiparticle damping. Using γ for a fork the power entering the pixel can be implied from a rearrangement of the previous equation.

$$\dot{Q}^F = \Delta f_2 \langle E \rangle T \frac{\pi k_B \rho^F t^F}{8 p_F^2 \gamma} A_P. \quad (2.78)$$

This can be useful in finding out how efficient a bolometer is. By comparing \dot{Q}^F with the power emitted from the BBR we can find out what percentage of the power from the BBR goes into each one of the pixels.

2.12.2 Using γ From One Tuning Fork in Order to Determine γ for Another Fork in Thermal Equilibrium with the First

Assuming that a fork sitting in a hole in a copper block is a BBR we can determine γ for that fork. The exact method for doing this is explained in Section 4.2.3. Sometimes it is not easy to use this method on a particular fork to determine γ . In that case as long as both forks are in thermal equilibrium then by knowing the value of γ for one fork then the value of γ for another can be determined. Going back to equation 2.62 and slightly modifying it we find that the quasiparticle damping on a fork is given by

$$\Delta f_2^F = \frac{\gamma^F W^F p_F^2}{\pi m_l k_B T^F} \langle n v_g \rangle^F, \quad (2.79)$$

where using the superscript F means for fork and the superscript W stands for wire. Assuming that the temperature and quasiparticle flux hitting both of the forks is the same we can say that

$$\langle n v_g \rangle^F = \Delta f_2^{F2} \frac{\pi m_l k_B T^F}{\gamma^{F2} W^F p_F^2}. \quad (2.80)$$

Putting this value of $\langle n v_g \rangle^F$ into equation 2.79 we find that

$$\Delta f_2^F = \frac{\gamma^F W^F p_F^2}{\pi m_l k_B T^F} \Delta f_2^{F2} \frac{\pi m_l k_B T^F}{\gamma^{F2} W^F p_F^2}. \quad (2.81)$$

Since the only factor that is different between the forks is γ this condenses down to equation 2.82.

$$\gamma^{F2} = \frac{\gamma^F \Delta f_2^{F2}}{\Delta f_2^F}. \quad (2.82)$$

This equation assumes thermal equilibrium between the forks being measured and that the mass per unit lengths m_l and the widths of the forks W^F are the same. Using equation 2.82 the values of γ for all tuning forks in the cell can be determined.

2.12.3 Finding γ for One Wire Using γ From Another Wire in Thermal Equilibrium With It

If two wires are in thermal equilibrium the properties of one wire can then be used to determine the properties of the second. We will start by modifying equation 2.62 for one of the wires

$$\Delta f_2^W = \frac{\gamma^W d^W p_F^2}{\pi m_l^W k_B T^W} \langle n v_g \rangle^W, \quad (2.83)$$

where the superscript W stands for wire. This equation can also be made for the second wire

$$\Delta f_2^{W2} = \frac{\gamma^{W2} d^{W2} p_F^2}{\pi m_l^{W2} k_B T^{W2}} \langle n v_g \rangle^{W2}. \quad (2.84)$$

In this equation $\langle n v_g \rangle^{W2}$ is the same as $\langle n v_g \rangle^W$ and the temperature of both wires is the same. Rearranging the last equation in terms of $\langle n v_g \rangle^W$ we find

$$\langle n v_g \rangle^W = \frac{\Delta f_2^{W2} \pi m_l^{W2} k_B T^{W2}}{\gamma^{W2} d^{W2} p_F^2}. \quad (2.85)$$

Plugging this equation into equation 2.83 we find

$$\Delta f_2^W = \frac{\gamma^W d^W \Delta f_2^{W2} m_l^{W2}}{m_l^W \gamma^{W2} d^{W2}}. \quad (2.86)$$

As the mass per unit length of the wire m_l is given by $m_l^W = \frac{\pi}{4} \rho^W d^W$. Rearranging for γ^{W2} we find that

$$\gamma^{W2} = \gamma^W \frac{\rho^{W2} \Delta f_2^{W2} d^{W2}}{\rho^W \Delta f_2^W d^W}. \quad (2.87)$$

m_l is slightly different for one of the wires in the cell. For this wire is defined as $m_l^W = \rho^W d^W$. Putting this into equation 2.86 we get

$$\gamma^{W2} = \gamma^W \frac{4 \rho^{W2} \Delta f_2^{W2} d^{W2}}{\pi \rho^W \Delta f_2^W d^W}. \quad (2.88)$$

This is useful if there are two wires are in thermal equilibrium with one another where the value of γ of one of those wires is known.

2.13 Chapter Summary

This chapter explained the theory behind the measurements that took place. The properties and phases of ^3He were discussed as well as the properties of quasiparticle damping

in $^3\text{He-B}$. We then discussed Andreev reflection and created a new model of quasiparticle damping in $^3\text{He-B}$ in order to take this phenomenon into account. This new model was then used to find derivations for the temperature and two geometrical constants: the sensitivity of a probe to quasiparticles γ and the probes velocity dependence to thermal damping λ , where λ could be extracted from the reduced force and reduced velocity. γ was then found using 2 methods one of which was through a BBR calibration and the other was through the comparison of damping between two probes where the value of γ for one of these probes is known. Through the derivation of γ a theoretical model of the quasiparticle damping due to the BBR quasiparticle beam was utilised which explained the dependence of the frequency of the vibrating object on its velocity and force.

Chapter 3

Experimental Setup

In order to achieve temperatures of the order of $100\ \mu\text{K}$, required for measurements in the ballistic regime of superfluid ^3He , the experimental volume (cell) was mounted onto a Lancaster-style nuclear cooling stage, which was itself attached to The Lancaster Advanced Dilution Refrigerator [41] [42], which is capable of reaching temperatures as low as $2\ \text{mK}$ in continuous operation. During the precooling stage, a good thermal connection between the nuclear stage and the dilution refrigerator is needed. However, during adiabatic demagnetisation and afterwards, the nuclear stage must be isolated from the refrigerator, requiring a heat switch.

A large magnetic field ($\sim 7\ \text{T}$) is used to order the nuclear spins of the silver coated copper sheets around the cell [43] [44] while the cell is pre-cooled to a temperature of $\sim 5\ \text{mK}$ using the dilution refrigerator. The cell is then cooled to $100\ \mu\text{K}$ using adiabatic demagnetisation with a final field of $\sim 47\ \text{mT}$ in the magnet [45]. The temperature of the cell stays close to $100\ \mu\text{K}$ for around a week. It is during this week in the Adiabatic Demagnetisation cycle that all measurements pertaining to this thesis were taken.

3.1 Outline of the Cell

Figure 3.1 shows a general overview of the cell. Some of the early measurements in this cell are shown in the work of Ahlstrom et al. [46] and the thesis of Edward Guise [47]. The cell was built to image the quasiparticle beam profile from a Black Body Radiator (BBR) and a source wire that is called $\mu\mu\mu_3$, using a quasiparticle camera that consists

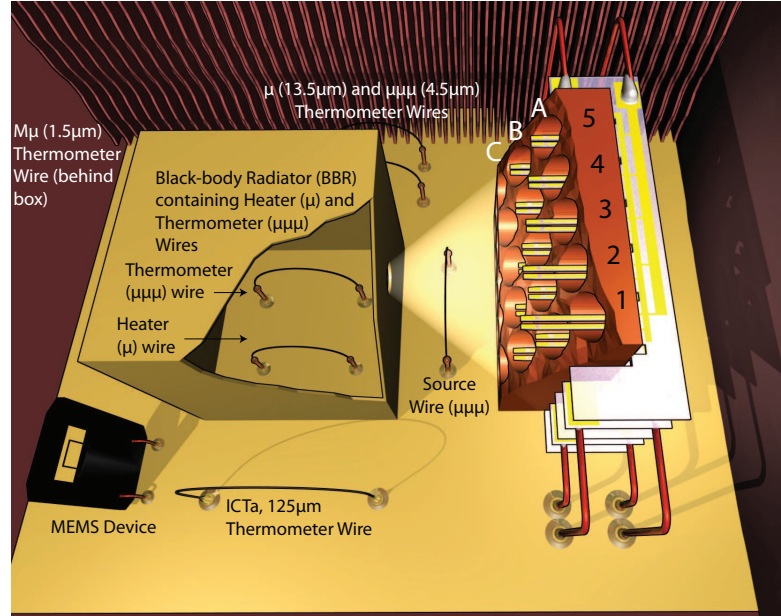


FIGURE 3.1: A diagram of the different components in the inner cell. All the $M\mu$ wires have a diameter of $1.5\ \mu\text{m}$, all $\mu\mu\mu$ wires have a diameter of $4.5\ \mu\text{m}$ and all μ wires have a diameter of $1.5\ \mu\text{m}$. All the wires shown in the diagram apart from ICTa and the MEMS are made from Niobium Titanate.

of 25 tuning forks. In order to find this beam profile the bulk temperature needs to be found and therefore there need to be instruments in the cell that are designed for thermometry. The main wires that are used for thermometry at high temperatures are the inner cell tantalum wire (ICTa) and the outer cell tantalum wire (OCTa) where OCTa is not shown in figure 3.1 as it is outside of the inner cell. Due to the high density of tantalum and their large diameters they cannot be used at low temperatures ($T \leq 150\ \mu\text{K}$).

All of the other vibrating wire resonators in the cell were constructed from multifilamentary NbTi wire. There are approximately 60 filaments in the wire and each filament has a diameter of $4.5\ \mu\text{m}$ or $13.5\ \mu\text{m}$. We use these to create so-called $\mu\mu\mu$ (triplemicro) and μ (single-micro)-wires, respectively. The $\mu\mu\mu$ -wires are typically used as thermometers and detectors, whilst μ -wires tend to be used as heaters. In the cell we have a megamicro ($M\mu$) wire which has a diameter of $1.5\ \mu\text{m}$. While all the wires in the cell except for ICTa and OCTa are effective thermometers at temperatures $\geq 100\ \mu\text{K}$, the $M\mu$ wire is the wire most commonly used for thermometry. This is because of two reasons. The first reason is that the wire is one of the most sensitive probes in the cell to temperature change. The second reason is that the probe is placed far away from most of the other probes in the cell which means that it won't register any heat leaks in

the cell from any of the other probes. The $M\mu$ has a leg spacing of 2.5 mm and is placed behind the BBR.

In order to verify the temperature reading from the $M\mu$ the wires $\mu\mu\mu_1$ and μ_1 were used with $\mu\mu\mu_1$ being a thermometer wire close to μ_1 . These wires are less reliable than the $M\mu$ as they are more likely to be affected by heat leaks due to being closer to other probes in the cell. $\mu\mu\mu_1$ has a lower intrinsic width than the $M\mu$ which means it is a more effective thermometer at $T \leq 100 \mu\text{K}$. Both of these wires have a leg spacing of 3 mm and are placed to the side of the BBR. The wire $\mu\mu\mu_3$ can be used as a thermometer in order to verify the $M\mu$, but is also less reliable due to its proximity to other probes in the cell. The main purpose of this wire in the experiment is to create a quasiparticle beam that has a profile that can be imaged by the tuning forks. This wire is commonly known as the 'source' wire. This wire has a leg spacing of 3.2 mm and is placed 1 mm away from both the tuning forks and the front of the BBR.

3.1.1 BBR Description

Our BBR consists of two wires $\mu\mu\mu_2$ and μ_2 that use the same concepts explained in section 3.2.1. Both of the wires in the BBR have a leg spacing of 3 mm and are placed inside a box that consists of stycast impregnated paper which has dimensions of 5.5 by 5.5 by 5.5 mm. A hole has been drilled into the BBR with a diameter of approximately 0.3 mm and hole depth of 0.4 mm.

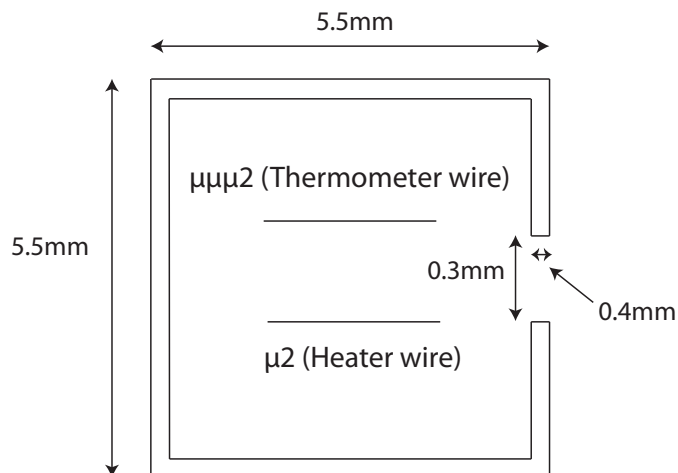


FIGURE 3.2: A 2D diagram of the box and its dimensions (Not to Scale). The height of the box is 5.5 mm and is not shown in the diagram.

The BBR is used to create a quasiparticle beam which is generated by driving the generator wire (μ_2) to a high power with the power being given by $\dot{Q} = Fv$ in which the profile of the beam is supposed to be focused on the centre of the quasiparticle camera. When the generator wire is being driven hard the damping on the thermometer wire ($\mu\mu\mu_2$) can be used to deduce the temperature inside the BBR. The principles behind the BBR operation are discussed in section 2.11.

3.1.2 The Quasiparticle Camera

A set of measurements in this thesis evaluate the suitability of the quasiparticle camera in order to find the beam profile from the source wire ($\mu\mu\mu_3$) and the BBR. In order to explain these measurements it is best to explain how the quasiparticle camera was designed. The quasiparticle camera consists of a copper block with dimensions of $5.7 \times 5.7 \times 4.0$ mm in which 25 holes with a diameter of 1.0 mm were drilled with the intent that a tuning fork would sit into each individual hole. This is shown in figure 3.3 [46].

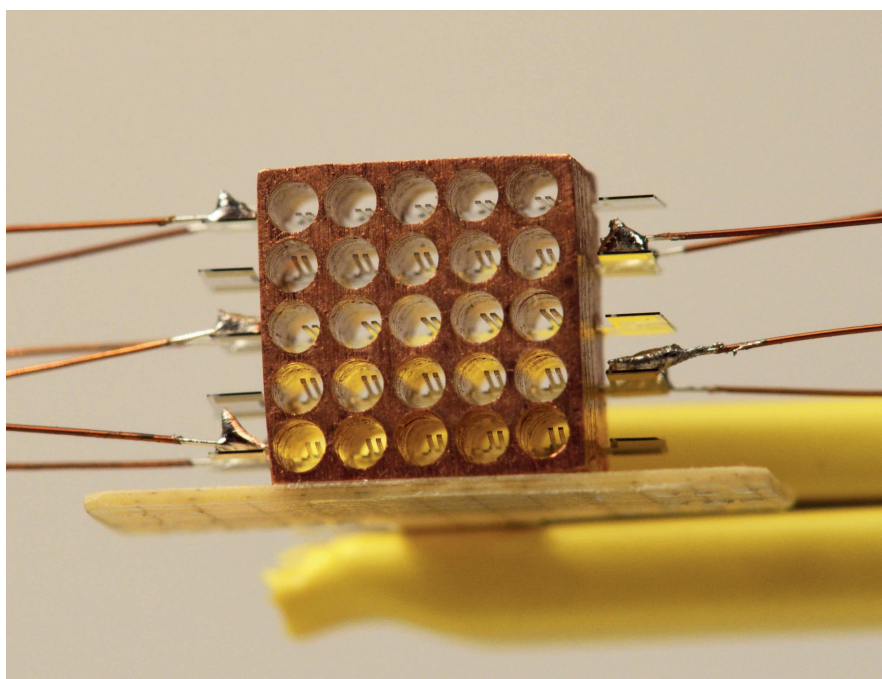


FIGURE 3.3: A picture of the quasiparticle camera before it was added to the cell.

As shown in figure 3.3 every 5 of these tuning forks are connected electrically in an array. The camera consists of 5 of these arrays that are similar to that shown in figure 3.4 [46]. The arrays in the camera are named in order from A to E, and then the forks on the array are then given a number dependent upon their frequency i.e where A1 has the

lowest frequency in A Array and A5 has the highest frequency. The arrays were chosen so that the minimum difference in frequency between 2 forks on the same array in this experiment is approximately 2 kHz. As the line width of the forks is ~ 0.05 Hz at low temperatures this means that the resonances of the forks are very unlikely to overlap.



FIGURE 3.4: A typical array of tuning forks that would be placed in the quasiparticle camera.

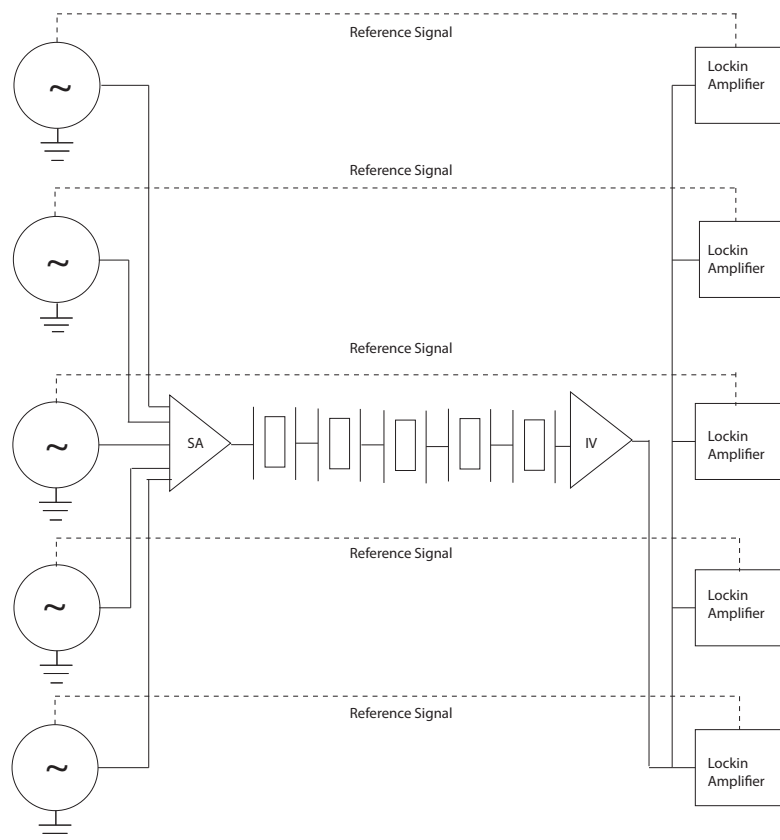


FIGURE 3.5: The setup for one of the arrays in the quasiparticle camera where five signals go through an array of 5 forks reaching a set of 5 Lockin Amplifiers. Note that SA is the summing amplifier with active attenuation and the IV is a current to voltage converter created by Holt et al. [48].

The measurement setup of the quasiparticle camera is shown in figure 3.5. In this setup the signals of 5 Agilent generators [49] are used to create a response from the forks. In this setup A,B,C, and D arrays all used Agilent model 33521A generators and E array used Agilent model 33220A generators. The signals from these generators are used to drive the forks at their resonant frequencies which are at a minimum of 2 kHz away from one another in order to prevent the resonances from overlapping. These signals are then combined and attenuated using a summing amplifier and then sent to the tuning forks where they create a response. The signal from the fork is then amplified using one I-V converter [48] with a gain of 10^6 V/A and then sent to the SR830s in order to measure the response [50].

3.1.3 Properties of the MEMS

Through a collaboration between Lancaster University and the Centre National de la Recherche Scientifique (CNRS) a Micro Electrical Mechanical System (MEMS) was created (at CNRS) and placed in our Lancaster cell. The MEMS has a goalpost shaped structure with legs that are 1 mm away from one another and is made of polycrystalline silicon with a thin layer of aluminium at the surface [51] [52]. The MEMS is placed away from the BBR in order to make sure that this probe is in thermal equilibrium. Recent measurements that were taken of the MEMS can be found in [53]. These show γ and λ measurements for the wire as well as determining the line-shape of the MEMS resonance at different velocities and finding the critical velocity.

3.2 Operating Principle of Vibrating Resonators

In this section we discuss the principles behind operating the various probes in the cell. This includes information such as how the probes were driven and how the response of the probe was obtained and analysed. These probes were chosen because of their high quality (q) factor [54]. This factor is defined as

$$q = \frac{f_0}{\Delta f_2}. \quad (3.1)$$

In this equation q is the quality factor, f_0 is the resonant frequency, and Δf_2 is the Full Width at Half Maximum (FWHM) of the Lorentzian resonance. The q-factor for most of the probes in the cell after demagnetisation is greater than 10^3 which means that these probes are ideal for low temperature measurements.

3.2.1 Vibrating Wires

In our vibrating wire setup the wire is driven by a generator using an alternating current which is then attenuated by a drive box which has a set of resistors and a transformer as shown in figure 3.6. The current through the wire generates a Lorentz force. As the wire is superconducting the main response of the wire to this force is to create a Faraday Voltage. The Faraday voltage V_F and the Lorentz force F_L are related to the velocity and drive of the wire by the following relations.

$$v_W = \frac{V_F}{BL}. \quad (3.2)$$

$$F_L = BIL. \quad (3.3)$$

Where B is the magnetic field strength, I is the current going through the wire, and L is the distance between the legs of the wire. The Faraday Voltage is then amplified by a low temperature transformer. The amplified signal is measured using a Stanford Research 830 (SR830) lockin [50] which is synchronised to the generator. The data is then recorded on the computer using either a General Purpose Interface Bus (GPIB) [55] or a Data Acquisition (DAQ) [56] card.

All the wires in the cell have a Lorentzian curve when they are driven at low forces near their resonant frequencies. From the Lorentzian curve the temperature and the width parameter of the wire can be found. This is shown in section 2.6.1.

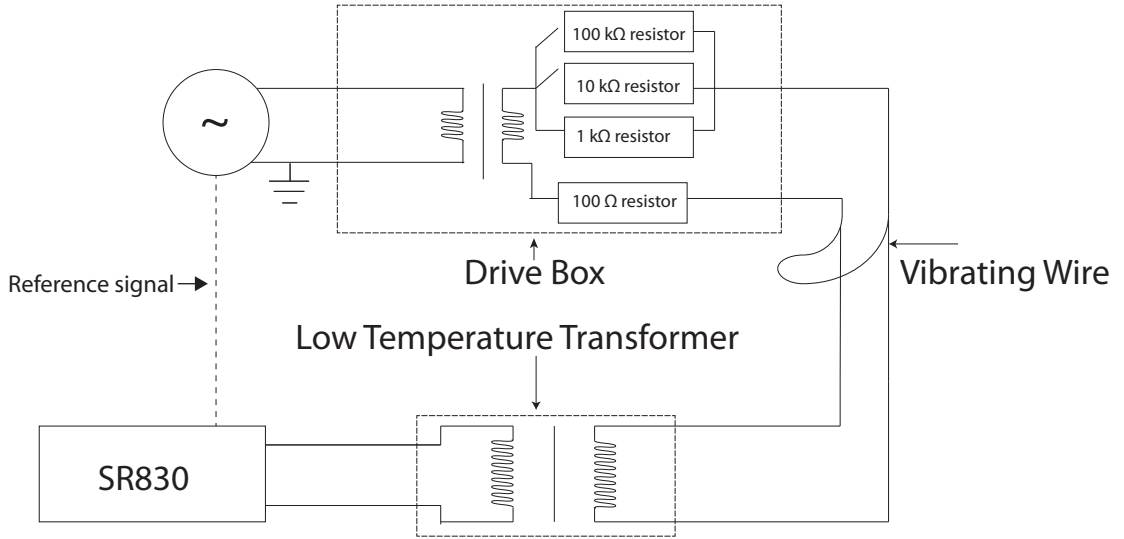


FIGURE 3.6: Setup of a vibrating wire. The signal is created by a generator and then goes through a drive box to the wire which generates a faraday voltage. This signal is amplified by a low temperature transformer and then read by an SR830.

3.2.2 Tuning Forks

3.2.2.1 Properties That can be Calculated From the Tuning Fork Response

The tuning forks used in this cell were manufactured by Statek Corporation [57] and were designed to have a width W of $50\ \mu\text{m}$, and a thickness of each prong T of $90\ \mu\text{m}$. Each tuning fork in the 25 pixel detector had a unique length L of the order of millimetres. A width of $50\ \mu\text{m}$ was chosen as it gives a high sensitivity to quasiparticle damping, which is useful for any type of beam profile measurement. The lengths of the forks have a range between 1.400 and 1.875 mm and each fork is custom made meaning they each have a specific length. This gives each tuning fork a specific frequency as given by

$$f_0 = \frac{1}{2\pi} \sqrt{\frac{k}{m_{eff}}}, \quad (3.4)$$

$$m_{eff} = C_0 \rho_q L T W. \quad (3.5)$$

Combining these two equations gives us

$$f_0 = \frac{1}{\pi} \sqrt{\frac{k}{\rho_q L T W}}, \quad (3.6)$$

where equation 3.5 shows the effective mass of the prong m_{eff} as it is derived by Blaauwgeers et al. [54]. In these equations ρ_q is the density of quartz, k is the spring constant of the material, and C_O is a constant which is determined to be 0.2427 in the cantilever beam model given by Karrai [58] and 0.25 by Bradley et al. (2012) [59], where the value of C from Bradley et al. was used to calculate the effective mass in this thesis. This was done as a safeguard to make sure that none of the forks received pickup from any of the other forks in the cell.

Other parameters that are useful to calculate for the tuning fork are its velocity and force which are given by

$$v = \frac{I}{a}, \quad (3.7)$$

$$F = aV/2, \quad (3.8)$$

where I is the current generated by the fork, V is the drive acting on the fork and a is the fork constant which is defined as

$$a = \sqrt{4\pi m_{eff} HWD}. \quad (3.9)$$

The fork constant is dependent on the effective mass and the HWD of the fork with the HWD being defined in equation 2.20 and the effective mass m_{eff} being defined previously in equation 3.5. From calculating the velocity and force of a tuning fork we can figure out when the fork begins to break pairs in the superfluid. The displacement of the fork can be calculated from the velocity as shown in [60].

$$d = \frac{v}{2\pi f}. \quad (3.10)$$

This calculation is useful as it determines whether the displacement of fork prongs is close to the inter-prong distance (90 μm). If this displacement is determined to be close to the inter-prong distance then the force acting on the fork can be decreased. This in turn stops the fork from breaking.

3.2.2.2 Tuning Fork Harmonics

The first harmonic of a tuning fork is used in this experiment in order to calibrate one of the tuning forks in the cell as a bolometer. Therefore it is useful to study some of the properties of the harmonics of these devices. The paper of S.S.Chaung [61] shows some of the properties of tuning forks including the properties of their harmonics. In order to explain the harmonics of these tuning forks and their frequencies from a theoretical perspective we must first look at Euler-Bernoulli thin beam theory. This theory assumes that the thickness and width of the beam is minimal compared to the length of the beam (*i.e.* $(W, T) \ll L$). Using this premise the equation of motion for the prong can be deduced as shown by Bradley et al. [59].

$$\mu \frac{\delta^2 u(x, t)}{\delta t^2} + \frac{\delta^2}{\delta x^2} \left(E_q I \frac{\delta^2 u(x, t)}{\delta x^2} \right) = q(x, t). \quad (3.11)$$

In this equation $u(x, t)$ explains the displacement of the prong at position x along it. The area moment of inertia I is defined as $WT^3/12$, E is the Young's modulus of quartz and $q(x, t)$ is the distributed load as force per unit length. μ defines the mass per unit length of the prong which is

$$\mu = C_O \rho_q WT, \quad (3.12)$$

where ρ_q is the density of quartz which is 2659 kg/m^3 . Assuming that the prong has one fixed end and one free end then equation 3.11 gives rise to four boundary conditions for the prong.

$$u(x, t)|_{x=0} = 0 \quad \frac{du(x, t)}{dx}|_{x=0} = 0, \quad (3.13)$$

$$\frac{d^2 u(x, t)}{dx^2}|_{x=L} = 0 \quad \frac{d^3 u(x, t)}{dx^3}|_{x=L} = 0. \quad (3.14)$$

In which $\frac{du(x, t)}{dx}$ is the bending of a point on the the cantilever beam, $\frac{d^2 u(x, t)}{dx^2}$ is related to the bending moment at that point $\frac{d^3 u(x, t)}{dx^3}|_{x=L} = 0$ is related to the shear force on

that point on the beam Using the equation of motion for the prong and putting in the boundary conditions the resonant frequencies of the prongs are given by

$$\omega_n = 2\pi f_n = \sqrt{\frac{EI}{\mu}} \frac{\beta_n^2}{L^2}, \quad (3.15)$$

which is shown in [62]. The variable β_n is known to satisfy the equation

$$\cos(\beta_n) \cosh(\beta_n) + 1 = 0, \quad (3.16)$$

where β_n is related to the length of the prong using the following expression,

$$\beta_n = b_n L. \quad (3.17)$$

These give solutions for the values of β_n , found by K.Karrai [62]. The ratio of the frequencies of any two resonances on the fork are given by this equation which is derived from equation 3.15

$$\frac{f_{n+1}}{f_n} = \frac{\beta_{n+1}^2}{\beta_n^2}. \quad (3.18)$$

The values of $\frac{\beta_n^2}{\beta_1^2}$ as well as the value of β_n are shown in table 3.1. Using this table as a reference we can deduce that the First Harmonic has a predicted frequency of 6.27 times the fundamental frequency. In the thesis of Edward Guise [47] the ratio of the first overtone and fundamental frequency was plotted against the ratio of the prongs length to its width. Figure 3.7 gives a experimental comparison to the theoretical predictions discussed above. It shows that at higher width to fork ratios that the thin beam model does not work perfectly. This causes a deviation in the ratio of f_2/f_1 . However we have shown that the Euler Bernoulli thin beam theory can still be used to give a ballpark figure of the frequency of the harmonics of a fork.

TABLE 3.1: The relation between β values for various harmonics [61].

Mode	β_n	$\frac{\beta_n^2}{\beta_1^2}$
Fundamental	1.875	1
First Harmonic	4.694	6.27
Second Harmonic	7.854	17.54
Third Harmonic	10.995	34.38

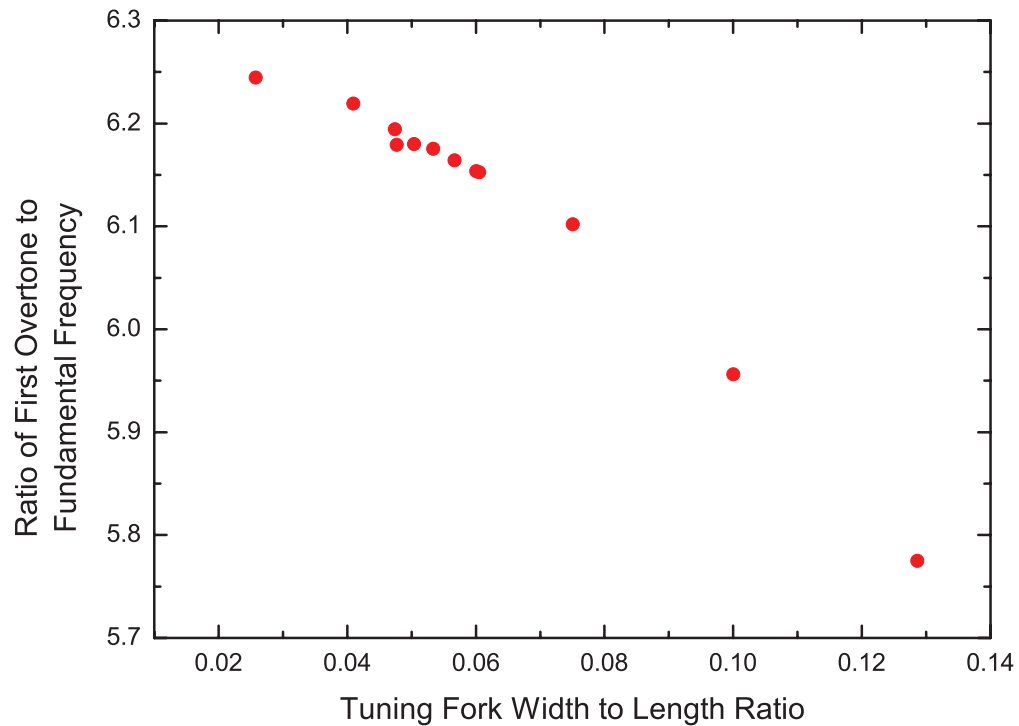


FIGURE 3.7: The frequency ratio between the fundamental and first overtone modes as measured for a number of forks of similar width but varying lengths [47].

3.2.2.3 Tuning Fork Setup

The setup for the tuning forks is quite similar to that shown for the wires. A tuning fork is a piezoelectric detector meaning that if the fork undergoes any type of stress then it will respond by generating a current.

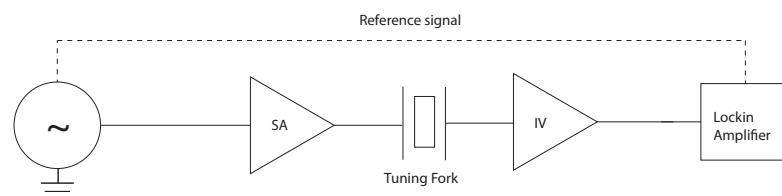


FIGURE 3.8: The setup of a single tuning fork

In our tuning fork setup an Agilent generator [49] is connected to a summing amplifier which will be at a set attenuation. The signals from the generator are then sent into the cell where they will generate a response from the tuning forks in the array. The response then goes out of the fridge to an I-V converter with a gain of 1 million V/A . This I-V converter was created by Steve Holt [48]. The signals from the forks are then read by a series of SR830 lockins [50] which are synched to the generators in order to make sure they are reading the correct frequency. The lockins are measured through a Data Acquisition card or the GPIB depending on the specific measurement that is being taken. As the ethernet switch has been proven to cause warming in the cell when it is on then for delicate measurements the generators are connected to the GPIB. This is normally the case for overtone measurements especially the ones explained later in section 4.2.3. Otherwise they are connected through an ethernet switch to the computer.

In order to measure the overtones of the forks a high frequency lockin had to be used. The piece of equipment used for these measurements was a stanford research 844 lockin (SR844) which operates between 25 kHz and 200 MHz. The setup for our high frequency measurements is similar to figure 3.8 except a SR830 lockin has been switched out for an SR844.

3.3 Measurement Techniques

In order to record data consistently many different computer programs were used. These programs had different uses with some programs being used for quick measurements and others being used to find the response of a probe to a frequency or driving force shift. These programs are described in this section.

3.3.1 Tracking Width

In some of the measurements taken in this thesis there have been changes to the cell that have taken place over a time period less than one second. In order to measure these changes in the cell the resonance of the probe was tracked on its resonant frequency with the in phase signal being kept at a constant value. By knowing the drive, signal, and backgrounds of the probe we can calculate the force and velocity of the probe and then

use the HWD given by equation 2.20 to find the width of the resonance. A program can do this calculation in real time and then display the width as it is shown in figure 3.9.

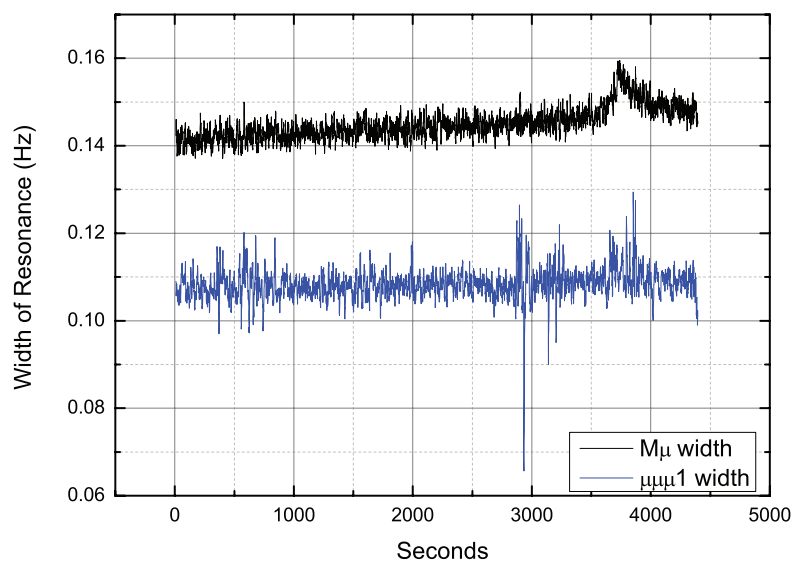


FIGURE 3.9: Using the DAQ program to track the width of two thermometers in the cell.

The tracking width program has been used for the beam profile measurements for the BBR and the source wire, as there are quick changes to the temperature of the cell during these measurements. This program has also been used to track the temperature of the cell overnight in order to check if there was any instantaneous heating in the cell during this period.

3.3.2 Frequency Sweeps

In a frequency sweep (f-sweep) the amplitude of the drive is set at a fixed value while the frequency of the signal changes in increments in order to find the characteristics of the resonance.

The frequency sweep in figure 3.10 shows an in phase and quadrature signal. These signals are normally phase shifted until the Lorentzian of the in phase signal is found. Another issue that had to be taken into account was ringing. In order to remove this issue the time taken per point had to be greater than the response time of the resonator i.e $T_i \geq \frac{1}{\Delta f_2}$. Once the frequency sweep has been corrected for ringing then this measurement can be used to determine the frequency, phase, HWD, and various other characteristics of the resonance curves. These values are necessary for the function of the other techniques.

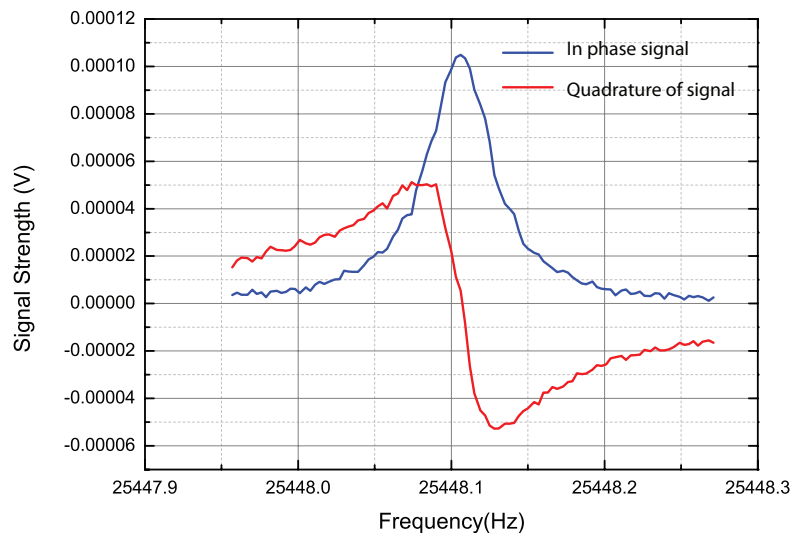


FIGURE 3.10: A frequency sweep of the fork D2 shortly after the cell had been demagnetized

3.3.3 Amplitude Sweeps

In an amplitude sweep (I-swp) the drive of the probe is changed and the response of the probe is measured when the probe is on its resonant frequency. In order to find whether the probe is on the correct frequency the program calculates the fraction of the quadrature signal against the in phase signal ($\frac{V_y}{V_x}$). If the fraction of $\frac{V_y}{V_x}$ that is found experimentally is lower than that the value of the fraction set in the program (1%) then the program will take a measurement and then move on to a higher drive. Most amplitude sweeps take hours to complete and therefore it is imperative that there are no heat leaks in the cell when these measurements are being taken.

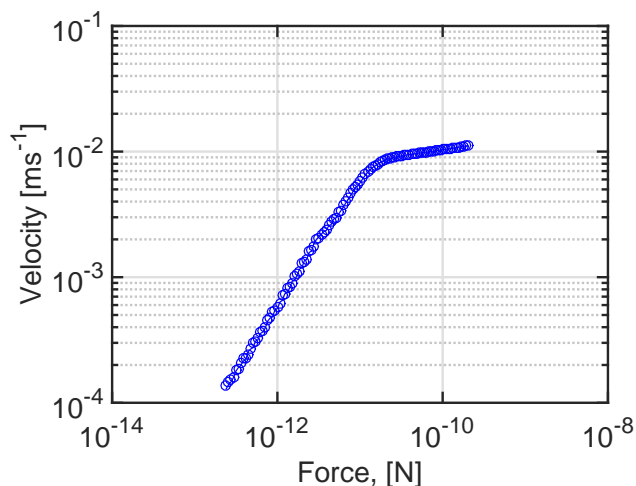


FIGURE 3.11: The Force-Velocity characteristics of A2 found using an amplitude sweep. This is at a temperature of 108 μ K.

Amplitude sweeps are used to find the force-velocity characteristics of a probe including its critical velocity v_c shown in figure 3.11. They can be used to find the off-resonance backgrounds of the probe which are explained in section A.1 and are necessary for all measurements apart from frequency sweeps. In this experiment amplitude sweeps are used in order to find the drive-dependent background of the probes as well as the geometrical constant λ .

3.4 Chapter Summary

This chapter described the probes in the cell and the equipment and the programs that were used in order to analyse these probes. The design of the cell was explained including the BBR, quasiparticle camera, source wire, and various thermometer wires in the cell. The BBR has a heater and a thermometer wire, which are necessary for calibrating it, and the quasiparticle camera is a 25-pixel camera with the data from each pixel coming from a quartz tuning fork. This chapter then discussed the operating principle behind vibrating resonators which explained the room-temperature setup for measuring the vibrating wires and tuning forks, the calculations of force and velocity for vibrating wire resonators and properties of tuning fork harmonics. Finally, the various computer programs that were used to measure the data were discussed as well as their benefits and drawbacks.

Chapter 4

Characterising the probes in the cell

In order to find the quasiparticle beam damping, the properties of various probes in the cell need to be found in order for those probes to be calibrated correctly. The two properties that need to be found for this calibration are γ and λ where γ is related to the sensitivity of a vibrating object to quasiparticles and λ is related to the velocity dependence of the thermal damping. Both of these calibration constants are of the order of unity. The sensitivity of a vibrating object to quasiparticles γ is normally found for Black Body Radiators when they are calibrated whether it is by pulse heating [63] or permanent heating [64] [63]. If the value of γ for one probe is found then γ for another probe can be found given that both probes are in thermal equilibrium. This method has been used by Bradley et al. [65] in order to determine γ for a fork by comparing it to a wire with a known value of γ and Defoort et al. [53] in order to find the value of γ for a MEMS by comparing it to another wire in their cell and assuming that wire had the same value of γ as Bradley et al. [65]. The value of λ for various probes has been found previously for wires [66] [67] [65] and for forks [65] [67] where in all cases λ was determined using an amplitude sweep of the probe. Fisher's paper [66] gives us a value of 0.95 for a wire while Bradley's paper [65] gave 0.69 where both papers used a wire with a 4.5 μm diameter. For a fork, Bradley's paper in 2008 [67] gave a value of 1.28 for a tuning fork which compares to the value of 0.45 for a tuning fork in Bradley's 2009 paper [65] where the tuning fork in Bradley's 2008 paper was much larger than the one in Bradley's 2009 paper.

In this chapter we find out the sensitivity of a vibrating object to quasiparticles for a BBR and for a tuning fork by using its first harmonic as a heater wire. We also compare all other probes in the cell to these aforementioned probes when the cell was at thermal equilibrium in order to estimate γ for these probes. The velocity dependence to thermal damping will also be shown for two wires of different diameter, a tuning fork and the overtone of that tuning fork. This shows whether λ is dependent on geometry and also if it is dependent on the mode of oscillation of the probe.

4.1 Thermal Damping of Various Oscillators

4.1.1 Force-Velocity Characteristics of the Probes

A relatively quick way to find λ is shown in the non-linear corrections in the preliminary measurements section (section A.3). While these measurements give a good indication of the value of λ they are by no means the accurate measurements that can be used to find damping due to the non-linearity of the probe. Instead the most reliable way to find λ is by using an amplitude sweep to find the force-velocity characteristics of the probe as shown in figure 4.1.

The sources of damping that affect the probe are the non-linear damping F_{ex} , the intrinsic damping F_I , and the thermal damping F_T . The non-linear damping only exists when the probe is driven to high enough velocities and the thermal damping is dominant at high temperatures.

$$F_T = F - F_I - F_{ex}. \quad (4.1)$$

This can be simplified again to

$$F_T = F(T, v) - F(0, v). \quad (4.2)$$

This means that the thermal damping F_T can be found if we know the damping force at a certain velocity $F(T, v)$ and subtract from it the intrinsic force at that velocity $F(0, v)$. In order to test a good range of velocities we used the amplitude sweep program. We took

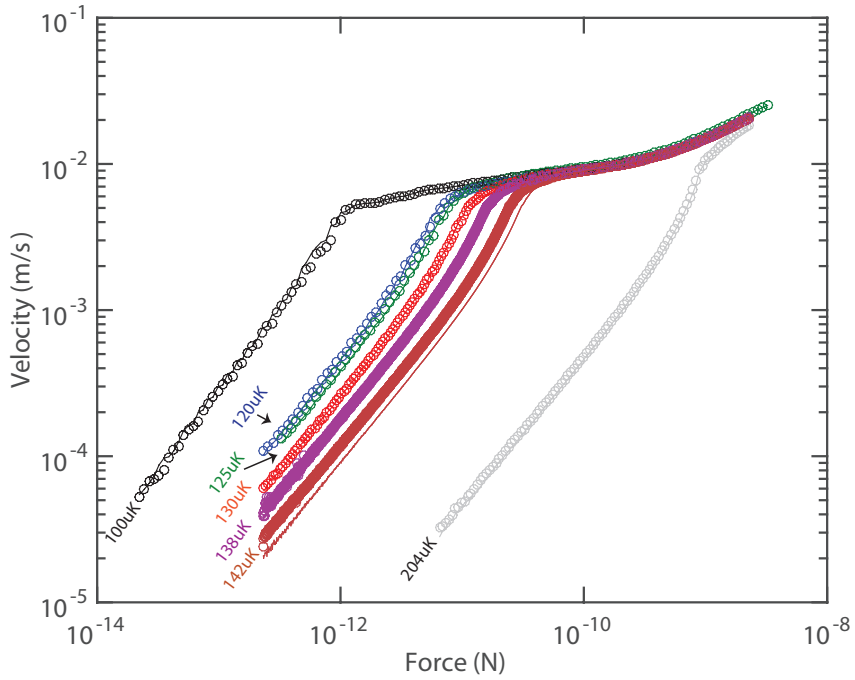


FIGURE 4.1: Amplitude sweeps of $\mu\mu\mu_3$ at different temperatures to find the force-velocity characteristics of the probe where black circles correspond to the intrinsic damping of the probe. The temperature of each characteristic is shown next to it on the graph. The circles indicate the part of the ramp where $\mu\mu\mu_3$ was increased to a certain drive while the lines indicate when the probe was ramped back down to a minimal drive.

measurements of the force-velocity characteristics of each probe at various temperatures. This is shown in figure 4.1 and figure 4.2. In figure 4.1 anything coloured in black is the intrinsic I-swp from the 11th demagnetisation. This was at a temperature of around 100 μK . The rest of the I-swps have been done in either the 3rd or 4th demagnetisation of this run and have temperatures ranging from 120 to 200 μK . The intrinsic I-swps for all of the wires and forks measured are shown in figure 4.3.

In figure 4.3 the velocity is plotted against force for various probes at the temperatures where they have minimal thermal damping. The temperatures of the wires are placed at the bottom of each respective I-swp. The intrinsic I-swp of the overtone of D2 was measured in figure 4.3. This was done at 140 μK in order to make sure that the dominant force on the wire was its intrinsic force and not thermal damping. These I-swps show that pair breaking velocity for the probes is around 7 mm/s which is close to the estimated pair breaking critical velocity of 9 mm/s where the force at which the fork goes pair-breaking is dependent on the thermal damping in the cell. The I-swps in figure 4.3 do

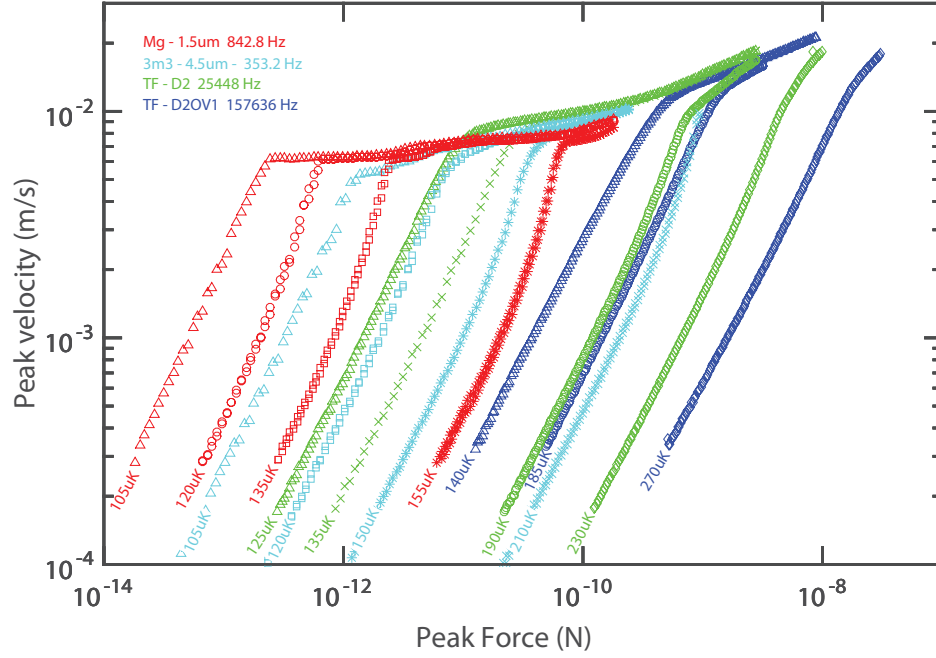


FIGURE 4.2: I-swps taken of $\mu\mu\mu_3$, $M\mu$, D2 and D2OV1 at different temperatures in order to find the force-velocity characteristics of the probes. The temperatures are indicated at the start of the I-swp.

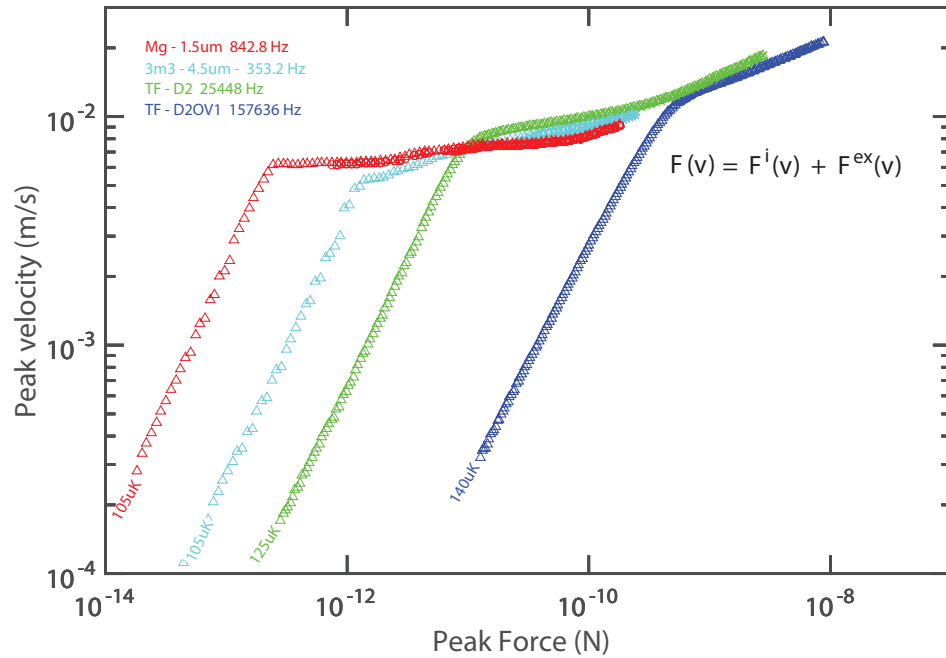


FIGURE 4.3: Intrinsic I-swps taken of various probes in the cell, These show a lack of Andreev reflection as there aren't any excitations in the bulk that the wire could shield itself from.

not show a decrease in the quasiparticle damping of the wire near the pair breaking critical velocity due to Andreev reflection which indicates that they are indeed intrinsic.

4.1.2 The Force Velocity Gradient

The intrinsic damping for the wire is estimated by interpolating between the intrinsic I-swp velocities and the I-swp of the wire at higher temperatures. Through this method the intrinsic damping force and damping from non-linearity are then found and subtracted from the total damping force of the wire at large temperatures. This gives the thermal damping force for any of the I-swps of the wire that have been taken. The thermal damping force is useful as the value of the geometrical constant λ can be found from it. In order to do this, prefactors in equation A.3 need to be removed. To do this we divide the thermal force by its gradient with respect to velocity $\frac{dF_T}{dv}$ where this fraction is given by

$$\frac{dF}{dv} = \frac{-2Ap_F^2 \langle nv_g \rangle \gamma (1 - e^{-\lambda p_F v / (k_B T)})}{k_B T} . \quad (4.3)$$

This value was found for every point on the I-swp and then plotted. This is shown in figure 4.4.

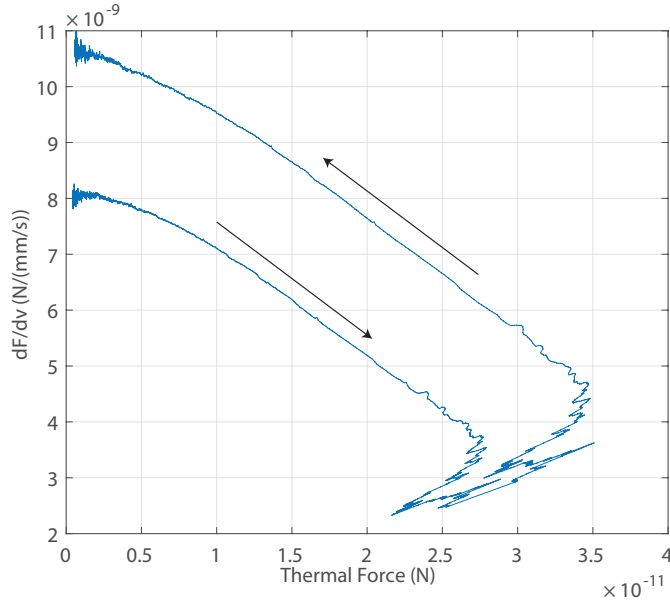


FIGURE 4.4: The change of $\frac{dF}{dv}$ against thermal force in an amplitude sweep taken on $\mu\mu\mu_3$ at 142 μK .

The problem with finding this value of $\frac{dF}{dv}$ is that the I-swp measurement takes hours to complete meaning that the temperature of the cell will increase during this time. This is especially true when the wire is being driven past pair breaking in which case the cell

will be actively warmed by the wire. In order to remove any effects of the temperature change on $\frac{dF}{dv}$ the force velocity gradient is estimated using the HWD of $\mu\mu\mu_3$ and the width of the $M\mu$. This is shown below

$$\left(\frac{dF}{dv}\right)_c = C \frac{(\Delta f_2)_{M\mu}}{RHWD}, \quad (4.4)$$

where $\left(\frac{dF}{dv}\right)_c$ is the force over velocity gradient calculated from the HWD. Note that for the I-swps of the $M\mu$ another probe had to be used as a reliable thermometer. This was done using the width of $\mu\mu\mu_3$ and is shown below

$$\left(\frac{dF}{dv}\right)_c = C \frac{(\Delta f_2)_{\mu\mu\mu_3}}{RHWD}. \quad (4.5)$$

In these calculations the width of the probe is deduced from the width of a thermometer probe in the bulk and the effective width C in which the effective width is a conversion factor from the damping of one probe to another given by $C = \frac{\Delta f_2^{P2}}{\Delta f_2^{P1}}$ where $P2$ is the second probe and $P1$ is the first probe. This conversion factor is explained further in section A.4. From the width of the probe the $\frac{dF}{dv}$ can be found from the $RHWD$ found during the time the wire was on frequency sweep. This is where the 'Real' HWD i.e $RHWD$ is given as

$$RHWD = \frac{v}{F\Delta f_2}, \quad (4.6)$$

where the force and velocity of the wire can be calculated through equation 3.2 and equation 3.3 respectively. Once the calculated fraction $\left(\frac{dF}{dv}\right)_c$ is estimated for all the points on the I-swp it is then added to the $\frac{dF_T}{dv}$ which has been calculated previously in order to get rid of the effect of the change in temperature in the I-swp. The calculated fraction from the start $\left(\frac{dF}{dv}\right)_c$ is then subtracted from the $\frac{dF_T}{dv}$ for all the points on the I-swp. This is all shown in

$$\left(\frac{dF}{dv}\right)_{corr} = \left(\frac{dF}{dv}\right)_c - \left(\frac{dF}{dv}\right)_{c(st)} + \left(\frac{dF}{dv}\right), \quad (4.7)$$

where $(\frac{dF}{dv})_{corr}$ is the corrected $(\frac{dF}{dv})$, $(\frac{dF}{dv})_c$ is the value of $(\frac{dF}{dv})$ calculated from the HWD and $(\frac{dF}{dv})_{c(st)}$ is the value of $(\frac{dF}{dv})$ calculated from the start of the I-swp. Using equation 4.7 the initial shift in the intrinsic $(\frac{dF}{dv})$ can be accounted for as shown in figure 4.5.

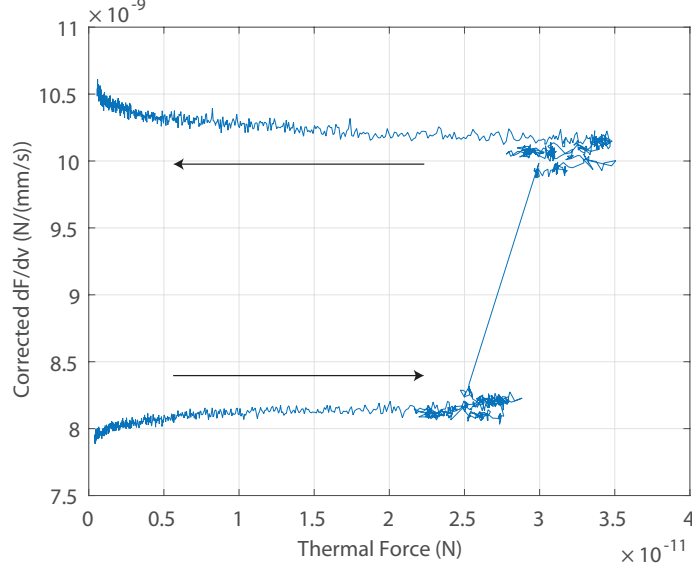


FIGURE 4.5: The change of corrected $DFDV$ against thermal force in 1 I-swp of $\mu\mu\mu_3$ at $142\ \mu\text{K}$.

The value of $\frac{dF}{dv}_{corr}$ plotted in figure 4.5 is the one used in further calculations to find λ . This value is only dependent on the temperature of the cell not the velocity the probe is driven to.

4.1.3 Finding λ From the Amplitude Sweeps

Once the force-velocity gradient has been found then the value of λ can be found. By dividing the thermal force by the gradient of the thermal force with respect to velocity we find that

$$\frac{F_T}{\frac{dF_T}{dv}} = \frac{k_B T (1 - e^{-\frac{\lambda p_F v}{k_B T}})}{\lambda p_F} . \quad (4.8)$$

By rearranging equation 4.8 we get the equation shown below

$$\frac{F_T}{\frac{dF_T}{dv}} \frac{p_F}{k_B T} = \frac{(1 - e^{-\frac{\lambda p_F v}{k_B T}})}{\lambda} . \quad (4.9)$$

The value of $\frac{F_T}{\frac{dF_T}{dv}} \frac{p_F}{k_B T}$ is known as the reduced force. To simplify equation 4.9 we turn everything into a reduced velocity which is the same as explained in the theoretical section (equation 2.57). This is where $\frac{dF_T}{dv_*}$ is defined by equation 4.10 and v_* is called the reduced velocity and explained by equation 4.11.

$$\frac{dF_T}{dv_*} = \frac{dF_T}{dv} \frac{k_B T}{p_F}, \quad (4.10)$$

$$v_* = \frac{p_F v}{k_B T}. \quad (4.11)$$

By plotting the reduced force against reduced velocity given by equation 2.57 against equation 4.11 we can estimate the value of λ . This is done by calculating the reduced force for any given value of the reduced velocity and seeing if the theoretical curve fits the data. This is shown in figure 4.6 where the blue line is the experimental data that was retrieved using the I-swp and the red line symbolises the theoretical fit to the data given by equation 2.57. This I-swp was taken at roughly 142 μK and the temperature change in the cell during this I-swp was about 4 μK .

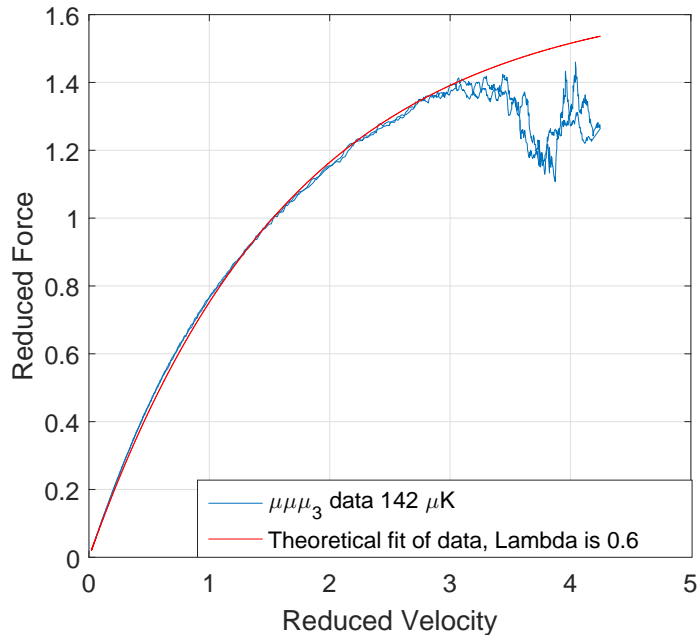


FIGURE 4.6: The plot of reduced force against reduced velocity for the amplitude sweep of $\mu\mu\mu_3$ at 142 μK in order to find λ . The theoretical curve is with λ at 0.6 ± 0.03 . The error in lambda was found by comparing various theoretical curves and seeing which range of curves fit the data well.

This process was then repeated for most of the I-swps shown in figure 4.1 for $\mu\mu\mu_3$. This gives us a value of λ of 0.50 ± 0.10 which is similar to the value of 0.69 calculated by Bradley et al. [65]. This method may not be perfect as it does not average the data, meaning there are odd points at high values of the reduced velocity that were not fitted.

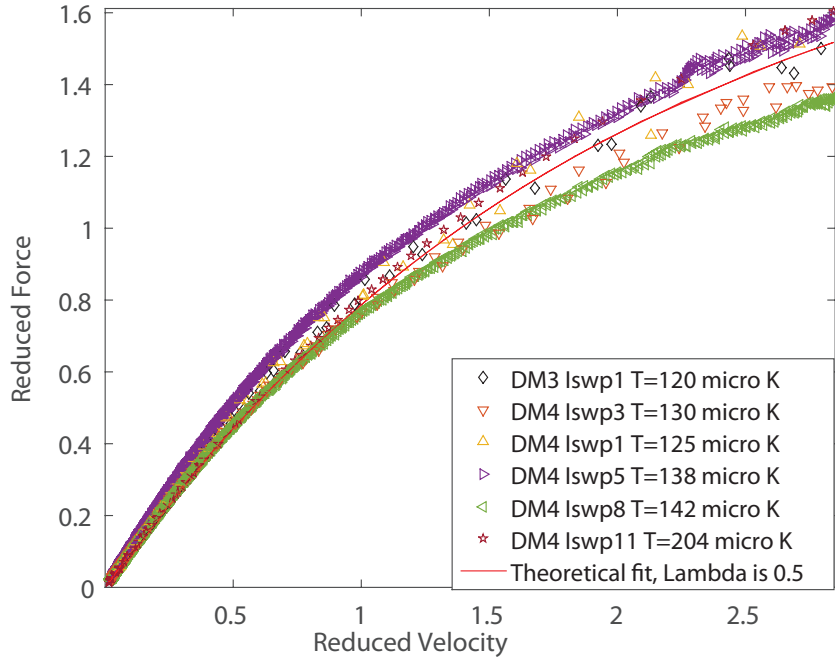


FIGURE 4.7: The plot of reduced force against reduced velocity for all the amplitude sweeps of $\mu\mu\mu_3$ analysed in order to find λ with a theoretical fit of λ is 0.50 ± 0.10 .

This process has been repeated for five amplitude sweeps of D2OV1 at different temperatures. Three of these were at 60 dB attenuation while the other two were at 40 dB. The Reduced Force against Reduced Velocity of each amplitude sweep has been averaged and is plotted below.

The same process has also been done for the $M\mu$ and the fundamental of the fork known as D2. These give values of λ of 0.83 ± 0.07 for the $M\mu$, 0.60 ± 0.10 for $\mu\mu\mu_3$ and 0.3 ± 0.06 and 0.10 ± 0.03 for the fundamental and harmonic of the fork D2 respectively. The differences in the value of λ for the wires may be because of their different wire diameters as postulated in [65].

In figure 4.9 the reduced force and reduced velocity were found for the $M\mu$, $\mu\mu\mu_3$, and the fork D2 using the methods that were explained previously. The symbols used in this graph are the same as those used in figure 4.2 and are from I-swps taken at various temperatures. This graph shows that the data collapse nicely onto a single curve for

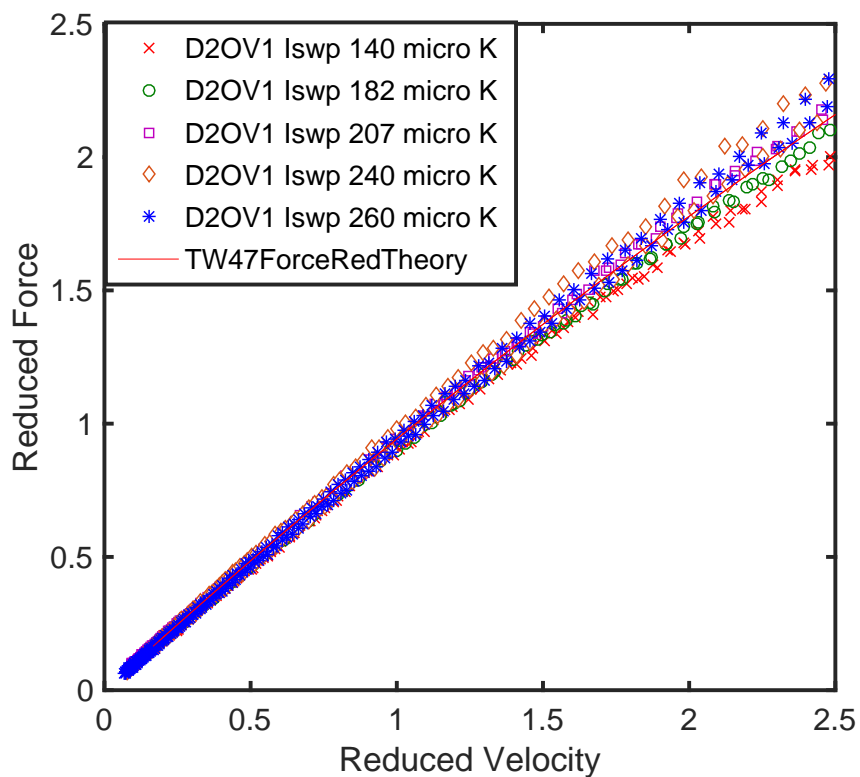


FIGURE 4.8: The plot of reduced force against reduced velocity for all the amplitude sweeps analysed in order to find λ with a theoretical fit of λ of 0.1 ± 0.03 .

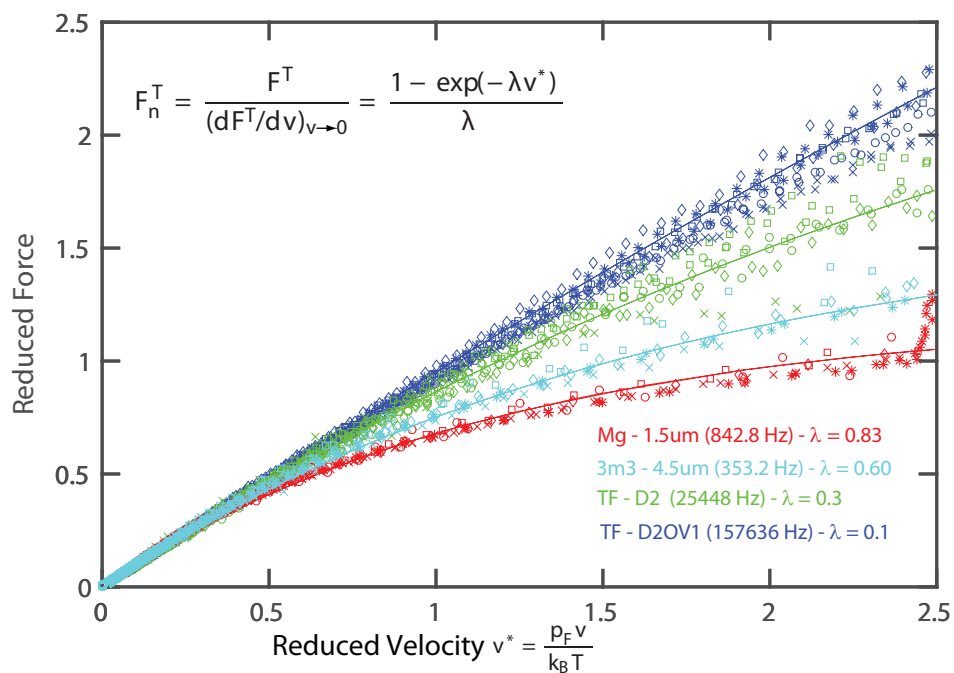


FIGURE 4.9: Calculations of λ for various probes in the cell.

each probe. The lines going through the curve are theoretical fits using equation 2.57 (shown in the graph). The fits show that the mode of oscillation does effect λ as D2

(0.30 ± 0.06) has a higher value of λ than D2OV1 (0.10 ± 0.03). They also indicate that the value of λ is dependent upon the diameter of a wire as the M μ (0.83 ± 0.07) has a slightly higher value of λ than $\mu\mu\mu_3$ (0.60 ± 0.10). Finally, the value of λ for the wires is much higher than that for the forks which indicates that geometry does play a factor in determining the geometrical constant λ .

4.2 Sensitivity of Vibrating Objects to Quasiparticles

4.2.1 Finding γ for $\mu\mu\mu_2$

The derivation for γ for a wire can be found by rearranging equation 2.66 and is given as

$$\gamma = \frac{\Delta f_2 \langle E \rangle T}{\dot{Q}} \times \frac{\pi k_B m_l}{2d p_F^2} A_H. \quad (4.12)$$

The value of the width parameter over power $\frac{\Delta f_2 \langle E \rangle T}{\dot{Q}}$ has been found using the BBR calibration as $3.33 \times 10^{-18} \text{ Hz, J, K/W}$ shown in section 5.1. The mass per unit length of the wire m_l and the area of the hole A_H can be converted into parameters that are better known. This gives the equation

$$\gamma = \frac{\Delta f_2 \langle E \rangle T}{\dot{Q}} \times \frac{\pi k_B \rho d \pi^2 R^2}{8 p_F^2}. \quad (4.13)$$

Where ρ is the density of the probe material which for wires is 6050 kg/m^3 and for the forks is 2660 kg/m^3 and R is the radius of the BBR hole which is 0.15 mm , d is the diameter of the wire, and p_F is the Fermi momentum. From this calibration we get that the value of γ for $\mu\mu\mu_2$ is 0.16 . This is similar to that found in [65] which gives a value of 0.24 for wires.

4.2.2 Using γ for $\mu\mu\mu_2$ to Find γ for Other Wires in the Cell

The equation for finding γ for one wire when another is known has been shown in equation 2.87 and is restated here

$$\gamma^{W2} = \gamma^W \frac{\rho^{W2} \Delta f_2^{W2} d^{W2}}{\rho^W \Delta f_2^W d^W}. \quad (4.14)$$

All these variables except the $\frac{\Delta f_2^{W2}}{\Delta f_2^W}$ are known. This fraction has to be found experimentally using a method shown in section A.4. In this situation the effective width C shown is defined as $C = \frac{\Delta f_2^{W2}}{\Delta f_2^W}$ which for any comparison of γ with $\mu\mu\mu_2$ gives $C = \frac{\Delta f_2^{W2}}{\Delta f_2^{\mu\mu\mu_2}}$. The values of C between each wire were then found and the value of γ calculated from it. These results are then put into a table shown below.

TABLE 4.1: Effective width of the wires compared to $\mu\mu\mu_2$ and the value of γ for all wires except μ_2 , ICTA and OCTA.

Device	$\mu\mu\mu_2$	$\mu\mu\mu_1$	$\mu\mu\mu_3$	$M\mu$	μ_1	MEMS
Effective Width	1	1	0.97	3.14	0.36	0.96
γ	0.159	0.159	0.153	0.167	0.172	0.330
Error in γ	0.004	0.005	0.004	0.005	0.005	0.009

The reason γ for μ_2 could not be measured is because the wire wasn't swept over a large temperature range meaning that the effective width could not be found. The value of γ for ICTA and OCTA weren't measured as they weren't swept at the same temperatures that the other wires were swept at. All of the other wires in the cell apart from the MEMS had approximately the same value of γ . One possible reason that the value of γ is different for the MEMS is because it is made of a different material and is a goalpost shape which is different from the semicircle shape that most of these wires have. The value of γ of the MEMS is by Defoort et al. [53] to be 0.7 which is different than the value of the MEMS of 0.33 found in this thesis. The method used in [53] was to compare the effective width of the MEMS against the $M\mu$ and then calculate γ for the MEMS using γ for the $M\mu$. In their calculation they use a value of γ from a previous paper (0.3 which is from [65]). This is different from the value of γ calculated in this thesis of 0.16.

4.2.3 Finding γ for D2 Using its Overtone Mode

In order to find γ for the forks we have to assume that they are bolometers. This means that local to the fork we have to assume that the helium is in thermal equilibrium. In order to calibrate the bolometer the width parameter of the fork has to be calibrated against its power. In these measurements we use the first overtone of the fork as a heater

and the fundamental mode as a thermometer. The overtone is being measured by a high frequency Stanford Research 844 lockin while the fundamental is being recorded by a Stanford Research 830 lockin.

The fork we chose for these measurements was D2 and this was because of the low intrinsic width of the overtone of the fork. The intrinsic width of the overtone of D2 is 3 Hz compared to other forks which have an intrinsic width closer to 100 Hz. Because of the lower intrinsic damping on the overtone it means the overtone will go pair breaking with a low driving force and is therefore more useful as a heater. A diagram of the dimensions of a fork in a copper block are shown in figure 4.10. Another assumption is that none of the quasiparticles escape through the back hole of the camera. This may not be a good assumption because the distance between the back wall and the camera is 1.5 mm which gives ample space for quasiparticles to disperse in the cell.

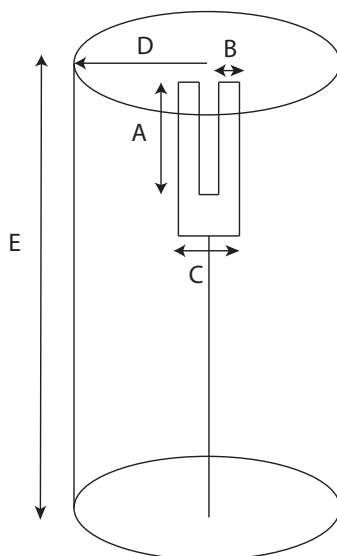


FIGURE 4.10: The hole drilled within the copper block has a depth of 4 mm (E) and a radius of 0.45 mm (D) in which the tuning fork is placed. The tuning fork used for these measurements is called D2, and this fork has a prong length shown by (A) of 1.75 mm as well as a prong thickness of 0.09 mm (B). The fork also has a distance between prongs of 0.09 mm which gives a total thickness of 0.27 mm (C). These forks also have a width of 0.05 mm which is not shown in the diagram.

The fundamental and overtone resonances of the fork D2 were found from a frequency sweep with the overtone at a frequency of about 6.25 times the fundamental mode frequency. From the frequency sweep the HWD and the intrinsics of the fork modes were found and then all the relevant data were put into a DAQ program where the drive of the overtone was then ramped up in steps up to 2.3 V at an attenuation of 40 dB while the fundamental was tracked during this ramp as a thermometer of the pixel

temperature and the thermometer wires $M\mu$, $\mu\mu\mu_3$, $\mu\mu\mu_1$, $\mu\mu\mu_2$ were used to check the bulk temperature. The effect of the increase in drive in the overtone is shown on the fundamental in figure 4.11.

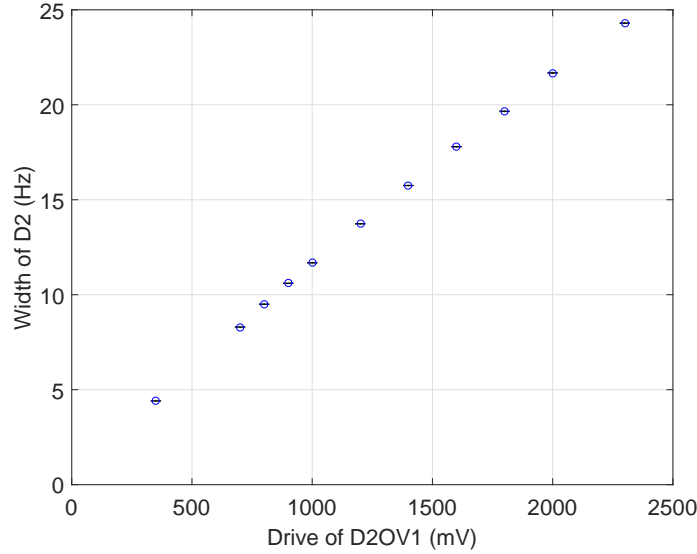


FIGURE 4.11: Effect of the drive of the overtone of D2 on the damping of its fundamental during the measurement.

The measurements shown in this figure were made using are at high drives because a reduction in quasiparticle damping was seen at low drives near the pair breaking critical velocity of the overtone. This is attributed to self shielding and at high drives the effect of the extra quasiparticle damping on the fundamental is considerably higher than the self shielding effect. The highest drive that could be achieved with the overtone was 2.3 V at an attenuation of 40 dB. This is because the overtone went off resonance at higher drives and would not have given any useful data.

From this data the force of the tuning fork was derived using its drive and the velocity was found from the output of the tuning fork V_x . This is shown in equation 3.7 and equation 3.8. Then the power \dot{Q} inside the pixel was found using the velocity and force as ($\dot{Q} = Fv$). Once the power of the overtone in the pixel was found the temperature of the pixel was calculated using equation 2.39 and the width parameter of the fundamental was calculated using equation 2.60. The width parameter of D2 was then plotted against the power of D2OV1. This is shown in figure 4.12.

This plot gives a calibration constant $c = 1.62 \times 10^{-19} \pm 1.61 \times 10^{-20}$ Hz J K/W and an x^2 component of -4.99×10^{-11} Hz J K/W² with the error in the calibration constant

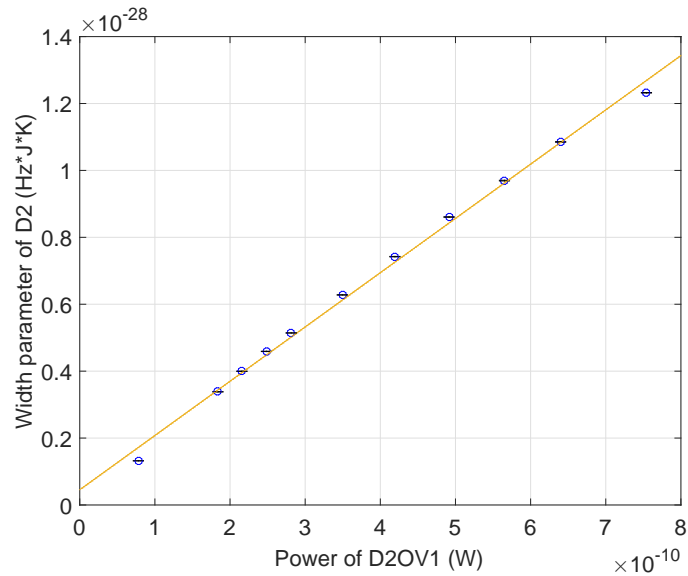


FIGURE 4.12: Effect of the power of D2OV1 on the damping of D2. This is a similar measurement to the BBR calibration.

being calculated by taking the normal of the residuals and dividing it by the mean power in the fit. The plot seems to change gradient halfway through the measurement so therefore it's best to analyse the data at high and low drives as well as take a polynomial of the data in order to see how the calibration constant changes with the fit.

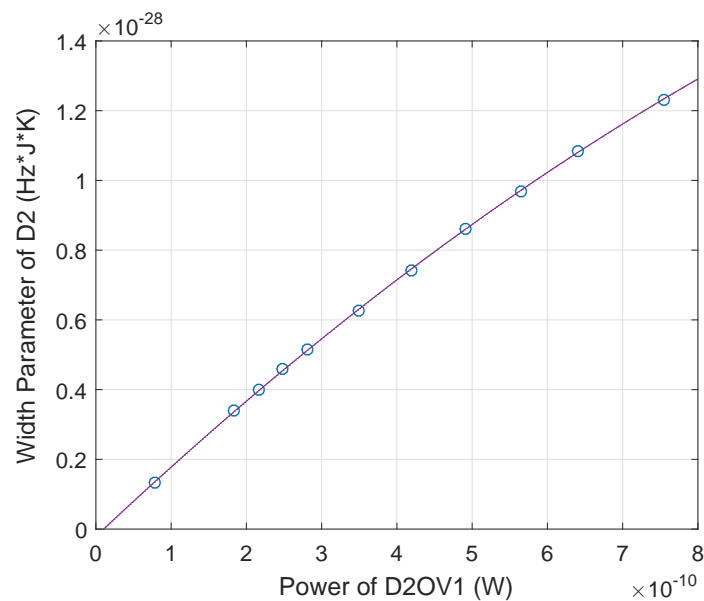


FIGURE 4.13: Polynomial fit of the previous data.

The polynomial fit gives a calibration constant of $c = 2.04 \times 10^{-19} \pm 2.58 \times 10^{-21} \text{ Hz J K/W}$ given by the norm of residuals on the plot. The fits of the data at high drives is given by figure 4.14 and figure 4.15.

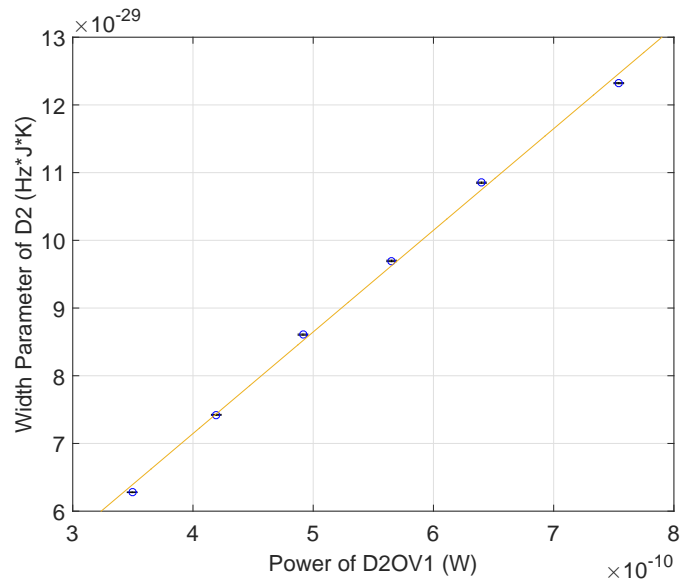


FIGURE 4.14: Effect of the power of D2OV1 on D2 at high drives. This is done as it seems like there was a change in gradient in figure 4.13.

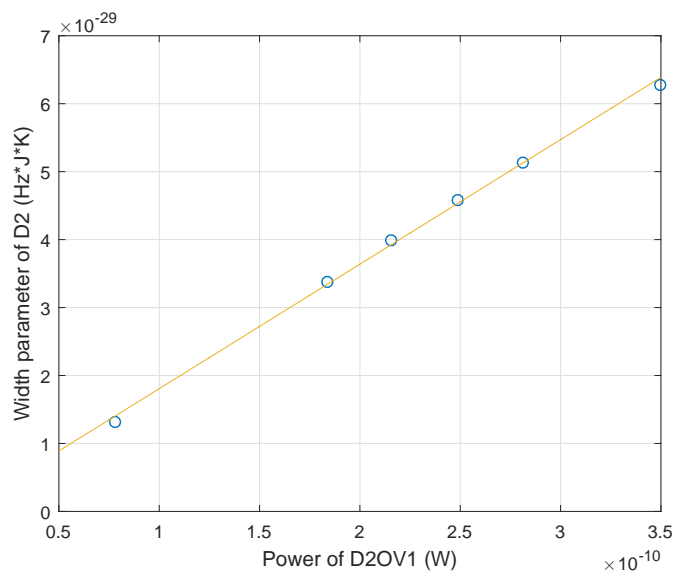


FIGURE 4.15: Effect of the power of D2OV1 on D2 at low drives. This is done as it seems like there was a change in gradient in figure 4.13.

Figure 4.14 gives us a calibration constant $c = 1.50 \times 10^{-19} \pm 4.27 \times 10^{-21} \text{ Hz J K/W}$ while figure 4.15 gives a calibration constant of $c = 1.83 \times 10^{-19} \pm 8.24 \times 10^{-21} \text{ Hz J K/W}$. As all the forks will be driven to relatively low powers in this experiment then the lower calibration will be used in order to determine the value of gamma for the forks as given by equation 4.15.

$$\gamma_F = c \frac{\pi k_B \rho_F t^F \pi R^2}{8 p_F^2}. \quad (4.15)$$

In this equation c is the BBR calibration constant, t^F is the fork thickness, and R is the radius of the front hole of the bolometer. This equation gives a value of γ of 0.18 for D2.

The main reason this equation differs from the work of Bradley et al. [65] is because the effective mass of the prong is calculated to be 4 times less than that in the aforementioned paper. The equation of the effective mass of the prong is explained in equation 3.5. Using the approach given in [65] the value of γ is found to be 0.72. A possible reason behind how this is still different from the value of γ of 0.64 given by [65] is that the fork may have not been driven to a high enough power to get an adequate calibration.

4.2.4 Using the Value of γ From the Pixel Calibration to Find γ for the Rest of the Forks

The comparison between the value of γ for one fork and another can be calculated from equation 2.34 and is given by

$$\gamma_{F2} = \frac{\gamma_F (\Delta f_2)_{F2}}{(\Delta f_2)_F}. \quad (4.16)$$

The assumptions governing this equation are that the cell is in thermal equilibrium and that there was no difference in the thickness between the tuning forks. The first condition can be satisfied when the camera is at a relatively high temperature, and with the second assumption the fork thickness was cut to 90 μm for all the forks in the wafer so there shouldn't be a distinguishable difference between the tuning forks. The data that is used for the comparison between forks are warmups from two separate demagnetisations in which one had B array measured and another had C array measured. The effective width is found between the warmups and can be used in the γ calculations as

$$C = \frac{(\Delta f_2)_P}{(\Delta f_2)_{M\mu}}, \quad (4.17)$$

where C is the effective width. which is determined using the $M\mu$ as that is the most reliable wire in the cell. From this equation 4.18 can be deduced.

$$\frac{C_2}{C_1} = \frac{(\Delta f_2)_{P2}}{(\Delta f_2)_{M\mu}} \frac{((\Delta f_2)_{M\mu})}{(\Delta f_2)_{P1}}. \quad (4.18)$$

The $(\Delta f_2)_{M\mu}$ cancels with itself. If we put this into equation 4.16 we find

$$\gamma_{F2} = \frac{\gamma_F C_2}{C_1}. \quad (4.19)$$

These have $M\mu$ widths measured between 10 and 100 Hz for A,C,D, and E array. For B array the $M\mu$ width is measured between 1 and 10 kHz. These measurements of effective width are explained further in section A.4. The effective widths of the forks are then plugged into equation 4.19 which then generates table 4.2.

TABLE 4.2: Values of γ for all of the forks in camera. This was calculated using the effective width between the fork and D2.

Array	Fork 1	Fork 2	Fork 3	Fork 4	Fork 5
A	0.22	0.22	0.23	0.23	0.23
B	0.22	0.22	0.22	0.22	0.22
C	0.22	0.22	0.22	0.22	0.23
D	0.22	0.22	0.22	0.22	0.22
E	0.27	0.22	0.22	0.22	0.24

In this table all errors for γ are approximately ± 0.01 . It can be seen that most of these values of γ for the forks are similar to one another. This is expected because the geometry of the forks are similar. E1 and E5 are exceptions to the rule and this is due to these forks getting dirt on them or breaking their prongs. This is shown by the high intrinsic width they have. The value of γ is similar for both the forks ~ 0.22 and wires ~ 0.16 in the cell. This may indicate that they oscillate in a similar fashion to one another.

4.3 Chapter Summary

In this chapter, we have found the values of the geometrical constants γ and λ for various probes in the cell. λ was obtained from the force-velocity characteristics of the probe for

two wires, a tuning fork, and its overtone mode where the values of λ found were close to unity. The value of λ for the wires was found to be 0.83 for the $M\mu$ and 0.60 for $\mu\mu\mu_3$ which seem to be values similar to those in Fisher's paper of 0.95 [66] and Bradley's paper of 0.69 [67]. The wires have a larger value of λ than the forks where the forks had a value of 0.3 for D2 and 0.10 for D2OV1 which is probably because of the difference in geometry between the forks and the wires. The value of λ for D2OV1 is 3 times smaller than that of D2 indicating that the mode of oscillation for this tuning fork affects the value of λ . The value of λ for D2 is close to that found by Bradley et al. [65] where the fork in Bradley et al. [65] had a larger width and thickness than this fork which may constitute for the difference in λ between these two experiments.

This chapter then found the value of the sensitivity of the probe to quasiparticles γ . This was done for the thermometer wire in the BBR which was then used to find γ for various other wires in the cell when they were in thermal equilibrium with $\mu\mu\mu_2$. The value of γ for various other wires in the cell was then deduced by comparing the thermal damping on the other wires to the thermal damping of $\mu\mu\mu_2$ where all the wires had a value of 0.16 for γ except for the MEMS which had a value of γ of 0.33. The MEMS was then postulated to have a different value of γ than the other wires as it had a goalpost geometry compared to the semicircle geometry of the rest of the wires. The values of γ for the MEMS was found to be different to that found by Defoort et al. [53] as the value of γ for a wire used in Defoort et al. calculation came from the calibration by pulse heating from Bäulerie et al. (0.28) [63] which is different than the value of γ found for wires in this cell.

Finally, the value of γ was found for a tuning fork using its first overtone mode as a heater and its fundamental mode as a thermometer. This was then compared against other forks to find the value of γ for all tuning forks in the cell. Almost all of the tuning forks in the cell had a value of γ close to 0.22 which is a lot smaller than the value of γ for a tuning fork given by Bradley et al. [65] of 0.62, however this may be due to there being a difference in size between the tuning forks in this experiment and those of Bradley's paper.

Chapter 5

Beam Profile From the BBR and Source Wire

The BBR has been used for bolometric measurements in $^3\text{He-B}$ for more than 20 years. The initial measurements mainly studied the power emitted from the BBR [34, 63] as well as its suitability as a probe to measure the beam profile of a VWR [64], while later works investigated the feasibility of using a BBR as a dark matter detector [68]. After the discovery of quantum turbulence in $^3\text{He-B}$ the BBR became a valuable tool to characterise a turbulent tangle and its decay properties, with the first measurements being of the fraction of quasiparticles that were reflected back into a BBR from a turbulent tangle [43, 69, 70], and following measurements of the decay of turbulence inside a BBR [71]. An overview of these measurements is found in Progress in Low Temperature Physics [72]. This idea was modified so that a BBR could be used to find the amount of quasiparticles that were transmitted through a turbulent tangle, with another BBR creating the quasiparticle flux [73]. Up until this point the BBR has been used to probe the properties of turbulence, but no effort has been made in order to use the BBR to find the spatial distribution of a vortex tangle. The most recent work by Lancaster ULT [46] shows early measurements of the beam profile as well as proof of concept of a tuning fork as a detector of turbulent shielding, where the concept behind this cell is described briefly in the Journal of Low Temperature Physics [74]. This work builds upon the previous paper by giving the beam profile of the BBR as seen by the quasiparticle camera. The results of this chapter can be used in further measurements to find the spatial distribution of quantum turbulence.

In this chapter we present the first measurements of the quasiparticle beam probed using a 2D array of tuning forks and show that a beam of quasiparticles emitted by BBR is uniform and that its profile does not depend on the amount of power emitted.

5.1 Calibration of the BBR

According to the law of conservation of energy, the power deposited in a steady state inside the BBR has to equal the power leaving the box. In the ballistic regime in $^3\text{He-B}$, the power that is deposited inside the BBR and the power that leaves the box are governed by quasiparticle excitations, where the power that leaves the box takes the form of a quasiparticle beam. Thus calibrating the BBR will help us to know the power emitted by the beam of excitations. In order to perform this BBR calibration the thermometer (detector of excitations) and heater (excitation source) wires had to be measured simultaneously. In the superfluid an excitation can be created when velocity of an object or velocity of superfluid around the object reaches so-called Landau critical velocity. The situation in $^3\text{He-B}$ is a bit more subtle [39] where the velocity of the heater wire μ_2 had to be greater than one third of the Landau critical velocity in order to create quasiparticle excitations in the BBR. At zero bar in $^3\text{He-B}$ Landau critical velocity is on the order of 27 mm/s, and wire peak velocity has to be in excess of (9 mm/s).

Figure 5.1 shows the dependence of force F as a function of velocity v for a heater wire. It is clear from this graph that for velocities above 9 mm/s the force required to move the wire is much larger than at lower velocities. The power deposited in BBR by μ_2 was calculated using $\dot{Q} = Fv$ where the force and velocity of μ_2 were calculated using equation 3.2 and equation 3.3, respectively.

The increased number of quasiparticles in the BBR was detected by the rise of the width of the thermometer wire. The thermometer wire was driven at velocities of the order of (1 mm/s), well below the pair-breaking velocity of the wire. This was done in order to make sure that the wire didn't cause any significant extra heating in the box.

The width of the thermometer wire $\mu\mu\mu_2$ as a function of the drive of the heater wire μ_2 is plotted on left part of figure 5.2, whereas the width of the thermometer wire $\mu\mu\mu_2$ is shown as a function of the velocity of the heater wire μ_2 on the right part of figure 5.2. This figure shows that to cause a significant change of the width of thermometer

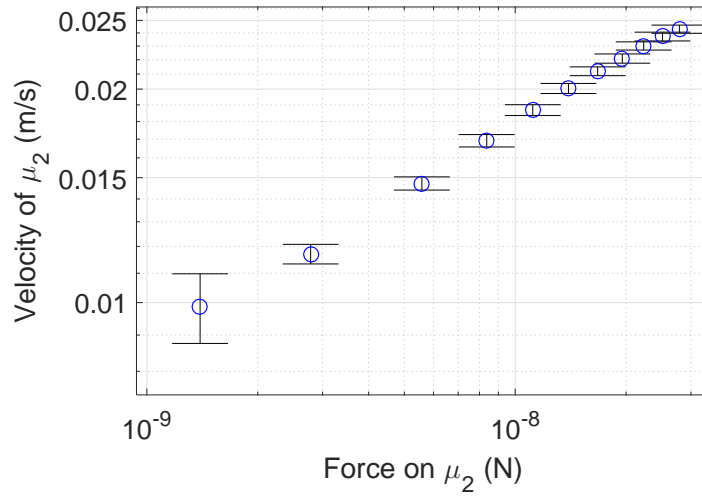


FIGURE 5.1: The velocity against the force of the heater wire μ_2 .

wire during calibration measurements, the velocity of the heater wire μ_2 had to be much higher than the pair-breaking velocity.

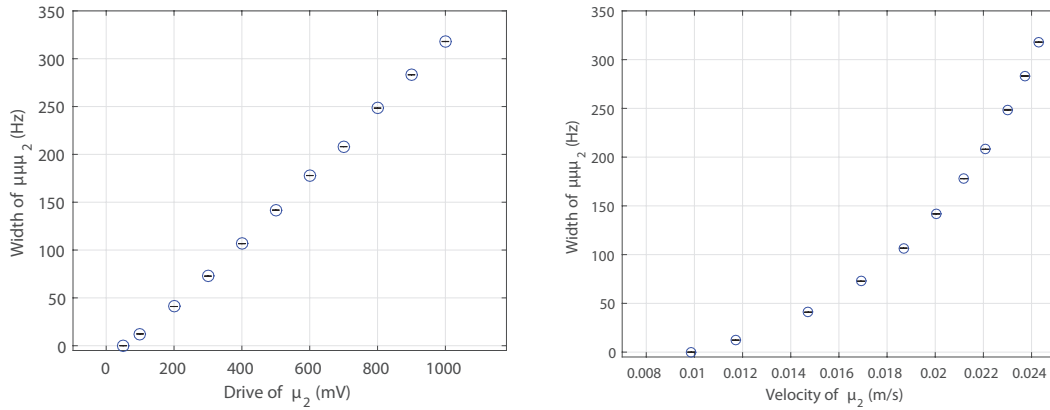


FIGURE 5.2: The width of the thermometer wire $\mu\mu\mu_2$ against the drive (A) and velocity (B) of the heater wire μ_2 .

We have shown in Chapter 2 and equation 2.66 that the power leaving the BBR should be proportional to the Width Parameter $\Delta f_2 \langle E \rangle T$ [63]:

$$\Delta f_2^W \langle E \rangle T^W = c\dot{Q} \quad (5.1)$$

The damping experienced by the thermometer wire $\mu\mu\mu_2$ (Δf_2^W) was converted into a temperature (T^W) using equation 2.39, and then converted to the mean thermal energy of a quasiparticle $\langle E \rangle$ using $\langle E \rangle = k_B(1.76T_c + T)$.

Figure 5.3 shows the resulting BBR calibration in a steady state. Practically this was achieved by averaging the damping of the thermometer wire $\mu\mu\mu_2$ when various powers were reached on the heater wire μ_2 after the BBR had achieved steady state. The calibration constant c given by a linear fit of the data is $3.33 \times 10^{-18} \pm 9.28 \times 10^{-20} \text{ Hz J K/W}$ and was obtained by least square fit of figure 5.3. The calibration of the BBR shown below can be used to obtain a detailed theoretical model of the quasiparticle interaction with the wire and is used in the calculation of gamma in section 4.2.1.

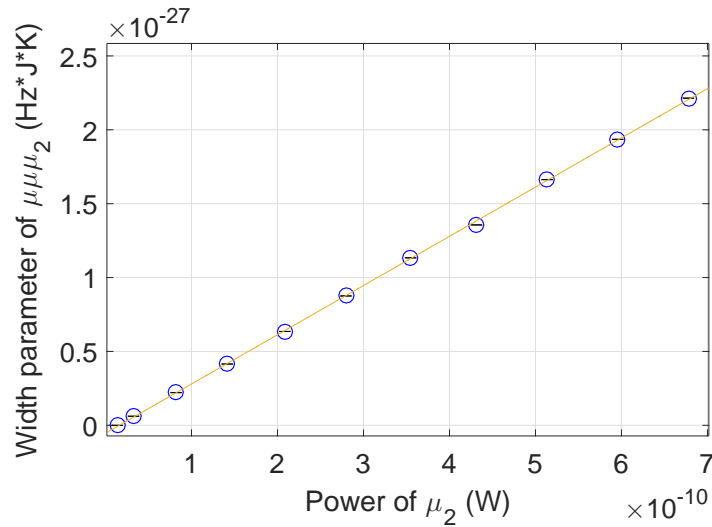


FIGURE 5.3: The calibration of the BBR where μ_2 is the heater wire and $\mu\mu\mu_2$ is the thermometer wire. The straight line is a least squared fit. For details see text.

5.2 BBR Beam Profile Measurements

5.2.1 Calculating the Width Parameter of the Forks due to the BBR

In these beam profile measurements all the forks and wires apart from B Array were monitored simultaneously using the tracking width program shown in section 3.3.1. B Array needed to be measured separately as there was a short between B and C Array that would cause warming in the cell if both arrays were measured simultaneously. During these measurements the forks were being driven to a velocity of 0.1 mm/s in order to ensure a linear response, while the drive on the heater wire μ_2 was ramped up in steps to the setting of 1 V over 1 k Ω in order to check whether the profile of the quasiparticle beam from the BBR changes with respect to power. The width parameter of the forks and the power of the BBR were then found using a the same method as the previous

section and then converted into an effective width for direct comparison between the forks using the method shown in section A.4. This gives the results plotted below.

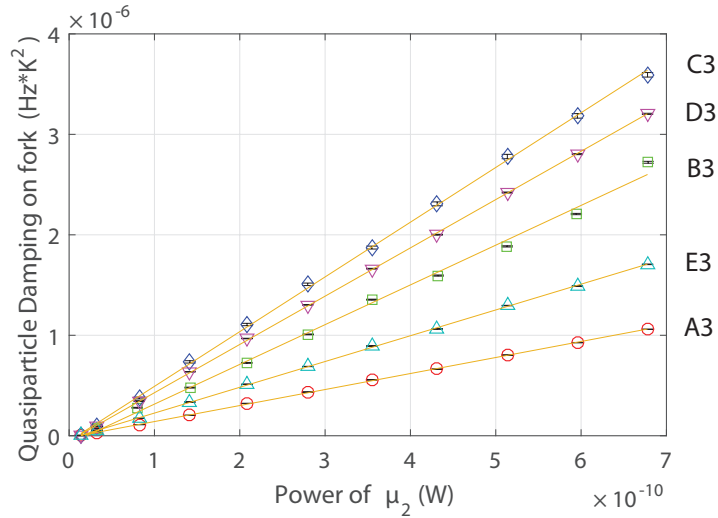


FIGURE 5.4: The change in the width parameter for A3 (Red circles) , B3 (Green squares), C3 (Blue diamonds), D3 (Magenta downwards triangles), and E3 (Cyan upwards triangles) against power during a BBR ramp. Note that by fitting a straight line we show that the beam profile does not change with respect to power.

The power of the BBR shown in this figure is found from the drive and V_x measurements of μ_2 . A linear dependence between the quasiparticle damping and power is shown which indicates the beam profile of the BBR can be found at any power.

5.2.2 The Fork Damping During a BBR Ramp

As there is no change in the beam profile with respect to power then we decided it was best to look at the damping on the forks at the highest power (~ 700 pW) in order to find the beam profile. This is because the highest power gives a higher signal to noise ratio. This beam profile was found using experimental data is shown in figure 5.5, figure 5.6, and a colormap of the profile is shown in figure 5.7.

Figure 5.5 shows that the profile from is centred between C and D (0 mm and -1.1 mm) arrays, because C array has the largest proportion of quasiparticle damping from the beam while D array has a higher proportion of damping than B array. Figure 5.6 shows a similar amount of damping for both the central row and the row at $x = -1.1$ mm which indicates that the beam is focused in between these two rows. Note that for these measurements E1 (The bottom left pixel) was not measuring. This is because E1 has a

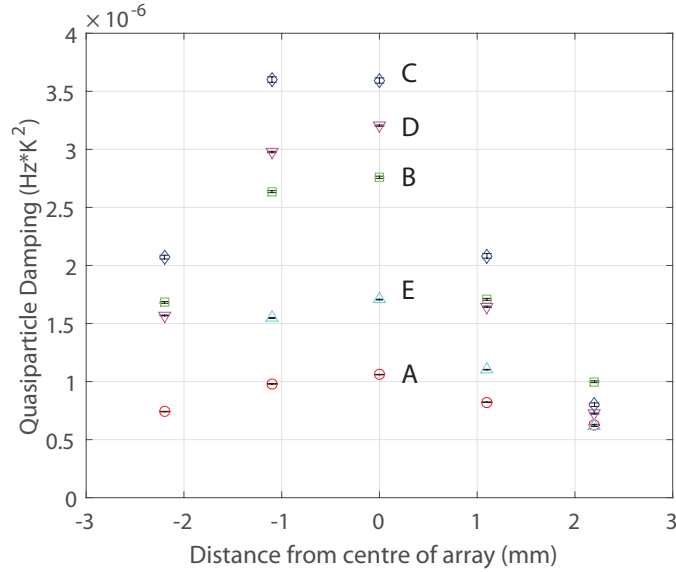


FIGURE 5.5: The beam profile from the BBR as shown on each individual array. In this figure A Array (Red circles), B Array (Green squares), C Array (Blue diamonds), D Array (Magenta downwards triangles), and E Array (Cyan upwards triangles) are shown. This graph shows that the central array (C Array) receives the most damping with the damping falling off for pixels further from the focus of the beam, which seems to be slightly left of the centre of the array.

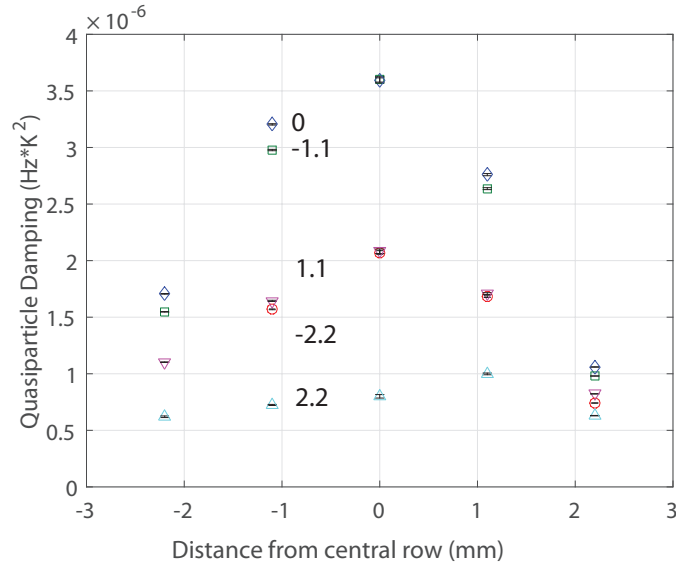


FIGURE 5.6: The beam profile from the BBR as shown on each individual array. In this figure $x = -2.2$ mm is shown as red circles, $x = -1.1$ mm is shown as green squares, $x = 0$ mm is shown as blue diamonds, $x = 1.1$ mm is shown as magenta downwards triangles, and $x = 2.2$ mm is shown as cyan upwards triangles. This graph shows that the focus of the damping is between the second and third pixels and that the beam is shifted slightly towards D array.

very high intrinsic width which is of the order of 3 Hz. This is possibly due to the fork being damaged before being placed in the cell.

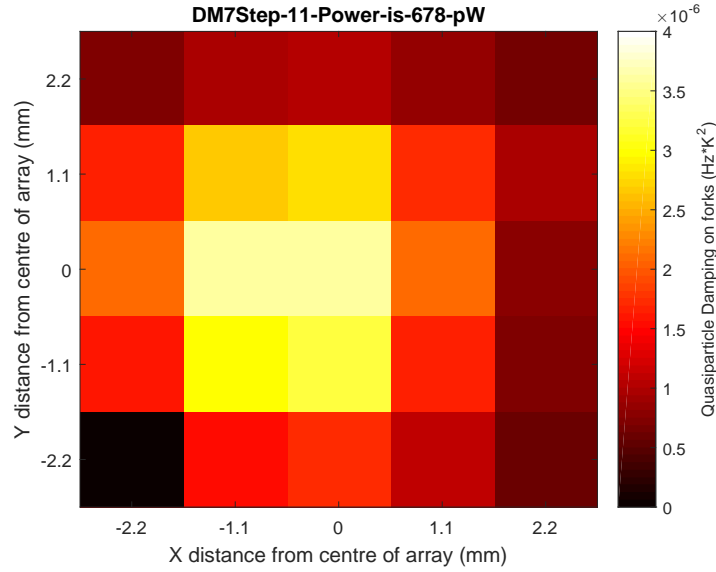


FIGURE 5.7: The beam profile from the BBR at approximately 700 picowatts. The color bar at the side shows what width parameters each color represents.

5.2.3 Theoretical Estimations of the Width Parameter

The theoretical model for the damping on each tuning fork due to the BBR has been explained previously in section 2.11.1. This gave a final result for the damping as shown by equation 5.2.

$$\Delta f_2^F T^F \langle E \rangle = \frac{\gamma^F \rho^W d^W A_H \cos^4(\theta)}{\gamma^W \rho^F t^F} \frac{1}{2R^2} cQ. \quad (5.2)$$

The values of γ used in this equation are the ones that were calculated in the previous chapter which has been shown to be 0.16 for $\mu\mu\mu_2$ and 0.18 for most of the forks. For this estimation of the beam damping the distance between the BBR and the camera (R) was set to be 2 mm and the area of the BBR hole A_H was defined as πR_H^2 with the radius of the hole R_H being 0.15 mm. The beam profile was also estimated to be focused towards the central pixel of the camera. When the theoretical damping is estimated it is then converted into an effective width using the method shown in section A.4. This was done in order to make sure that the experimental damping of the forks could be directly compared to its theoretical counterpart. The comparison between the theoretical damping and the experimental data is shown in figure 5.8 and figure 5.9 with a colour image of the theoretical profile in figure 5.10.

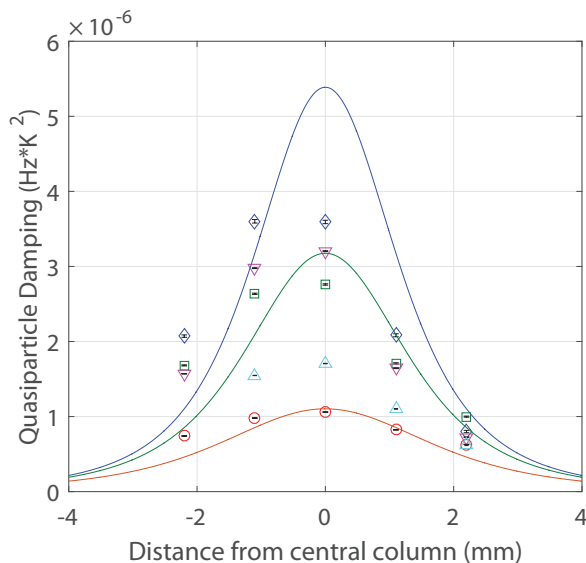


FIGURE 5.8: The experimental data with theoretical fits for each of the arrays. Note due to symmetry only the fits for A (Red), B (Green) and C (Blue) are shown. This means the fit for D is the same as the fit for B, and the fit for E is the same as the fit for A. These fits are largely inconsistent with the data, which means some of the parameters of the fit must be off.

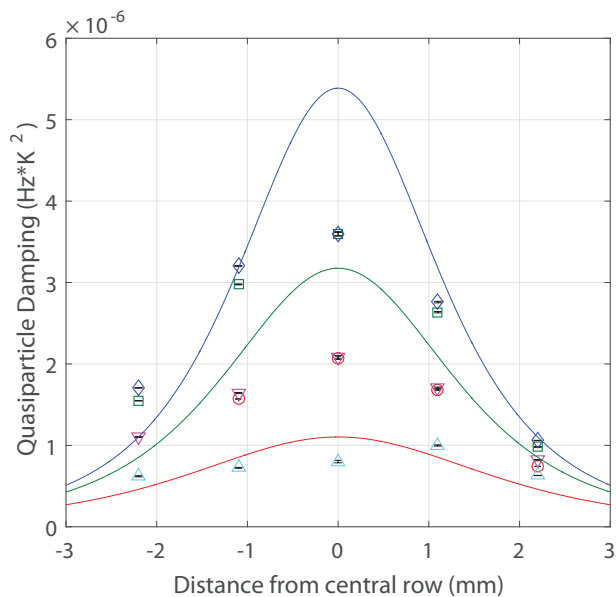


FIGURE 5.9: The experimental data with theoretical fits for each x position on the camera. Note due to symmetry only the fits for $x=-2.2$ mm (Red), $x=-1.1$ mm (Green) and $x=0$ mm (Blue) are shown. The fit for $x=1.1$ mm is exactly the same as the fit for $x=-1.1$ mm and the fit for $x=2.2$ mm is the same as the one for $x=-2.2$ mm. These fits are largely inconsistent with the data, which means some of the parameters of the fit must be off.

These theoretical fits assume that the beam from the BBR was focused on the centre of the camera. This seems to be unlikely given the how the fits compare to the data. The graphs show that the beam is focused between C and D arrays and the second and third

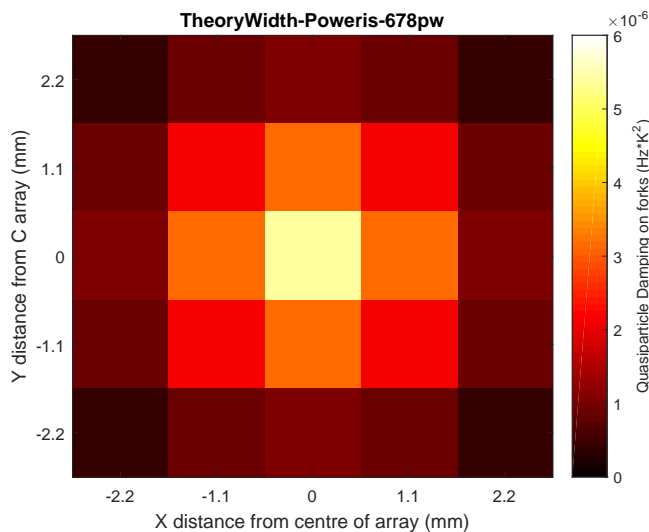


FIGURE 5.10: A colour map of the theoretical beam profile that was used to fit figure 5.8 and figure 5.9.

pixels. The theoretical estimation also seems to give a lower quasiparticle damping than the experimental data.

If the focus of the beam is shifted by -0.55 mm in the x direction and 0.25 mm in the y direction and the quasiparticle damping is multiplied by a calibration constant of 1.15 then the fits seem more reasonable. This is shown in figure 5.11 and figure 5.12 with a colour image of the modified theoretical beam profile in figure 5.13.

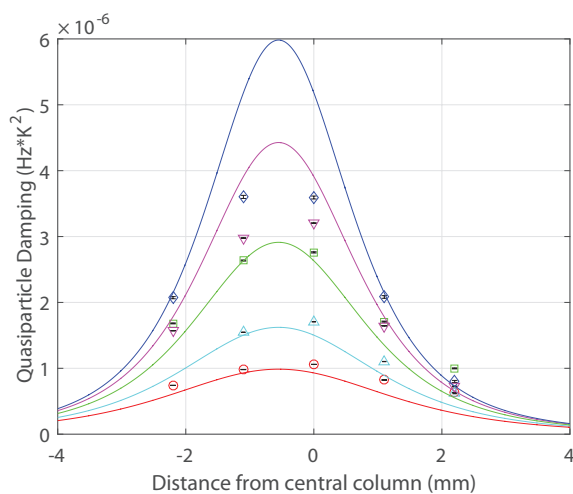


FIGURE 5.11: The experimental data with theoretical fits for each of the array where A is the red line , B is green, C is blue, D is magenta, and E is cyan. In this figure there is extra damping calculated for the central pixels that is not shown on the experimental data. This could be because some of the quasiparticles from the BBR go straight through the pixel instead of interacting with the fork.

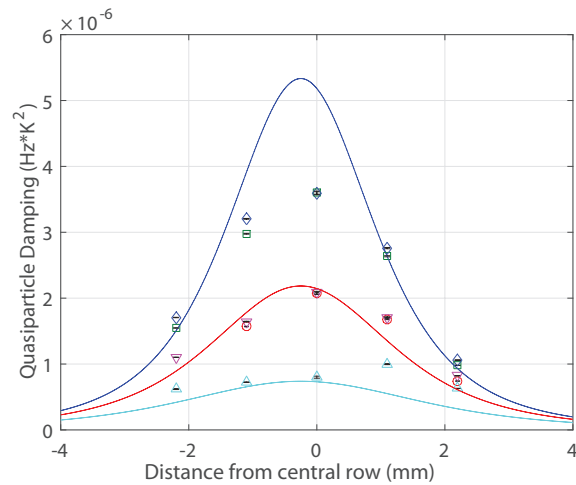


FIGURE 5.12: The experimental data with theoretical fits for each x position on the camera. Note due to symmetry only the fits for $x=-2.2$ mm (Red), $x=-1.1$ mm (Blue) and $x=2.2$ mm (Cyan) are shown. The fit for $x=-1.1$ mm is exactly the same as the fit for $x=0$ mm and the fit for $x=-2.2$ mm is the same as the one for $x=1.1$ mm. In this figure there is extra damping calculated for the central pixels that is not shown on the experimental data. This could be because some of the quasiparticles from the BBR go straight through the pixel instead of interacting with the fork.

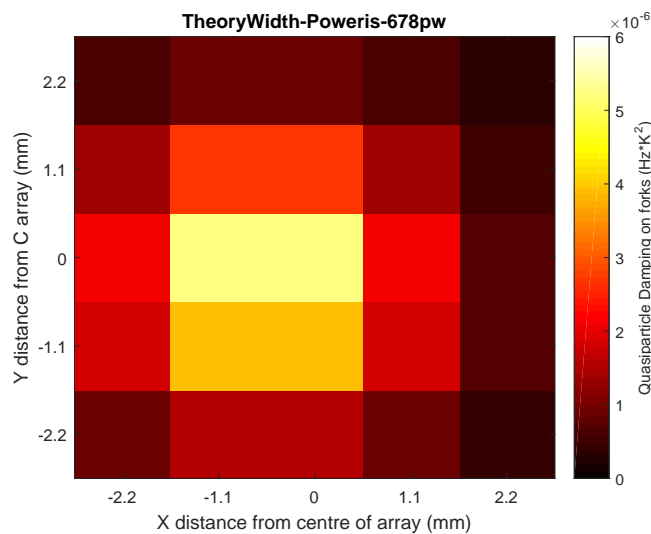


FIGURE 5.13: A colour map of the theoretical beam profile that was used to fit figure 5.11 and figure 5.12.

These graphs show that a greater fit of the experimental beam profile can be achieved with a slight modification to some of the parameters of the BBR. However, both of these graphs show that the theoretical estimation of the width parameter does not fit with the experimental data at pixels that are close to the focus of the BBR beam. This lack of damping in the centre pixels can be attributed to some of the quasiparticles passing through the pixel without interacting with the tuning fork.

5.3 Source Wire Beam Profile Measurements

In this section, the beam profile from the source wire is analysed in the same manor as the BBR beam profile shown in the previous section with the drive on the source wire going up in steps to a final drive of 7 V over 100 k Ω using the tracking width program. These measurements are done in order to see if there are any similarities between the BBR beam and source wire beam profiles, where a direct comparison can be seen in section 5.4.

5.3.1 Calculating the Width Parameter of the Forks for the Source Wire Ramp

The method of the source wire ramp is similar to that stated for the BBR. The drive on the source wire was increased in steps until the wire was at a velocity of 21 mm/s corresponding to a power of 48 pW. The force velocity curve for the wire is shown in figure 5.14.

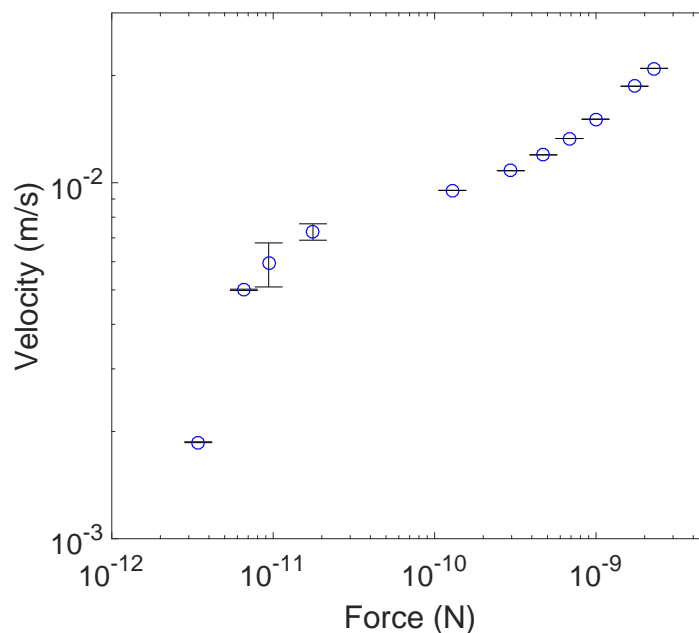


FIGURE 5.14: The force-velocity plot for the source wire. This graph shows that pair breaking happens at a velocity of the order of 10^{-2} m/s .

When the source wire was above 9 mm/s damping is created and a quasiparticle beam is produced. The extra damping from the wire is then seen on the camera and converted

into a width parameter using the same process shown in section 5.1. The width parameter of the forks in the centre of their respective arrays is plotted against the power of the source wire for high powers in figure 5.15.

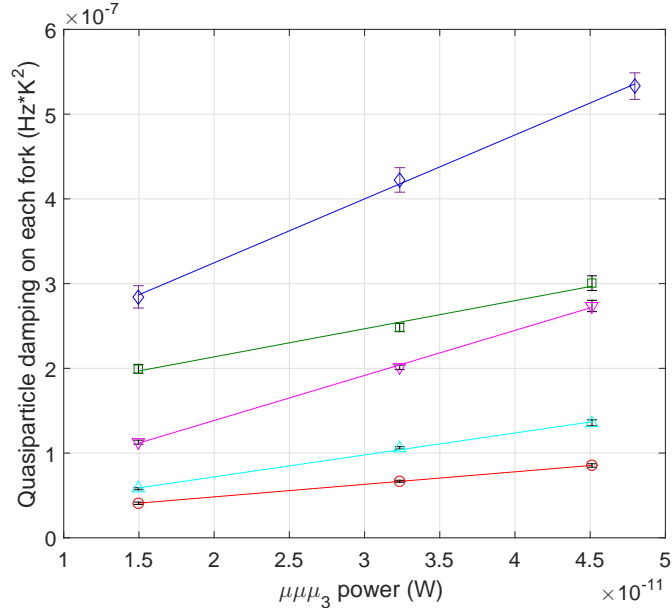


FIGURE 5.15: The width parameter against power for various forks during a $\mu\mu\mu_3$ ramp with A3 (red circles), B3 (green squares), C3 (blue diamonds), D3 (magenta downwards triangles), and E3 (cyan upwards triangles) shown where the velocity of the source wire is higher than the pair breaking critical velocity.

This graph shows there is a linear dependence between the width parameter of the fork and the power of the source wire at high powers. This indicates that the source wire beam profile at high powers does not change which is why this profile was chosen for further analysis.

5.3.2 Finding the Beam Profile for the Source Wire

As the relation of the width parameter of the forks to the power of the source wire was found to be linear at high powers we chose to analyse the highest power measurements in order to find the beam profile of the source wire. These measurements which are shown in figures 5.16, 5.17, and 5.18 were taken at a velocity of 21 mm/s and a power of 48 pW.

We can see that the beam seems to be centred around C2. This is in line with the position of the source wire in the cell. There is also less spread in the source wire beam profile than there is in the BBR profile, which may be due to the source wire being

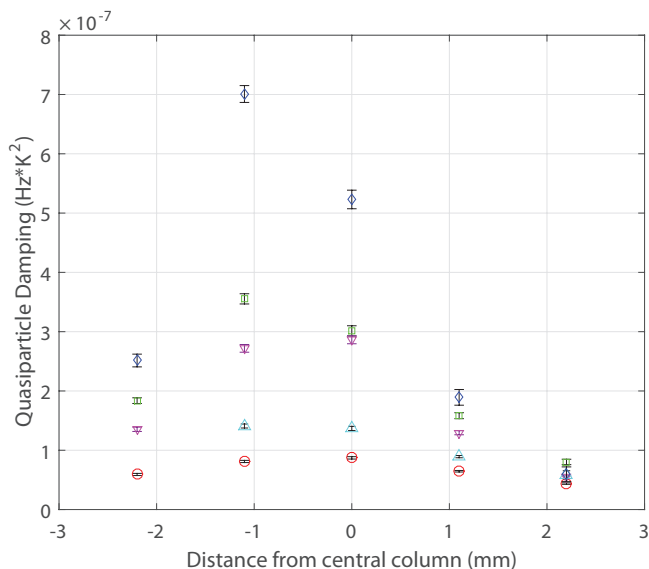


FIGURE 5.16: The full beam profile for the source wire where the power of the wire is approximately 48 pW. Shown in this figure are A array (Red circles), B array (Green Squares), C array (Blue Diamonds), D array (Magenta downwards triangles) and E array (Cyan upwards triangles). The beam from the source wire seems to be focused on C Array which indicates the beam is focused towards the centre of the camera.

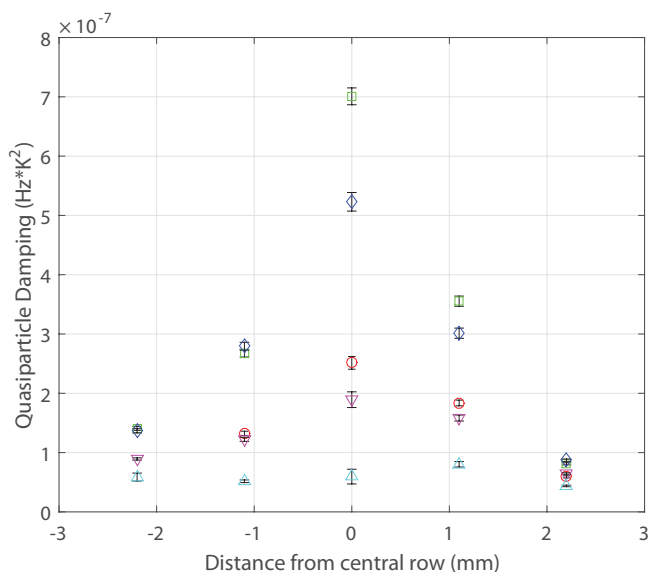


FIGURE 5.17: The full beam profile for the source wire where the power of the wire is approximately 48 pW. Shown in the figure are $x=-2.2$ mm (Red circles), $x=-1.1$ mm (Green squares), $x=0$ mm (Blue diamonds), $x=1.1$ mm (Magenta downwards triangles) and $x=2.2$ mm (Cyan upwards triangles). This graph shows that the beam is centred close to the second pixel.

closer to the camera. The apex of the source wire is slightly left to the centre of the array which may explain the shift in the beam profile.

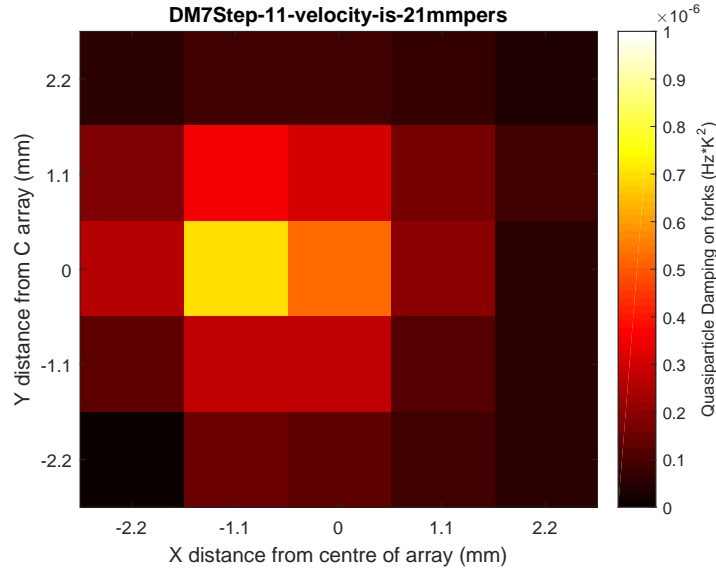


FIGURE 5.18: The full beam profile for the source wire shown in a colour map where the power of the wire is approximately 48 pW.

5.4 Comparing the Power Captured by the Quasiparticle Camera From the BBR to the Source Wire

The equation used to calculate the power in each pixel from experimental data has been estimated in equation 2.78 and is restated here with A_P substituted in as πR_P^2

$$\dot{Q}^F = \Delta f_2 \langle E \rangle T \frac{\pi k_B \rho^F t^F}{8 p_F^2 \gamma} \pi R_P^2. \quad (5.3)$$

This assumes that all the power emitted from the fork is from the front hole of the fork. If the back hole were to be included in this measurement then the area of the hole would be multiplied by a factor of 2. See figure 4.10 for more details about the pixel.

In this equation $A_P = \pi R_P^2$ where R_P is the radius of the pixel hole. Using this equation, we can find the power in each pixel. However there is an extra heat leak close to the quasiparticle camera that needs to be removed from the calculation of the power in the pixel. Therefore the true power of the pixel is given by $\dot{Q}_T^F = \dot{Q}^F - \dot{Q}_B^F$ where \dot{Q}_T^F is the 'True' power in the pixel which is only due to the quasiparticle beam. \dot{Q}^F is the power measured in each pixel and \dot{Q}_B^F is the power measured in each pixel with the quasiparticle generator at a low power. This is 0.006 pW for $\mu\mu\mu_3$ and 14 pW for the BBR. These experimental results were compared with theoretical calculations where the theoretical

calculations are explained in equation 2.69. Because this is a power comparison the theoretical calculation has not been multiplied by the calibration constant of 1.4.

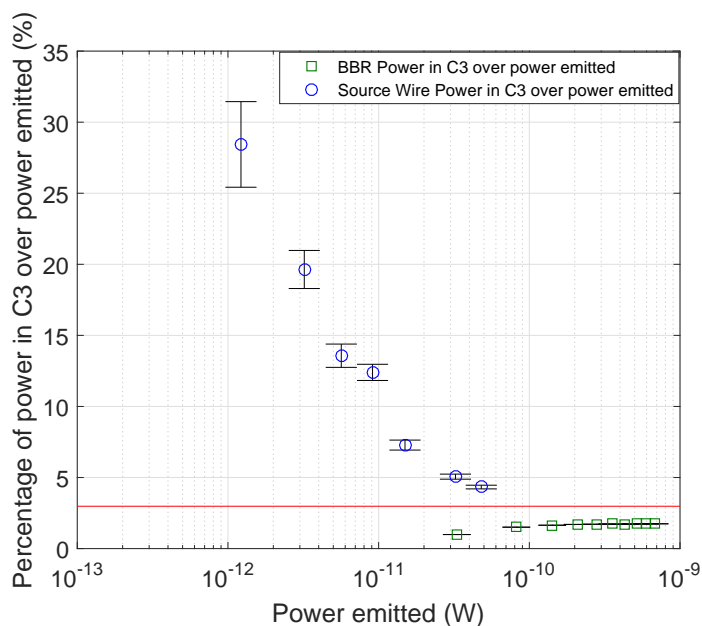


FIGURE 5.19: A comparison of the percentage of power trapped by $\mu\mu\mu_3$ and the BBR with a theoretical prediction shown as a red line for various powers. At low powers it shows that a high percentage of the power from the source wire is focused on the central pixels, with the beam spreading out at high powers.

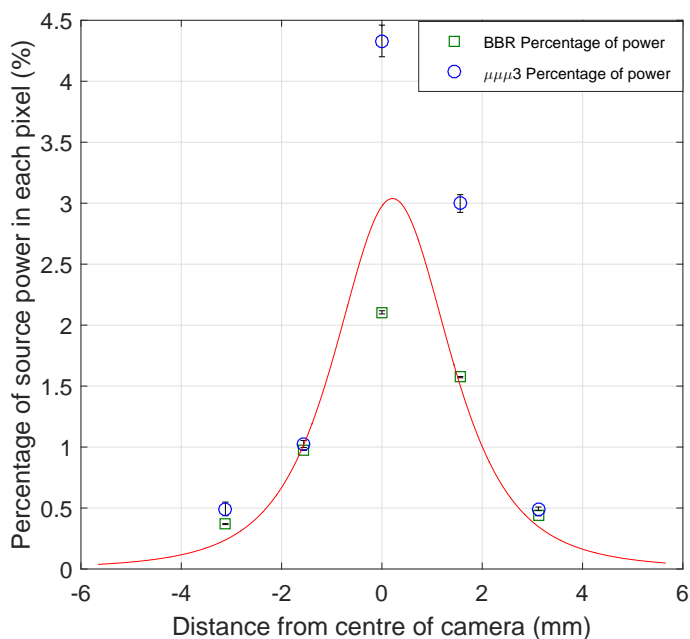


FIGURE 5.20: A comparison of the percentage of power trapped by the source wire at 48 pW and the BBR at 678 pW with the corrected theoretical prediction for the diagonal down the camera shown by a red line.

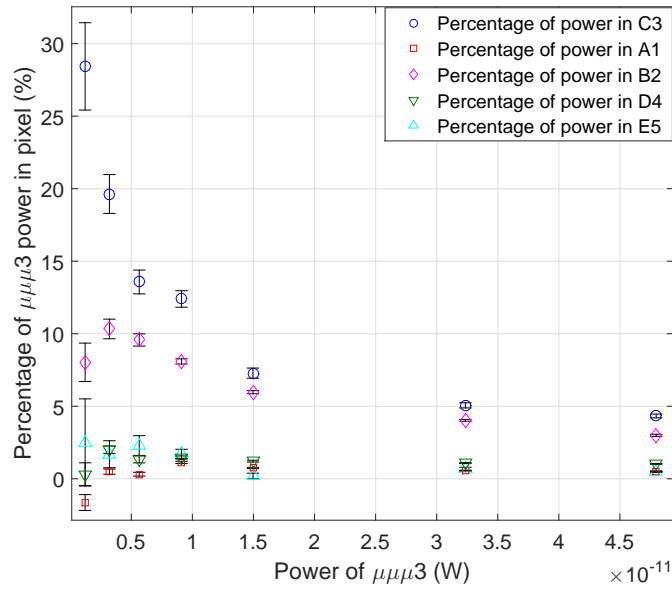


FIGURE 5.21: A comparison of the percentage of power trapped by the source wire at different powers for a diagonal along the camera. Note that A1 at low powers shows a negative power percentage. This may have been because of small oscillations in the cell temperature with a period of approximately 200 s.

Figure 5.21 shows the percentage of the power from $\mu\mu\mu_3$ that was seen in five tuning forks that constitute a diagonal cross section of the camera. This was for various powers that the source wire was at. The lowest power in this graph corresponds to a velocity of 8.5 mm/s and the highest power corresponds to a velocity of 21 mm/s.

The interesting thing about this figure is the high amount of damping seen on C3 at low powers. This indicates that the beam from $\mu\mu\mu_3$ spreads out when it gets to higher velocities. A decrease in the percentage of power with respect to the power increase can be seen on the central forks on this figure.

Figure 5.20 shows that the source wire creates a thinner quasiparticle beam than the BBR when the source wire is at a power of 48 pW. At lower powers the source wire will create a thinner beam as shown in figure 5.19. These thinner beams would be useful as they do not need a lot of power to create. This means that there would be less bulk damping in the cell which in turn means that the cell would stay cold for longer. As the thin beam is giving a large amount of power in a very small area it can be used reliably to find the exact position of turbulence though Andreev Reflection where various small thin beams could be used in order to determine the exact spatial properties of turbulence. One of the possible downsides of this idea is that a 3.2 mm wire was used to create this

thin beam. If a series of thin beams was ever created to probe turbulence then another smaller probe should be found to create it.

5.5 Chapter Summary

In this chapter, we used the quasiparticle camera in order to find the quasiparticle beam profile from a BBR and a source wire. In the BBR measurements, the BBR was calibrated and it was found that there was a linear relationship between the width parameter and power of the BBR. This in turn proves that the main source of dissipation of heat of the BBR was the quasiparticle beam that it emitted and that the quasiparticle beam profile did not change too much with power. This means that the BBR is useful for quasiparticle beam measurements when the BBR is driven to a high power and thus the beam profile was measured when the BBR was at a power of 678 pW. The measurements of the quasiparticle beam showed that the beam was focused between *C2* and *C3* and that it was relatively spread out. The quasiparticle beam damping was then calculated theoretically and then compared to the experimental results where the theoretical results gave a good fit to the data apart from the centre pixels. The discrepancies between the theoretical and experimental results were postulated to be due to some of the experimental quasiparticles passing straight through the pixel and not interacting with the tuning fork inside it.

We then studied the quasiparticle beam profile from a source wire. We found that there was a linear relationship between the source wires width parameter and power at high source wire powers and thus decided to study the source wire beam profile at a power of 48 pW. The beam profile of the source wire seemed to be focused on *C2* and was more focused on the central array. Finally, the percentage of the power emitted by these sources was compared against one another and compared against the theoretical predictions for the power captured by the BBR. These measurements found that at low powers the quasiparticle beam from the source wire becomes thinner. The discovery of this thin beam could be useful for use in measurements where only a small amount of the liquid needs to be probed and in situations where the measurements may be susceptible to the bulk thermal damping in the cell.

Chapter 6

Summary

This thesis presents first measurements of the quasiparticle beam profile of the Black-Body radiator and the source wire using a 25 pixel quasiparticle camera.

In the Black-Body radiator beam profile measurements, the BBR was calibrated and it was found that there were no other main sources of dissipation for the BBR, except for the quasiparticle beam it emitted when the BBR was at a high power. From this result, it was decided that the beam profile would be analysed at the highest power in that BBR ramp, which was a power of 678 pW. The BBR beam profile was then found to be centred slightly left of centre to the central pixel and was then compared to a theoretical model in which the theoretical model predicted a larger amount of damping than that which was seen on the central pixels. The quasiparticle beam profile from the source wire was then measured in which a linear relationship was found between the source wires width parameter and power near a power of 48 pW in which the beam profile from this source wire was found to be focused on the centre array of the camera. The quasiparticle damping on the tuning forks due to the quasiparticle beam of the BBR and source wire were then converted into a percentage of the total power emitted in order to compare the beam profiles directly to one another. The source wire was found to have a much thinner beam compared to the BBR in which the beam was concentrated on C3 at low source wire powers.

Two geometrical constants were also found in this thesis, λ which relates to the force-velocity characteristics of the probe and γ which relates to the sensitivity of the probe to quasiparticles. The value of λ was calculated for 2 wires, a tuning fork, and the tuning

forks overtone mode. In these measurements it was found that the mode of oscillation of the fork affected the value of λ and that the value of λ was probably dependent on the geometry of the probe. The value of γ was also found for various wires and forks in the cell where it was found for $\mu\mu\mu_2$ via a BBR calibration and then estimated for other wires in the cell via a comparison of the thermal damping between the other wires and $\mu\mu\mu_2$. The values of γ for all of the wires were similar to one another except for the MEMS which had a different geometry than the other wires. The sensitivity of the probe to quasiparticles was then found for a fork using its resonant mode as a thermometer wire and its overtone as a heater which was then used to find the value of γ for all other tuning forks in the camera. All the forks had a value of γ that was similar to one another.

Appendix A

Preliminary Measurements

In order for any of the measurements to be properly analysed a set of preliminary measurements had to be taken. The objective of most of these measurements are to make sure that we can find the thermal width of the forks. From finding the thermal width we can then find the beam profile and estimate γ and λ for the forks and wires.

All of these measurements are taken using Labview programs created by Viktor Tsepelin and then analysed using Matlab 2015*a*. The results of the preliminary measurements are stored in a parameter file that can then be loaded and used for quick analysis.

A.1 Background Corrections

All probes in the cell have amplitude dependent backgrounds. All frequency sweeps can find and subtract the background from the measurement taken. However for any DAQ measurements or amplitude sweeps the background cannot be found with the measurement so they have to be taken beforehand and then put in the measurement as a parameter.

For the forks the backgrounds are taken using the amplitude sweep program to drive the fork at fixed frequency 100 Hz either side of the resonance. This is shown in figure [A.1](#).

In these measurements of figure [A.1](#) the drive of the probe is increased from 0.71 mV to 7 V at a fixed frequency as described before. The time constant for each point is

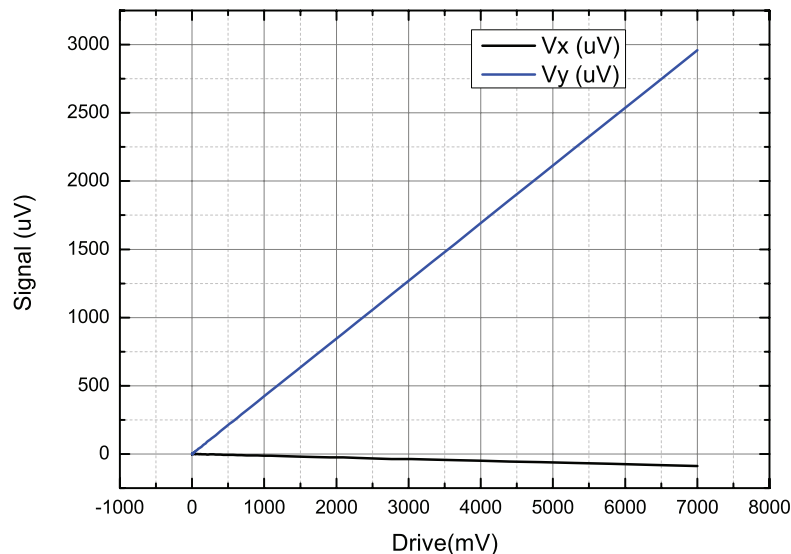


FIGURE A.1: A typical fork background.

300 ms and the time taken between points is 2.1 s. The phase that these backgrounds are taken at are the same phase that was taken on the frequency sweeps right before this measurement.

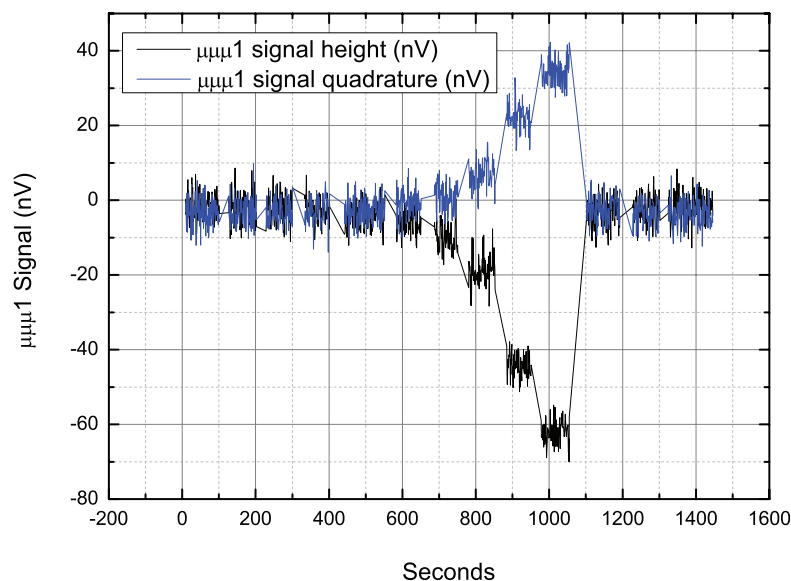


FIGURE A.2: A DAQ background done at zero field.

For the wires the backgrounds were taken when they were at zero magnetic field using the DAQ program at the same frequency for which they were on resonance during the demagnetization. As the wires were taken at zero field as this means that there was no Faraday voltage coming from the wires as there was no magnetic field to induce it. These normally use a time constant of 300 ms and a time between points of 1 s.

In these measurements the drive is kept fixed for a short period of time (100 s) and then the drive is increased to a higher value. This is shown in figure [A.2](#).

In figure [A.2](#) all the wires are being measured at the same time. The drive on the wires is then ramped up logarithmically from 10 mV to 7 V. The values V_x and V_y for each drive are plotted against drive and then fitted. The backgrounds are then put into the DAQ and amplitude programs and then taken off by the respective programs themselves.

A.2 Intrinsic

There are three contributions to fork damping these are explained in figure [2.55](#) which has been written here.

$$F = F_I + F_T + F_{ex}. \quad (\text{A.1})$$

In order to find the thermal damping F_T we need to find the intrinsic damping F_I and the damping at high velocities F_{ex} . The non-linear damping F_{ex} can be found using non-linear corrections and will be explained later. equation [A.1](#). This can be rearranged to find the intrinsic width equation [A.2](#).

$$F_I = F - F_T - F_{ex}. \quad (\text{A.2})$$

The intrinsic damping F_I is due to the mechanical dissipation of the probe. This can be found when the probe is at vacuum at the lowest temperatures and when the probe has been driven to low velocities, i.e. when F_T and F_{ex} are minimal compared to the size of F_I . The only part of the previous equation that is temperature dependent is the force F_T . The intrinsic damping and the damping at high velocities are independent of temperature.

One of the ways of finding the intrinsic and the non-linear damping is to do an amplitude sweep of the probe at the lowest temperatures possible.

This amplitude sweep takes care of all contributions to the damping force that are not due to the bulk temperature including the effect of pair breaking on the fork, the non-linear damping on the fork, and the intrinsic damping on the fork.

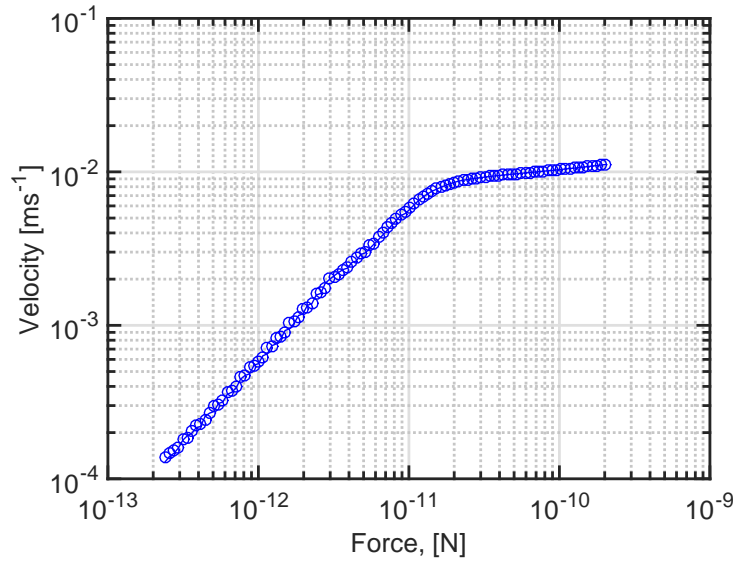


FIGURE A.3: An intrinsic amplitude sweep of the fork A2 at a temperature of 108 μK .

The force of this amplitude sweep can then be subtracted from the force of an amplitude sweep at higher temperatures in order to find λ ; this is explained in section 4.1.

Another way the intrinsic damping was estimated was by measuring the width of the probe using a frequency sweep program at the coldest possible temperatures at velocities which we know are far lower than any in which non-linear corrections would have had to take place (forks driven to 100 μV which gives a velocity of ~ 0.1 mm/s). This is in ^3He which means that there may have still been a slight amount of thermal damping in the intrinsic that had been unaccounted for.

The intrinsics that were used later on in the analysis are estimated alongside λ using the non-linear corrections explained in section A.3.

A.3 Non-Linear Corrections

It is sometimes beneficial to drive probes to high velocities in order to increase the signal to noise ratio. When these probes are driven to such a velocity they exhibit non-linear behaviour.

The best way to do this is to linearise the damping on the probe. Equation A.3 reminds us of the thermal force acting on a paddle taking into account Andreev reflection.

$$F_{NL} = 2Ap_F \langle nv_g \rangle \gamma (1 - e^{-\lambda p_F v / (k_B T)}). \quad (\text{A.3})$$

The force has been shown to be correlated to the width of the resonance in equation 2.19. The important part of that equation is shown as

$$((\Delta f_2)_{NL}) \sim F_{NL}, \quad (\text{A.4})$$

where F_{NL} is the thermal and extra non-linear damping and $(\Delta f_2)_T$ is the thermal and non-linear damping on the probe. In order to get rid of the non-linear damping we multiply the width of the resonance by the force if the probe is linear and divide by the non-linear force.

$$(\Delta f_2)_T = ((\Delta f_2)_{NL}) \frac{F_L}{F_{NL}}. \quad (\text{A.5})$$

In this equation the force when the probe is non-linear F_{NL} is given by equation A.3 and the force when the probe is driven to low velocities F_L is given below.

$$F_L = \frac{-2Ap_F \langle nv_g \rangle \gamma \lambda p_F v}{(k_B T)}. \quad (\text{A.6})$$

Putting equation A.6 and equation A.3 into equation A.5 the width due to thermal damping can be estimated as

$$(\Delta f_2)_T = (\Delta f_2)_{NL} \frac{\lambda p_F v / k_B T}{(1 - e^{-\lambda p_F v / (k_B T)})}. \quad (\text{A.7})$$

In order to find the effect of the non-linear damping on the width of the resonance the intrinsic width has to be subtracted first. The true width of the resonance which is the combination of the resonances thermal and intrinsic widths is given as

$$(\Delta f_2)_{True} = (\Delta f_2)_I + (((\Delta f_2) - (\Delta f_2)_I) \frac{\lambda p_F v / k_B T}{(1 - e^{-\lambda p_F v / (k_B T)})}). \quad (\text{A.8})$$

In the non-linear measurements that were taken the drive on the probe was constant on the DAQ for a fixed amount of time 100s and then increased. This is shown in figure A.5. The time axis is the same for figure A.4, figure A.5, and figure A.6. This means all of these graphs can be compared against one another.

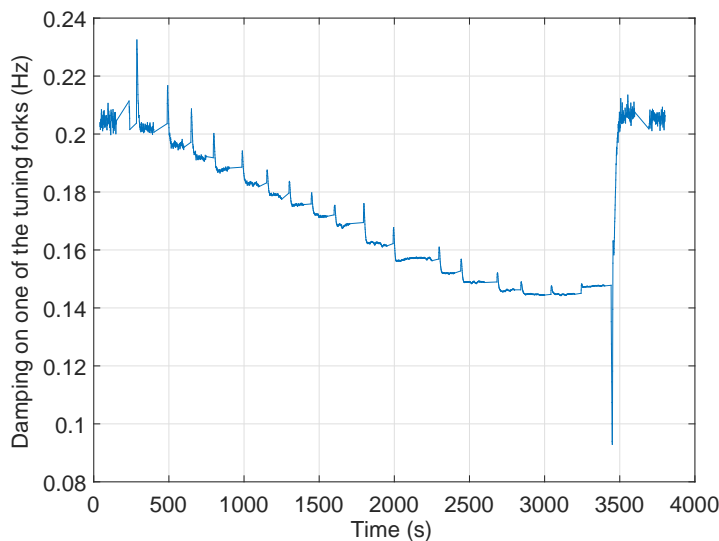


FIGURE A.4: Change in the width of a probe due to non-linearity. The probe V_x was ramped from 0.1 mV to 3 mV.

The decrease in damping seen in figure A.4 is due to the non-linearity of the fork. When the damping seems to increase at the end of the measurement this is because of the probe creating quasiparticles and thus warming the area around the probe.

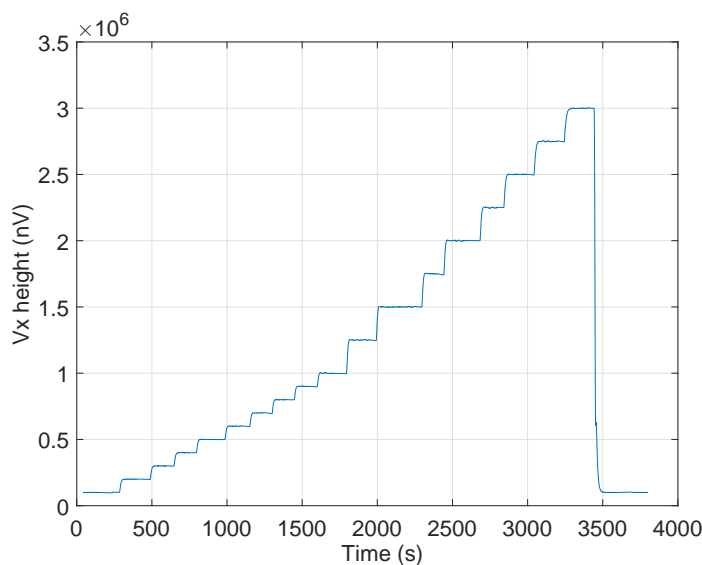


FIGURE A.5: Signal height the probe was driven to during the non-linear measurement.

Figure A.4 shows the decrease in width of one of the probes when the drive on the probe is increased. The true width of the probe was then calculated which is shown in equation A.8. The value of λ is calculated such that no decrease in width can be seen in the true width. This is shown in figure A.6.

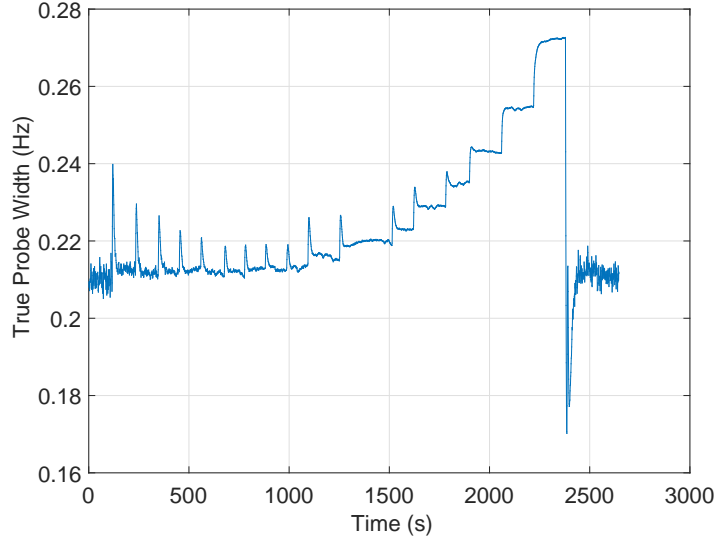


FIGURE A.6: The width of the probe after it was non-linearly corrected using equation A.8.

In figure A.6 there is no decrease in the width of the probe due to non-linear damping. However it can be seen that at higher drives the probe has an increase in damping. This is because the probe starts generating quasiparticles which then cause an increase in the temperature which increases the probe damping.

Using this method to estimate λ we get a value of 0.45 for all of the forks. λ has been calculated for the wires with a far better method, and these results will be explained later on.

A.4 Effective Width

While the width of the $M\mu$ has been calibrated in order to give the temperature this only gives the temperature of one part of the cell which we call the bulk temperature. Looking back at figure 3.1 it can be seen that if the quasiparticle beam from the BBR is on then the temperature inside the BBR and the temperature of anything hitting the beam is going to be much higher than the bulk temperature.

The only way that this temperature can be found for other probes in the cell is if we calibrate these probes against the $M\mu$ thus working out what the width would be if the probe was a $M\mu$ an 'effective' width. This is shown below.

$$(\Delta f_2)_P = C(\Delta f_2)_{M\mu}, \quad (\text{A.9})$$

where $(\Delta f_2)_P$ is the resonant width of the probe and $(\Delta f_2)_{M\mu}$ is the resonant width of the $M\mu$. This equation assumes that there aren't any thermal gradients in the cell. At high temperatures this assumption of thermal equilibrium in the cell is valid.

The calibration constant C is what we call the effective width of the probe. This can be found by plotting the probe width against the $M\mu$ width at various temperatures. This is normally achieved by doing frequency sweeps on the probe and $M\mu$ at various temperatures during a demagnetization and then comparing them. figure A.7 shows this plot for one of the pixels in the camera.

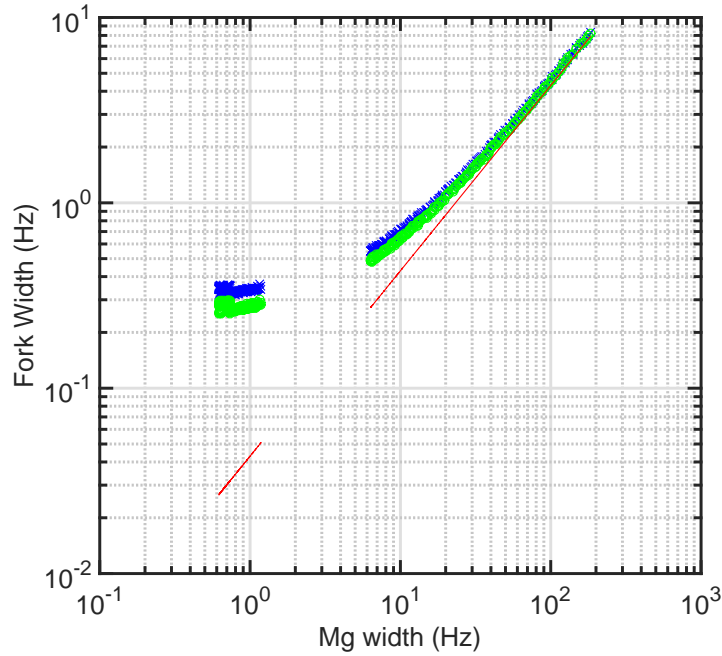


FIGURE A.7: Plot of the fork width against the width of the $M\mu$.

At low temperatures there may be a distinct difference in the fork temperature to the $M\mu$ temperature. Therefore it is best to calibrate between the $M\mu$ and the forks at a range of high temperatures. Figure A.8 shows how the effective width of the probe tails off.

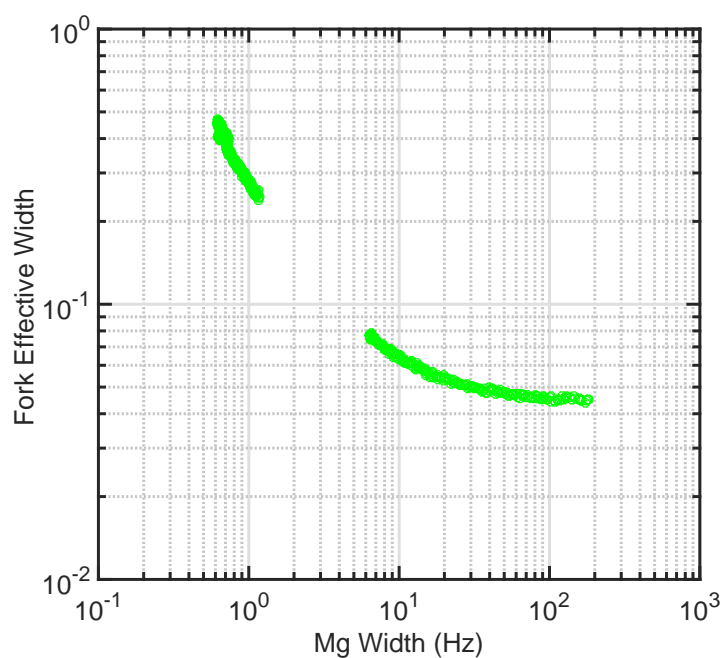


FIGURE A.8: Plot of the fork effective width against the $M\mu$ width.

The B array measurements are done at a different time and are shown in figure A.9. In this graph the effective width changes after 3 kHz.

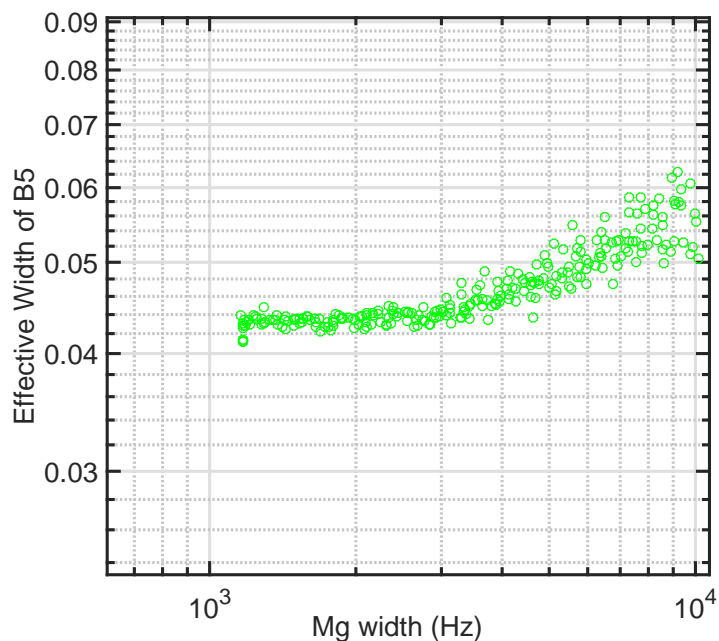


FIGURE A.9: Plot of the effective width of a fork in B array against the width of the $M\mu$.

In figure A.8 the Effective width tails off at about 0.045 for forks and for wires is 0.33 for $\mu\mu\mu$ wires and 0.1 for μ wires. Once the effective width C is found the width of the

probe as if it were a $M\mu$ can be calculated,

$$(\Delta f_2)_{M\mu} = \frac{(\Delta f_2)_P}{C}. \quad (\text{A.10})$$

By calibrating the width of the probe the temperature around the probe can be found. From the temperature the width parameter and the thermal damping can be found. Through using the effective width all probes in the cell can now be used as thermometers.

Bibliography

- [1] B.M. Oliver, James G. Bradley, and Harry Farrar. Helium Concentration in the Earth's Lower Atmosphere. *Geochimica et Cosmochimica Acta*, 48(9):1759 – 1767, 1984. ISSN 0016-7037. doi: [http://dx.doi.org/10.1016/0016-7037\(84\)90030-9](http://dx.doi.org/10.1016/0016-7037(84)90030-9).
URL
<http://www.sciencedirect.com/science/article/pii/0016703784900309>.
- [2] Kaye and Laby. Table of Physical and Chemical Constants. Online. URL
http://www.kayelaby.npl.co.uk/chemistry/3_1/3_1_3.html.
- [3] Hector. MacPherson.Jr. Pierre Jules Cesar Janssen. *Popular Astronomy*, 16: 72–74, 1908.
- [4] A. L. Cortie. Sir Norman Lockyer, 1836-1920. *Astrophysical Journal*, 53:233–248, 1921.
- [5] R. K. Kochhar. French Astronomers in India During the 17th - 19th Centuries. *Journal of the British Astronomical Association*, 101:95–100, 1991.
- [6] E. R. Dobbs. *Helium Three*. Oxford University Press, Oxford, 2001. Page 1.
- [7] J.E Cederblom. Award Ceremony Speech, The Nobel Prize in Chemistry, Sir William Ramsay, 1904. URL http://www.nobelprize.org/nobel_prizes/chemistry/laureates/1904/press.html.
- [8] M.L.E Oliphant, B.B Kinsey, and Rutherford.E. The Transmutation of Lithium by Protons and by Ions of the Heavy Isotope of Hydrogen. *Proc R Soc Lond*, 1933.
- [9] U.S. Geological Survey, Mineral Commodity Summaries, February 2014. Online. URL <http://minerals.usgs.gov/minerals/pubs/commodity/helium/mcs-2014-heliu.pdf>.

- [10] ITER, What is Fusion ? URL <https://www.iter.org/sci/Whatisfusion>.
- [11] Steve Conner. Why the World is Running out of Helium, 2010. URL <http://www.independent.co.uk/news/science/why-the-world-is-running-out-of-helium-2059357.html>.
- [12] Adrian Cho. Helium-3 Shortage Could Put Freeze On Low-Temperature Research. *Science*, 2009. URL <http://www.sciencemag.org/content/326/5954/778.full>.
- [13] Alan J. Hurd and Richard T. Kouzes. Why New Neutron Detector Materials Must Replace Helium-3. *The European Physical Journal Plus*, 129(10):236, 2014. doi: 10.1140/epjp/i2014-14236-6. URL <http://dx.doi.org/10.1140/epjp/i2014-14236-6>.
- [14] Robert Richardson. Nobel Prizewinner: We are Running out of Helium. *New Scientist*, 2773, 2010. URL <https://www.newscientist.com/article/mg20727735-700-nobel-prizewinner-we-are-running-out-of-helium/>.
- [15] Dana A. Shea and Daniel Morgan. CRS Report for Congress Prepared for Members and Committees of Congress The Helium-3 Shortage: Supply, Demand, and Options for Congress. Online, December 2010.
- [16] Peter Kes. Dirk van Delft. The Discovery of Superconductivity. *Physics Today*, September 2010.
- [17] Dirk van Delft. Heike Kamerlingh Onnes and the Road to Liquid Helium. 2011. URL <http://snf.ieeecsc.org/sites/ieeecsc.org/files/RN19.pdf>.
- [18] Dirk van Delft. *Freezing physics Heike Kamerlingh Onnes and the quest for cold*. Number pp 16. Koninklijke Nederlandse Akademie van Wetenschappen, 2007. URL <http://www.dwc.knaw.nl/wp-content/HSSN/2007-10-Van%20Delft-Freezing%20Physics.pdf>.
- [19] H. Kittel, C. Kroemer. *Thermal Physics*. Number pp 339. Freeman, W.H. and Company, 1980.
- [20] T.H Nordstrom. Award Ceremony Speech, The Nobel Prize in Physics 1913 Heike Kamerlingh Onnes. Online, 1913. URL http://www.nobelprize.org/nobel_prizes/physics/laureates/1913/press.html.

- [21] C. Enss, C. Hunklinger. *Low-Temperature Physics*. Number pp 7-10. Springer, 2005.
- [22] The Nobel Prize in Physics 1978, 1978. URL http://www.nobelprize.org/nobel_prizes/physics/laureates/1978/.
- [23] Meredith. D McClintock. P and Wigmore. J. *Matter at Low Temperatures*. Blackie, 1984.
- [24] S. G. Sydoriak, E. R. Grilly, and E. F. Hammel. Condensation of Pure He³ and Its Vapor Pressures between 1.2° and Its Critical Point. *Phys. Rev.*, 75:303–305, Jan 1949. doi: 10.1103/PhysRev.75.303. URL <http://link.aps.org/doi/10.1103/PhysRev.75.303>.
- [25] D. D. Osheroff, R. C. Richardson, and D. M. Lee. Evidence for a New Phase of Solid ³He. *Phys. Rev. Lett.*, 28:885–888, 1972.
- [26] C. Nording. The Nobel Prize in Physics 1996 Award Ceremony Speech, 1996. URL http://www.nobelprize.org/nobel_prizes/physics/laureates/1996/presentation-speech.html.
- [27] David M. Lee. The Extraordinary Phases of Liquid ³He. *Rev. Mod. Phys.*, 69: 645–666, Jul 1997. doi: 10.1103/RevModPhys.69.645. URL <http://link.aps.org/doi/10.1103/RevModPhys.69.645>.
- [28] J. Bardeen, L. N. Cooper, and J. R. Schrieffer. Theory of superconductivity. *Phys. Rev.*, 108:1175–1204, Dec 1957. doi: 10.1103/PhysRev.108.1175. URL <http://link.aps.org/doi/10.1103/PhysRev.108.1175>.
- [29] A. M. Guénault. *Basic Superfluids*. Taylor and Francis, 2003.
- [30] P. W. Anderson and P. Morel. Generalized Bardeen-Cooper-Schrieffer States and the Proposed Low-Temperature Phase of Liquid ³He. *Phys. Rev.*, 123:1911–1934, Sep 1961. doi: 10.1103/PhysRev.123.1911. URL <http://link.aps.org/doi/10.1103/PhysRev.123.1911>.
- [31] R. Balian and N. R. Werthamer. Superconductivity with Pairs in a Relative p Wave. *Phys. Rev.*, 131:1553–1564, Aug 1963. doi: 10.1103/PhysRev.131.1553. URL <http://link.aps.org/doi/10.1103/PhysRev.131.1553>.

- [32] D. S. Greywall. Helium 3 Specific Heat and Thermometry at Millikelvin Temperatures. *Phys Rev B*, 33:7520, 1986.
- [33] Advanced Information on the Nobel Prize in Physics, 7 October 2003, October 2003. URL http://www.nobelprize.org/nobel_prizes/physics/laureates/2003/advanced-physicsprize2003.pdf.
- [34] S.N. Fisher. *The Mechanical Properties of Superfluids $^3\text{He-A}$ and $^3\text{He-B}$ in the Ballistic Regime*. PhD thesis, Lancaster University, 1991.
- [35] A. J. Leggett. A theoretical description of the new phases of liquid ^3He . *Rev. Mod. Phys.*, 47:331–414, 1975.
- [36] A. F. Andreev. Thermal conductivity of the intermediate state of superconductors 2. *J.Exper.Theoret.Phys (U.S.S.R)*, 47:2222–2228, 1965.
- [37] S. N. Fisher, G. R. Pickett, and R. J. Watts-Tobin. A microscopic calculation of the force on a wire moving through superfluid $^3\text{He-B}$ in the ballistic regime. *J. Low Temp. Phys.*, 83:225, 1991.
- [38] P. Vollhardt, D. Wölfle. *The Superfluid Phases of Helium 3*. Taylor and Francis, 1990. Page 27.
- [39] C. J. Lambert. Theory of pair breaking by vibrating macroscopic objects in superfluid ^3He . *Physica B*, 178:294, 1992.
- [40] J.P Carney, A. M. Guénault, G.R Pickett, and G.F. Spencer. Extreme nonlinear damping by the quasiparticle gas in superfluid Helium 3-B in the low-temperature limit. *Phys Rev Lett*, 62:3042, 1989.
- [41] D.J. Cousins, S.N. Fisher, A.M. Guénault, R.P. Haley, I.E. Miller, G.R. Pickett, G.N. Plenderleith, P. Skyba, P.Y.A. Thibault, and M.G. Ward. An advanced dilution refrigerator designed for the new lancaster microkelvin facility. *Journal of Low Temperature Physics*, 114(5-6):547–570, 1999. ISSN 0022-2291. doi: 10.1023/A:1021862406629. URL <http://dx.doi.org/10.1023/A%3A1021862406629>.
- [42] O V Lounasmaa. Dilution refrigeration. *Journal of Physics E: Scientific Instruments*, 12(8):668, 1979. URL <http://stacks.iop.org/0022-3735/12/i=8/a=001>.

- [43] D. I. Bradley, S. N. Fisher, A. M. Guénault, M. R. Lowe, G. R. Pickett, A. Rahm, and R. C. V. Whitehead. Quantum Turbulence in Superfluid ^3He Illuminated by a Beam of Quasiparticles. *Phys. Rev. Lett.*, 93(23):235302, 2004.
- [44] S.N. Fisher and G.R. Pickett. Superfluid ^3He in the zero-temperature limit. *Progress in Low Temperature Physics*, 16:147–194, 2009.
- [45] D.I. Bradley, A.M. Guénault, V. Keith, C.J. Kennedy, I.E. Miller, S.G. Mussett, G.R. Pickett, and Jr. Pratt, W.P. New methods for nuclear cooling into the microkelvin regime. *Journal of Low Temperature Physics*, 57(3-4):359–390, 1984. ISSN 0022-2291. doi: 10.1007/BF00681199. URL <http://dx.doi.org/10.1007/BF00681199>.
- [46] S.L. Ahlstrom, D.I. Bradley, S.N. Fisher, A.M. Guénault, E.A. Guise, R.P. Haley, S. Holt, O. Kolosov, P.V.E. McClintock, G.R. Pickett, M. Poole, R. Schanen, V. Tsepelin, and A.J. Woods. A Quasiparticle Detector for Imaging Quantum Turbulence in Superfluid $^3\text{He-B}$. *Journal of Low Temperature Physics*, 175(5-6): 725–738, 2014. ISSN 0022-2291. doi: 10.1007/s10909-014-1144-2. URL <http://dx.doi.org/10.1007/s10909-014-1144-2>.
- [47] E.A. Guise. *Developing a Quasiparticle Detector for Quantum Turbulence Imaging Studies in Superfluid $^3\text{He-B}$* . PhD thesis, Lancaster University, 2014.
- [48] S. Holt and P. Skyba. Electrometric direct current I/V converter with wide bandwidth. *Review of Scientific Instruments*, 83:064703, 2012. doi: 10.1063/1.4725526.
- [49] Agilent Technologies. California. USA.
- [50] SR830 / SR844. Stanford research systems. California, USA .
- [51] S. Triqueneaux, E. Collin, D. Cousins, T. Fournier, Y. M. Bunkov, and C. Bäuerle. Microfabrication of silicon vibrating wires. *Physical B Condensed Matter*, pages 2141–2142, 2000.
- [52] Eddy Collin, Laure Filleau, Thierry Fournier, YuriyM. Bunkov, and Henri Godfrin. Silicon Vibrating Wires at Low Temperatures. *Journal of Low Temperature Physics*, 150(5-6):739–790, 2008. ISSN 0022-2291. doi:

- 10.1007/s10909-007-9607-3. URL
<http://dx.doi.org/10.1007/s10909-007-9607-3>.
- [53] M. Defoort, S. Dufresnes, S.L. Ahlstrom, D.I. Bradley, R.P. Haley, A. M. Guénault, E.A Guise, G.P. Pickett, M. Poole, A.J Wood, V. Tsepelin, S.N Fisher, H. Godfrin, and E. Collin. Probing Bogoliubov quasiparticles in superfluid ^3He with a 'vibrating-wire like' MEMS device. *Journal of Low Temperature Physics*, 183(3):286–291, 2016.
- [54] R. Blaauwgeers, M. Blazkova, M. Clovecko, V. B. Eltsov, R. de Graaf, J. Hosio, M. Krusius, D. Schmoranzler, W. Schoepe, L. Skrbek, P. Skyba, R. E. Solntsev, and D. E. Zmeev. Quartz Tuning Fork: Thermometer, Pressure- and Viscometer for Helium Liquids. *J. Low Temp. Phys.*, 146(5/6):537–562, 2007. doi: 10.1007/s10909-006-9279-4.
- [55] National Instruments. GPIB (IEEE 488). Online, 2015. URL
<http://www.ni.com/gpib/>.
- [56] National Instruments. NI BNC-2110. Online, 2015. URL
<http://sine.ni.com/nips/cds/view/p/lang/en/nid/1865>.
- [57] Statek Corporation, California, USA.
- [58] K. Karrai and R. D. Grober. Tip-sample distance control for near-field scanning optical microscopes. In M. A. Paesler and P. T. Moyer, editors, *Near-Field Optics*, volume 2535, pages 69–81, Bellingham, 1995. SPIE.
- [59] D. I. Bradley, M. Človečko, S. N. Fisher, D. Garg, E. Guise, R. P. Haley, O. Kolosov, G. R. Pickett, V. Tsepelin, D. Schmoranzler, and L. Skrbek. Crossover from hydrodynamic to acoustic drag on quartz tuning forks in normal and superfluid ^4He . *Phys. Rev. B*, 85:014501, 2012. doi: 10.1103/PhysRevB.85.014501.
- [60] D. I. Bradley, P. Crookston, M. J. Fear, S. N. Fisher, G. Foulds, D. Garg, A. M. Guénault, E. Guise, R. P. Haley, O. Kolosov, G. R. Pickett, R. Schanen, and V. Tsepelin. Measuring the Prong Velocity of Quartz Tuning Forks Used to Probe Quantum Fluids. *J. Low. Temp. Phys.*, 161(5-6, SI):536–547, 2010. ISSN 0022-2291. doi: 10.1007/s10909-010-0227-y.

- [61] S.S. Chuang. Quartz Tuning Fork Crystal Using Overtone Flexure Modes. *Proc. 35th Ann. Freq. Control Symposium*, pages 130–142, 1981.
- [62] K. Karrai. Lecture notes on shear and friction force detection with quartz tuning forks. *lecture notes*, pages 1–23, 2000. URL http://www.nano.physik.uni-muenchen.de/publikationen/Preprints/p-00-03_Karrai.pdf.
- [63] C. Bäuerle, Yu. M. Bunkov, S. N. Fisher, and H. Godfrin. Temperature scale and heat capacity of superfluid $^3\text{He} - B$ in the $100\mu\text{K}$ range. *Phys. Rev. B*, 57:14381–14386, Jun 1998. doi: 10.1103/PhysRevB.57.14381. URL <http://link.aps.org/doi/10.1103/PhysRevB.57.14381>.
- [64] S. N. Fisher, A. M. Guénault, C. J. Kennedy, and G. R. Pickett. Blackbody source and detector of ballistic quasi-particles in $^3\text{He}-B$ - Emission angle from a wire moving at supercritical velocity. *Phys. Rev. Lett.*, 69:1073, 1992.
- [65] D. I. Bradley, P. Crookston, S. N. Fisher, A. Ganshin, A. M. Guénault, R. P. Haley, M. J. Jackson, G. R. Pickett, R. Schanen, and V. Tsepelin. The Damping of a Quartz Tuning Fork in Superfluid He-3-B at Low Temperatures. *J. Low Temp. Phys.*, 157(5-6):476–501, 2009.
- [66] S. N. Fisher, A. M. Guénault, C. J. Kennedy, and G. R. Pickett. Beyond the 2-fluid model - Transition from linear behavior to a velocity-independent force on a moving object in $^3\text{He}-B$. *Phys. Rev. Lett.*, 63:2566, 1989.
- [67] D.I. Bradley, M.Clovecko, E. Gazo, and P.Skyba. Probing Andreev reflection in superfluid $^3\text{He}-B$ using a quartz tuning fork. *J. Low Temp Phys.*, 152:147–155, 2008.
- [68] D. I. Bradley, Yu. M. Bunkov, D. J. Cousins, M. P. Enrico, S. N. Fisher, M. R. Follows, A. M. Guénault, W. M. Hayes, G. R. Pickett, and T. Sloan. Potential Dark Matter Detector? The Detection of Low Energy Neutrons by Superfluid ^3He . *Phys. Rev. Lett.*, 75:1887–1890, Sep 1995. doi: 10.1103/PhysRevLett.75.1887. URL <http://link.aps.org/doi/10.1103/PhysRevLett.75.1887>.
- [69] D.I Bradley, S.N.Fisher, A. M.and M.R. Lowe Guénault, G.R. Pickett, and A. Rahm. Direct observation of the Andreev reflection of a quasiparticle beam by quantum turbulence in superfluid $^3\text{He}-B$. *Physica B*, pages 64–65, 2003.

- [70] D.I. Bradley, S.N. Fisher, A.M. Guénault, M. Lowe, G.R. Pickett, and A. Rahm. Preliminary measurements of andreev reflection of quasiparticles by turbulence in superfluid ^3He . *Journal of Low Temperature Physics*, 124(1-2):113–122, 2001. ISSN 0022-2291. doi: 10.1023/A:1017569716880. URL <http://dx.doi.org/10.1023/A%3A1017569716880>.
- [71] D. I. Bradley, S. N. Fisher, A. M. Guénault, R. P. Haley, G. R. Pickett, D. Potts, and V. Tsepelin. Direct measurement of the energy dissipated by quantum turbulence. *Nature Physics*, 7:473, 2011. doi: 10.1038/nphys1963.
- [72] S.N. Fisher and G.P. Pickett. Quantum Turbulence in Superfluid ^3He at Very Low Temperatures. *Progress in Low Temperature Physics*, 2009. Page 173.
- [73] M.J. Jackson. *A Study of Quantum Turbulence in Superfluid $^3\text{He-B}$ Using Vibrating Structures*. PhD thesis, Lancaster University, 2011.
- [74] G.R. Pickett. Superfluid ^3He , a two-fluid system, with the normal-fluid dynamics dominated by Andreev reflection. *Journal of Experimental and Theoretical Physics*, 119(6):1058–1068, 2014. ISSN 1063-7761. doi: 10.1134/S1063776114120140. URL <http://dx.doi.org/10.1134/S1063776114120140>.
-